UNIVERSITY OF CALIFORNIA SAN DIEGO

Innovations in ocean biogeochemical instrumentation and monitoring

A dissertation submitted in partial satisfaction of the requirements
for the degree Doctor of Philosophy

in

Oceanography

by

Taylor Wirth

Committee in charge:

Todd Martz, Chair
Ryan Kastner
Sarah Purkey
Dale Stokes
Yuichiro Takeshita

2024

The dissertation of Taylor Wirth is approved, and it is acceptable in quality and form for publication on microfilm and electronically.

University of California San Diego

2024

TABLE OF CONTENTS

LIST OF FIGURES

LIST OF TABLES

ACKNOWLEDGEMENTS

I would like to express my deepest gratitude to my advisor, Todd Martz. Working together over the past decade has been an incredible privilege, and I truly would not be where I am today without his unwavering support at every stage of my career. His mentorship has been invaluable, and I feel immensely fortunate to have had the opportunity to learn from him.

I am also profoundly grateful to my dissertation committee. I had the pleasure of knowing and working with each of you before graduate school, and your continued guidance and encouragement have been instrumental to my success at SIO. Dale Stokes, your enthusiasm and constant willingness to help and teach have been truly motivating. Sarah Purkey, your insights into the global biogeochemical picture and our discussions about BGC-Argo have been incredibly enriching and motivating. Ryan Kastner, your technical expertise and collaboration on Smartfin have opened new ways of thinking as an engineer but also as a scientist.

A special thanks to Yui Takeshita and the entire MBARI family—it was a privilege to work so closely with you all prior to, during and after my summer visit in 2022. I am grateful for all that I learned during my time with you and can't wait to see what is to come between our continued collaboration.

I also want to extend my thanks to all past and present members of the Martz Lab. You have all been a source of inspiration, and working alongside you has been both a joy and a motivator to pursue graduate school. I owe a particular debt of gratitude to Phil Bresnahan, my undergraduate mentor, whose belief in me gave me the opportunity to begin my journey in the Martz Lab and at SIO—thank you for that initial spark. It is amazing to be able to continue working with you all and I couldn't ask for a better academic family.

I want to thank my family: my mom, dad and sister for their utmost strength during the program. A very special thank you to my partner, Lauren, who has been my number one supporter throughout this entire process, always listening to my endless musings about sensors with patience and love. I couldn't have done this without you, and I am eternally grateful to have

you in my life during this challenging part of my life. Finally, a heartfelt thanks to my cats, Goldie and Pico, for their delightful distractions and for always keeping my workspace fluffy.

Chapter 1, in full, is currently being prepared for submission for publication of the material in *Nature: Science Data*. Wirth, T., Clements, S., Takeshita, Y., Carter, M., Bresnahan, P., Martz, T., Smith, J., 2024. A decade of near-shore pH data from the Scripps Ocean Acidification Real-Time (SOAR) Monitoring Program. The dissertation author was the primary investigator and author of this paper.

Chapter 2, in full, is a reprint of previously published material in *Limnology and Oceanography: Methods*. Wirth, T., Takeshita, Y., Davis, B., Park, E., Hu, I., Huffard, C.L., Johnson, K.S., Nicholson, D., Staudinger, C., Warren, J.K. and Martz, T., 2024. Assessment of a pH optode for oceanographic moored and profiling applications. The dissertation author was the primary investigator and author of this paper.

Chapter 3, in part, is currently being prepared for submission for publication of the material in *Geophysical Research Letters*. Wirth, T., Martz, T., 2024. Subsurface biogeochemical variability in the equatorial Pacific observed by BGC-Argo floats over the 2019-2024 El Niño/La Niña cycle. The dissertation author was the primary investigator and author of this paper.

VITA

2015 Bachelor of Science in Mechanical Engineering, Minor in Marine Science, University of California San Diego

2022 Master of Science in Oceanography, University of California San Diego

2024 Doctor of Philosophy in Oceanography, University of California San Diego

PUBLICATIONS

Wirth, T., Takeshita, Y., Davis, B., Park, E., Hu, I., Huffard, C. L., Johnson, K. S., Nicholson, D., Staudinger, C., Warren, J. K., & Martz, T. (2024). Assessment of a pH optode for oceanographic moored and profiling applications. *Limnology and Oceanography: Methods*, *n/a*(n/a). https://doi.org/10.1002/lom3.10646

Gonski, S. F., Luther, G. W., Kelley, A. L., Martz, T. R., Roberts, E. G., Li, X., Dong, B., Watson, J. A., **Wirth, T. S.**, Hussain, N., Feris Serrano, R. J., Hale, E., & Cai, W.-J. (2024). A half-cell reaction approach for pH calculation using a solid-state chloride ion-selective electrode with a hydrogen ion-selective ion-sensitive field effect transistor. *Marine Chemistry*, 104373. https://doi.org/10.1016/j.marchem.2024.104373

Bresnahan, P., Farquhar, E., Portelli, D., Tydings, M., **Wirth, T.**, & Martz, T. (2023). A Low-Cost Carbon Dioxide Monitoring System for Coastal and Estuarine Sensor Networks. *Oceanography*. https://doi.org/10.5670/oceanog.2023.s1.4

Shangguan, Q., Prody, A., **Wirth, T. S.**, Briggs, E. M., Martz, T. R., & DeGrandpre, M. D. (2022). An inter-comparison of autonomous in situ instruments for ocean CO2 measurements under laboratory-controlled conditions. *Marine Chemistry*, *240*, 104085. https://doi.org/10.1016/j.marchem.2022.104085

Shipley, K., Martz, T., Bresnahan, P., & **Wirth, T.** (2022). Metabolic rates in the Agua Hedionda Lagoon during the 2020 Southern California red tide event. *Elementa: Science of the Anthropocene*, *10*(1), 00018. https://doi.org/10.1525/elementa.2022.00018

Bresnahan, P., Cyronak, T., Brewin, R. J. W., Andersson, A., **Wirth, T.**, Martz, T., Courtney, T., Hui, N., Kastner, R., Stern, A., McGrain, T., Reinicke, D., Richard, J., Hammond, K., & Waters, S. (2022). A high-tech, low-cost, Internet of Things surfboard fin for coastal citizen science, outreach, and education. *Continental Shelf Research*, *242*, 104748. https://doi.org/10.1016/j.csr.2022.104748

Bresnahan, P. J., Takeshita, Y., **Wirth, T.**, Martz, T. R., Cyronak, T., Albright, R., Wolfe, K., Warren, J. K., & Mertz, K. (2021). Autonomous in situ calibration of ion-sensitive field effect transistor pH sensors. *Limnology and Oceanography: Methods*. https://doi.org/10.1002/lom3.10410

Wolfe, W., Shipley, K., Bresnahan, P., Takeshita, Y., **Wirth, T.**, & Martz, T. (2021). Technical Note: Stability of tris pH buffer in artificial seawater stored in bags. *Ocean Science Discussions*, 1–15. https://doi.org/10.5194/os-2020-120

Bresnahan, P. J., **Wirth, T.**, Martz, T., Shipley, K., Rowley, V., Anderson, C., & Grimm, T. (2020). Equipping smart coasts with marine water quality IoT sensors. *Results in Engineering*, *5*, 100087. https://doi.org/10.1016/j.rineng.2019.100087

Bresnahan, P. J., **Wirth, T.**, Martz, T. R., Andersson, A. J., Cyronak, T., D'Angelo, S., Pennise, J., Melville, W. K., Lenain, L., & Statom, N. (2016). A sensor package for mapping pH and oxygen from mobile platforms. *Methods in Oceanography*, *17*, 1–13. https://doi.org/10.1016/j.mio.2016.04.004

Frank, M. B., Naleway, S. E., **Wirth, T. S.**, Jung, J.-Y., Cheung, C. L., Loera, F. B., Medina, S., Sato, K. N., Taylor, J. R. A., & McKittrick, J. (2016). A Protocol for Bioinspired Design: A Ground Sampler Based on Sea Urchin Jaws. *JoVE (Journal of Visualized Experiments)*, *110*, e53554. https://doi.org/10.3791/53554

ABSTRACT OF THE DISSERTATION

Innovations in ocean biogeochemical instrumentation and monitoring

by

Taylor Wirth

Doctor of Philosophy in Oceanography

University of California San Diego, 2024

Professor Todd Martz, Chair

Anthropogenic activities are driving changes in ocean biogeochemistry, which can be monitored through instruments and sensors deployed across diverse platforms in even the harshest marine environments. Continued monitoring of these changes demands innovations in instrumentation, calibration and quality control to effectively capture dynamic signals and ensure comprehensive ocean coverage. This dissertation focuses on advancements in oceanographic pH sensors, starting with the longest near-continuous ocean pH dataset collected using ion-sensitive field effect transistor (ISFET) technology at Scripps Pier. A new in situ calibration approach, based on direct tris buffer injection, was compared to the traditional bottle collection

method, yielding a fourfold improvement in repeatability with an uncertainty of 0.006 pH. Additionally, an automated calibration system integrated into the sensor package was evaluated, offering near real-time, self-calibrating capability for ocean acidification and biogeochemical monitoring programs. To continue the discourse of pH sensor technology in the second section of this dissertation, a novel optical pH sensor was evaluated in laboratory settings to establish its accuracy and precision, response time, temperature and pressure sensitivity, and calibration techniques which improved accuracy over factory methods. Field tests of the optical pH sensor across diverse marine environments—deep ocean, dynamic nearshore, and open ocean profiling—provided guidelines for field calibration, correction and optimal field use. In a scaled-up sense, the final section of this dissertation leveraged pH and other biogeochemical sensors on BGC-Argo profiling floats to explore biogeochemical variability in the equatorial Pacific from 2019 to 2024. While the region has extensive physical data, subsurface biogeochemical observations and their links to El Niño and La Niña cycles are sparse. These floats revealed distinct biogeochemical patterns driven by vertical movement of the mixed layer depth, meridional subtropical water transport and primary production shifts associated with ENSO phases. Overall, this work combines new sensor technologies and analytical methods to provide essential data, instrument guidelines and reveal insights into ocean biogeochemical phenomena. Ongoing instrumentation development and monitoring will be critical to expand and deepen our understanding of how human-driven impacts are transforming our oceans.

Introduction

A changing ocean climate

The ocean is undergoing profound changes driven by human activities that are reshaping Earth's climate and ecosystems. The burning of fossil fuels, deforestation, and land-use modifications have had far-reaching impacts on both terrestrial and marine environments. Rising ocean temperatures have intensified El Niño events (Trenberth & Hoar 1997; Yeh et al. 2009; Shin et al. 2022), altered precipitation patterns and salinity (Durack et al. 2012; Konapala et al. 2020), and increased the frequency and strength of winds and storms (Sydeman et al. 2014; Kossin et al. 2020). These are just a few examples of the physical impacts affecting the ocean. However, intertwined with these physical changes, the ocean's biogeochemistry is also being altered.

Global ocean biogeochemical effects due to climate change, such as ocean deoxygenation (Keeling et al. 2010), disruptions to nutrient cycling and primary production (Marinov et al. 2010; Kwiatkowski et al. 2020), and transformations in the carbon cycle (Sarmiento et al. 1998; Doney et al. 2014), are all underway. A crucial aspect of ocean biogeochemistry is the carbon cycle and how the ocean's absorption of roughly one-third of atmospheric CO_2 (Sabine et al. 2004; Le Quéré et al. 2016) has led to a reduction in ocean pH, a process known as ocean acidification (Doney et al. 2009). Monitoring and understanding these biogeochemical changes have become increasingly dependent on advancements in sensor technologies. In particular, measuring the inorganic carbonate system, comprising pH, total alkalinity, dissolved inorganic carbon, and partial pressure of CO_2, is essential for tracking ocean acidification and broader changes in global carbon cycling (Byrne 2014; Wang et al. 2019). Among these variables, pH is the most accessible for measuring CO_2 changes in the ocean, thanks to recent innovations in sensor technology (Martz et al. 2015; Bushinksy et al. 2019).

Ocean pH instrumentation

Ocean pH instrumentation has evolved to include various types, yet this dissertation focuses on two critical pH sensing technologies in use today: the potentiometric ion-sensitive field effect transistor (ISFET), specifically the Durafet model from Honeywell, and the optical Pico-pH-SUB (Pico optode) from PyroScience GmbH (Martz et al. 2010; Johnson et al. 2016; Staudinger et al. 2018; Staudinger et al. 2019). These two sensors stand out as the only solid-state, scalable carbonate system sensors currently available. Their small size, pressure tolerance, low power consumption, and lack of moving parts or fluidics make them ideally suited for integration across a wide range of ocean observation platforms.

The Durafet has become central to global ocean pH monitoring programs, serving as the backbone for numerous long-term datasets (Rivest et al. 2016; Johnson et al. 2017; Claustre et al. 2020). However, in 2022, Honeywell discontinued the Durafet, creating a significant gap for the carbon observing community which relies on this technology for widespread monitoring. The Pico optode emerged as a promising alternative, offering a new approach to pH measurement but still required thorough assessment for oceanographic use.

Despite the advancements offered by new sensor technologies like the Pico optode, significant challenges remain in the validation and calibration of sensors in situ. Currently, the best practice for in-the-field calibration involves collecting seawater samples in bottles followed by laboratory-based pH analysis (Bresnahan et al. 2014). This approach, however, leaves room for improvement regarding the following:

- Spatiotemporal mismatch: Collecting the exact water measured by the sensor in dynamic ocean environments can be difficult, producing large errors between sensor and bottle sample (Hofmann et al. 2013; Bresnahan et al. 2021).
- Uncertainties in sample analysis: Recent work has shed light on global ship-based seawater carbonate measurement uncertainties, with more complications for coastal

environments showing that there is still work to be done to quantify and reduce bottle analysis uncertainties (Carter et al. 2023; Carter et al. 2024).

- Variability in user expertise: The accuracy of bottle measurements can vary depending on the experience and skill of the personnel involved, with larger errors due to more inexperienced users (McLaughlin et al. 2017).
- Resource intensity: Collecting and processing bottle data requires extensive personnel time, financial resources and specialty equipment, which many labs do not have (Martz et al. 2015).
- Time lag: Delays in obtaining and applying bottle calibration data can result in outdated calibration adjustments. For example, a month-long sensor deployment may not be corrected until bottle data is returned, sometimes many more months or years after the deployment.

Given these limitations, continued development in sensor technology, calibration techniques, and new methodologies is essential and further examined in this dissertation. Innovations will not only enhance sensor accuracy and reliability but also improve accessibility, ultimately ensuring the continued expansion of robust ocean pH and carbon monitoring.

Biogeochemical monitoring

The pH sensors previously mentioned are just one of many biogeochemical instruments used in ocean monitoring programs worldwide. Working alongside sensors capable of measuring oxygen, nutrients, chlorophyll, and particles, they collectively provide insights into the ocean's biogeochemical cycles (Gruber et al. 2009; Wang et al. 2019).

A flagship example of these technologies in concert is the Biogeochemical Argo (BGC-Argo program, a global initiative deploying biogeochemical sensors on an array of 1,000 profiling floats across the world's oceans (Johnson et al. 2009; Johnson & Claustre 2016; Chai et al. 2020). These profiling floats are autonomous platforms that sample the upper 2,000

meters of the ocean, transmitting their data back via satellite every 10 days, with each float designed to operate for around five years providing real-time data available for public use.

Through profiling floats, scientists have gained unprecedented insights into global ocean warming, shifts in the hydrological cycle, deoxygenation, and ocean acidification (Riser et al. 2016; Hosoda et al. 2009; Sharp et al. 2023; Mazloff et al. 2023). The ability to infer these global changes is directly tied to the efforts in developing these sophisticated sensors and the rigorous work required to ensure their performance and quality control (Bittig et al. 2019).

The ocean's cycles of nutrients and elements play a crucial role in regulating Earth's climate, ecosystems, and ocean chemistry (Falkowski et al. 2008, Gruber & Galloway 2008). Although significant research has advanced our understanding of these cycles, the complexity and variability of biogeochemical processes make them challenging to measure and model accurately. Ongoing biogeochemical monitoring and innovations in instrumentation will reinforce each other, enabling deeper exploration of hard-to-reach regions and continuous discoveries within the ocean's vast systems.

Dissertation outline

Chapter 1, in preparation and formatted for submission to *Nature: Science Data*, presents a decade-long time-series of ocean pH measurements at Scripps Pier from the Scripps Ocean Acidification Real-time (SOAR) Monitoring Program. To process the high frequency pH measurements, the chapter focuses on the evaluation of a novel alternative in situ calibration method, along with new tools and routines applicable to the wider pH sensor user community. The data set, currently the longest near-continuous time-series using an ISFET-based pH sensor, was rigorously quality-controlled and made available for public use for the first time since data collection began in 2014.

Chapter 2, published in *Limnology and Oceanography: Methods*, evaluates a new commercially available optical pH sensor by investigating its dependencies on temperature,

salinity, pressure, and characterizing response time, leading to the development of improved calibration procedures. Extensive field testing across multiple platforms enabled a thorough assessment of its performance in diverse ocean environments. Based on these results, new recommendations for sensor use were provided to the community which did not exist previously.

Chapter 3, in preparation and formatted for submission to *Geophysical Research Letters*, investigates subsurface biogeochemical variability in the remote equatorial Pacific Ocean using data collected by BGC-Argo profiling floats. It explores potential drivers of biogeochemical variability and examines the influence from the historic La Niña/El Niño cycles of 2019-2024.

References

Bittig, H. C., Maurer, T. L., Plant, J. N., Schmechtig, C., Wong, A. P. S., Claustre, H., Trull, T. W., Udaya Bhaskar, T. V. S., Boss, E., Dall'Olmo, G., Organelli, E., Poteau, A., Johnson, K. S., Hanstein, C., Leymarie, E., Le Reste, S., Riser, S. C., Rupan, A. R., Taillandier, V., Xing, X. (2019). A BGC-Argo Guide: Planning, Deployment, Data Handling and Usage. *Frontiers in Marine Science*, *6*. https://doi.org/10.3389/fmars.2019.00502

Bresnahan, P. J., Martz, T. R., Takeshita, Y., Johnson, K. S., & LaShomb, M. (2014). Best practices for autonomous measurement of seawater pH with the Honeywell Durafet. *Methods in Oceanography*, *9*, 44–60. https://doi.org/10.1016/j.mio.2014.08.003

Bushinsky, S. M., Takeshita, Y., & Williams, N. L. (2019). Observing Changes in Ocean Carbonate Chemistry: Our Autonomous Future. *Current Climate Change Reports*, *5*(3), 207–220. https://doi.org/10.1007/s40641-019-00129-8

Byrne, R. H. (2014). Measuring Ocean Acidification: New Technology for a New Era of Ocean Chemistry. *Environmental Science & Technology*, *48*(10), 5352–5360. https://doi.org/10.1021/es405819p

Carter, B. R., Sharp, J. D., Dickson, A. G., Álvarez, M., Fong, M. B., García-Ibáñez, M. I., Woosley, R. J., Takeshita, Y., Barbero, L., Byrne, R. H., Cai, W.-J., Chierici, M., Clegg, S. L., Easley, R. A., Fassbender, A. J., Fleger, K. L., Li, X., Martín-Mayor, M., Schockman, K. M., & Wang, Z. A. (2023). Uncertainty sources for measurable ocean carbonate chemistry variables. *Limnology and Oceanography*, *n/a*(n/a). https://doi.org/10.1002/lno.12477

Carter, B. R., Sharp, J. D., García-Ibáñez, M. I., Woosley, R. J., Fong, M. B., Álvarez, M., Barbero, L., Clegg, S. L., Easley, R., Fassbender, A. J., Li, X., Schockman, K. M., & Wang, Z. A. (2024). Random and systematic uncertainty in ship-based seawater carbonate chemistry observations. *Limnology and Oceanography*, *n/a*(n/a). https://doi.org/10.1002/lno.12674

Chai, F., Johnson, K. S., Claustre, H., Xing, X., Wang, Y., Boss, E., Riser, S., Fennel, K., Schofield, O., & Sutton, A. (2020). Monitoring ocean biogeochemistry with autonomous platforms. *Nature Reviews Earth & Environment*, *1*(6), 315–326. https://doi.org/10.1038/s43017-020-0053-y

Claustre, H., Johnson, K. S., & Takeshita, Y. (2020). Observing the Global Ocean with Biogeochemical-Argo. *Annual Review of Marine Science*, *12*(1), 23–48. https://doi.org/10.1146/annurev-marine-010419-010956

Doney, S. C., Bopp, L., & Long, M. C. (2014). Historical and Future Trends in Ocean Climate and Biogeochemistry. *Oceanography*, *27*(1), 108–119.

Doney, S. C., Fabry, V. J., Feely, R. A., & Kleypas, J. A. (2009). Ocean Acidification: The Other CO2 Problem. *Https://Doi.Org/10.1146/Annurev.Marine.010908.163834*, *1*, 169–192. https://doi.org/10.1146/ANNUREV.MARINE.010908.163834

Durack, P. J., Wijffels, S. E., & Matear, R. J. (2012). Ocean Salinities Reveal Strong Global Water Cycle Intensification During 1950 to 2000. *Science*, *336*(6080), 455–458. https://doi.org/10.1126/science.1212222

Falkowski, P. G., Fenchel, T., & Delong, E. F. (2008). The microbial engines that drive earth's biogeochemical cycles. *Science*, *320*(5879), 1034–1039. https://doi.org/10.1126/SCIENCE.1153213/ASSET/6B08817F-E1AD-4130-A430-2F3CBF3177F0/ASSETS/GRAPHIC/320_1034_F3.JPEG

Gruber, N., & Galloway, J. N. (2008). An Earth-system perspective of the global nitrogen cycle. *Nature 2008 451:7176*, *451*(7176), 293–296. https://doi.org/10.1038/nature06592

Gruber, N., Körtzinger, A., Alberto, B., Claustre, H., Doney, S. C., & Feely, R. A. (2009). *Toward an integrated observing system for ocean carbon and biogeochemistry at a time of change*. OceanObs'09: Sustained Ocean Observations and Information for Society. https://doi.org/10.5270/OceanObs09.pp.18

Hofmann, G. E., Smith, J. E., Johnson, K. S., Send, U., Levin, L. A., Micheli, F., Paytan, A., Price, N. N., Peterson, B., Takeshita, Y., Matson, P. G., Crook, E. D., Kroeker, K. J., Gambi, M. C., Rivest, E. B., Frieder, C. A., Yu, P. C., & Martz, T. R. (2011). High-Frequency Dynamics of Ocean pH: A Multi-Ecosystem Comparison. *PLOS ONE*, *6*(12), e28983. https://doi.org/10.1371/journal.pone.0028983

Hosoda, S., Suga, T., Shikama, N., & Mizuno, K. (2009). Global surface layer salinity change detected by Argo and its implication for hydrological cycle intensification. *Journal of Oceanography*, *65*(4), 579–586. https://doi.org/10.1007/s10872-009-0049-1

Johnson, K. S., Berelson, W. M., Boss, E. S., Chase, Z., Claustre, H., Emerson, S. R., Gruber, N., Körtzinger, A., Perry, M. J., & Riser, S. C. (2009). Observing biogeochemical cycles at global scales with profiling floats and gliders: Prospects for a global array. *Oceanography*, *22*(SPL.ISS. 3), 216–225. https://doi.org/10.5670/OCEANOG.2009.81

Johnson, K. S., & Claustre, H. (2016, November 8). *Bringing Biogeochemistry into the Argo Age*. Eos. http://eos.org/science-updates/bringing-biogeochemistry-into-the-argo-age

Johnson, K. S., Jannasch, H. W., Coletti, L. J., Elrod, V. A., Martz, T. R., Takeshita, Y., Carlson, R. J., & Connery, J. G. (2016). Deep-Sea DuraFET: A Pressure Tolerant pH Sensor Designed for Global Sensor Networks. *Analytical Chemistry*, *88*(6), 3249–3256. https://doi.org/10.1021/acs.analchem.5b04653

Johnson, K. S., Plant, J. N., Coletti, L. J., Jannasch, H. W., Sakamoto, C. M., Riser, S. C., Swift, D. D., Williams, N. L., Boss, E., Haëntjens, N., Talley, L. D., & Sarmiento, J. L. (2017). Biogeochemical sensor performance in the SOCCOM profiling float array. *Journal of Geophysical Research: Oceans*, *122*(8), 6416–6436. https://doi.org/10.1002/2017JC012838

Keeling, R. E., Körtzinger, A., & Gruber, N. (2010). Ocean deoxygenation in a warming world. *Annual Review of Marine Science*, *2*, 199–229. https://doi.org/10.1146/annurev.marine.010908.163855

Konapala, G., Mishra, A. K., Wada, Y., & Mann, M. E. (2020). Climate change will affect global water availability through compounding changes in seasonal precipitation and evaporation. *Nature Communications*, *11*(1), 3044. https://doi.org/10.1038/s41467-020-16757-w

Kossin, J. P., Knapp, K. R., Olander, T. L., & Velden, C. S. (2020). Global increase in major tropical cyclone exceedance probability over the past four decades. *Proceedings of the National Academy of Sciences*, *117*(22), 11975–11980. https://doi.org/10.1073/pnas.1920849117

Kwiatkowski, L., Torres, O., Bopp, L., Aumont, O., Chamberlain, M., Christian, J. R., Dunne, J. P., Gehlen, M., Ilyina, T., John, J. G., Lenton, A., Li, H., Lovenduski, N. S., Orr, J. C., Palmieri, J., Santana-Falcón, Y., Schwinger, J., Séférian, R., Stock, C. A., … Ziehn, T. (2020). Twenty-first century ocean warming, acidification, deoxygenation, and upper-ocean nutrient and primary production decline from CMIP6 model projections. *Biogeosciences*, *17*(13), 3439–3470. https://doi.org/10.5194/bg-17-3439-2020

Le Quéré, C., Andrew, R. M., Canadell, J. G., Sitch, S., Korsbakken, J. I., Peters, G. P., Manning, A. C., Boden, T. A., Tans, P. P., Houghton, R. A., Keeling, R. F., Alin, S., Andrews, O. D., Anthoni, P., Barbero, L., Bopp, L., Chevallier, F., Chini, L. P., Ciais, P., … Zaehle, S. (2016). Global Carbon Budget 2016. *Earth System Science Data*, *8*(2), 605–649. https://doi.org/10.5194/essd-8-605-2016

Marinov, I., Doney, S. C., & Lima, I. D. (2010). Response of ocean phytoplankton community structure to climate change over the 21st century: Partitioning the effects of nutrients, temperature and light. *Biogeosciences*, *7*(12), 3941–3959. https://doi.org/10.5194/bg-7-3941-2010

Martz, T., Daly, K., Byrne, R., Stillman, J., & Turk, D. (2015). Technology for Ocean Acidification Research: Needs and Availability. *Oceanography*, *25*(2), 40–47. https://doi.org/10.5670/oceanog.2015.30

Martz, T. R., Connery, J. G., & Johnson, K. S. (2010). Testing the Honeywell Durafet® for seawater pH applications. *Limnology and Oceanography: Methods*, *8*(5), 172–184. https://doi.org/10.4319/lom.2010.8.172

Mazloff, M. R., Verdy, A., Gille, S. T., Johnson, K. S., Cornuelle, B. D., & Sarmiento, J. (2023). Southern Ocean Acidification Revealed by Biogeochemical-Argo Floats. *Journal of Geophysical Research: Oceans*, *128*(5), e2022JC019530. https://doi.org/10.1029/2022JC019530

McLaughlin, K., Dickson, A., Weisberg, S. B., Coale, K., Elrod, V., Hunter, C., Johnson, K. S., Kram, S., Kudela, R., Martz, T., Negrey, K., Passow, U., Shaughnessy, F., Smith, J. E., Tadesse, D., Washburn, L., & Weis, K. R. (2017). An evaluation of ISFET sensors for coastal pH monitoring applications. *Regional Studies in Marine Science*, *12*, 11–18. https://doi.org/10.1016/j.rsma.2017.02.008

Riser, S. C., Freeland, H. J., Roemmich, D., Wijffels, S., Troisi, A., Belbéoch, M., Gilbert, D., Xu, J., Pouliquen, S., Thresher, A., Le Traon, P.-Y., Maze, G., Klein, B., Ravichandran, M., Grant, F., Poulain, P.-M., Suga, T., Lim, B., Sterl, A., … Jayne, S. R. (2016). Fifteen years of ocean observations with the global Argo array. *Nature Climate Change*, *6*(2), 145–153. https://doi.org/10.1038/nclimate2872

Rivest, E. B., O'Brien, M., Kapsenberg, L., Gotschalk, C. C., Blanchette, C. A., Hoshijima, U., & Hofmann, G. E. (2016). Beyond the benchtop and the benthos: Dataset management planning and design for time series of ocean carbonate chemistry associated with Durafet®-based pH sensors. *Ecological Informatics*, *36*, 209–220. https://doi.org/10.1016/j.ecoinf.2016.08.005

Sabine, C. L., Feely, R. A., Gruber, N., Key, R. M., Lee, K., Bullister, J. L., Wanninkhof, R., Wong, C. S., Wallace, D. W. R., Tilbrook, B., Millero, F. J., Peng, T.-H., Kozyr, A., Ono, T., & Rios, A. F. (2004). The Oceanic Sink for Anthropogenic CO2. *Science*, *305*(5682), 367–371. https://doi.org/10.1126/science.1097403

Sarmiento, J. L., Hughes, T. M. C., Stouffer, R. J., & Manabe, S. (1998). Simulated response of the ocean carbon cycle to anthropogenic climate warming. *Nature*, *393*(6682), 245–249. https://doi.org/10.1038/30455

Sharp, J. D., Fassbender, A. J., Carter, B. R., Johnson, G. C., Schultz, C., & Dunne, J. P. (2023). GOBAI-O2: Temporally and spatially resolved fields of ocean interior dissolved oxygen over nearly 2 decades. *Earth System Science Data*, *15*(10), 4481–4518. https://doi.org/10.5194/essd-15-4481-2023

Shin, N.-Y., Kug, J.-S., Stuecker, M. F., Jin, F.-F., Timmermann, A., & Kim, G.-I. (2022). More frequent central Pacific El Niño and stronger eastern pacific El Niño in a warmer climate. *Npj Climate and Atmospheric Science*, *5*(1), 1–8. https://doi.org/10.1038/s41612-022-00324-9

Staudinger, C., Strobl, M., Breininger, J., Klimant, I., & Borisov, S. M. (2019). Fast and stable optical pH sensor materials for oceanographic applications. *Sensors and Actuators B: Chemical*, *282*, 204–217. https://doi.org/10.1016/j.snb.2018.11.048

Staudinger, C., Strobl, M., Fischer, J. P., Thar, R., Mayr, T., Aigner, D., Müller, B. J., Müller, B., Lehner, P., Mistlberger, G., Fritzsche, E., Ehgartner, J., Zach, P. W., Clarke, J. S., Geißler, F., Mutzberg, A., Müller, J. D., Achterberg, E. P., Borisov, S. M., & Klimant, I. (2018). A versatile optode system for oxygen, carbon dioxide, and pH measurements in seawater

with integrated battery and logger. *Limnology and Oceanography: Methods*, *16*(7), 459–473. https://doi.org/10.1002/lom3.10260

Sydeman, W. J., García-Reyes, M., Schoeman, D. S., Rykaczewski, R. R., Thompson, S. A., Black, B. A., & Bograd, S. J. (2014). Climate change and wind intensification in coastal upwelling ecosystems. *Science*, *345*(6192), 77–80. https://doi.org/10.1126/science.1251635

Trenberth, K. E., & Hoar, T. J. (1997). El Niño and climate change. *Geophysical Research Letters*, *24*(23), 3057–3060. https://doi.org/10.1029/97GL03092

Wang, Z. A., Moustahfid, H., Mueller, A. V., Michel, A. P. M., Mowlem, M., Glazer, B. T., Mooney, T. A., Michaels, W., McQuillan, J. S., Robidart, J. C., Churchill, J., Sourisseau, M., Daniel, A., Schaap, A., Monk, S., Friedman, K., & Brehmer, P. (2019). Advancing Observation of Ocean Biogeochemistry, Biology, and Ecosystems With Cost-Effective in situ Sensing Technologies. *Frontiers in Marine Science*, *6*. https://doi.org/10.3389/fmars.2019.00519

Yeh, S.-W., Kug, J.-S., Dewitte, B., Kwon, M.-H., Kirtman, B. P., & Jin, F.-F. (2009). El Niño in a changing climate. *Nature*, *461*(7263), 511–514. https://doi.org/10.1038/nature08316

Chapter 1 A decade of near-shore pH data from the Scripps Ocean Acidification Real-time (SOAR) Monitoring Program

Taylor Wirth[1], Samantha Clements[1], Yuichiro Takeshita[2], Melissa Carter[1], Phillip Bresnahan[3], Todd Martz[1], Jennifer Smith[1]

Affiliations
1. Scripps Institution of Oceanography, University of California San Diego, La Jolla, CA, USA
2. Monterey Bay Aquarium Research Institute, Moss Landing, CA, USA
3. Department of Earth and Ocean Sciences, University of North Carolina Wilmington, Wilmington, NC, USA

Abstract

Monitoring and assessing long-term trends in coastal near-shore environments pose distinct challenges due to greater variability relative to the open ocean. The Scripps Ocean Acidification Real-time (SOAR) Monitoring Program has addressed these by collecting over a decade of high-frequency sensor pH measurements at the Ellen Browning Scripps Memorial Pier. This rigorously quality-controlled dataset incorporates calibration via both traditional bottle sampling methods and a novel approach using direct in situ injections of tris buffer in synthetic seawater, a traceable pH standard. The updated calibration procedures and methodology are further detailed, with the in situ tris buffer injection method achieving an accuracy of 0.006 pH. This near-continuous, high-quality pH time series offers a valuable resource for studying long-term trends and variability in the near-shore inorganic carbon system, contributing to ongoing ocean acidification monitoring efforts.

Background & Summary

Monitoring the ocean's inorganic carbon system is essential for understanding biogeochemical processes and assessing ocean health (Tanhua et al. 2019; Wanninkhof et al. 2021). The inorganic carbon system is typically characterized by four measurable parameters: pH, dissolved inorganic carbon (DIC), total alkalinity (TA), and the partial pressure of CO_2 (Dickson et al. 2007; Wang et al. 2019). Among these, pH has become a key focus of

measurement due to the availability of robust, efficient sensors that can be deployed across a wide range of oceanographic environments (Martz et al. 2015; Bushinsky et al. 2019).

Recent advancements in pH sensors, especially those based on ion-sensitive field-effect transistor (ISFET) technology (Martz et al. 2010; Bresnahan et al. 2014; Takeshita et al. 2014; Johnson et al. 2016), have enabled continuous, large-scale monitoring of the ocean's inorganic carbon system. These sensors are widely employed in regional to global monitoring networks such as the Global Ocean Acidification Observing Network (GOA-ON, Rivest et al. 2016) and the Biogeochemical Argo array (BGC-Argo, Claustre et al. 2020). However, despite technological progress, the calibration or remote delayed-mode quality control of sensors in situ remains a significant challenge (Carter et al. 2023, Wimart-Rousseau et al. 2024), and is the limiting factor in the reported accuracy of all autonomous datasets. Traditionally, ISFET pH sensors are calibrated using discrete bottle samples (Bresnahan et al. 2014), which introduces uncertainties due to potential spatio-temporal mismatches, sampling methods, and the inherent complexities of the inorganic carbon system (Hofmann et al. 2001; McLaughlin et al. 2017). Additionally, the time and cost required for laboratory analyses delay the ability to quality-control real-time data.

To address these limitations, use of tris buffer in synthetic seawater as a known pH reference, has been proposed as an alternative for in situ validation of ISFET-based pH sensors. This method involves directly injecting the buffer solution across the pH sensing surfaces within an enclosed flow cell. Tris buffer in synthetic seawater is widely used as a primary standard for oceanic pH measurements and has been extensively characterized across a range of temperatures, pressures, and salinity compositions (DelValls and Dickson, 1998; Rodriguez et al. 2015; Takeshita et al. 2017; Müller et al. 2018). Initially demonstrated on a short-term deployment (2 weeks) where the tris buffer injections (n=15) outperformed a rigorous bottle sampling campaign (n>100, Bresnahan et al. 2021), tris buffer offers a streamlined and

more consistent in situ calibration method, potentially reducing dependence on discrete bottle sample collection and the associated laboratory analysis.

In this study, we present a ten-year dataset of high-frequency pH measurements (~10-minute intervals) collected using a custom SeaFET sensor package deployed at Scripps Pier, La Jolla, CA, USA. The dataset, provided here, following rigorous quality control protocols, represents the first time these procedures have been fully developed and documented. We leverage the ~monthly concurrent collection of bottle samples and tris buffer injections to evaluate the long-term performance of in situ tris buffer calibration. Specifically, we compare tris-calibrated and bottle-calibrated SeaFET pH sensor data over an extended time-series, aiming to demonstrate that tris buffer calibration provides a more reliable and consistent method for sensor validation, particularly for real-time monitoring applications. A simultaneous goal of this research is to establish in situ tris buffer calibration as a scalable solution for high-frequency, continuous pH monitoring, which is essential for improving ocean carbon observations and supporting future marine carbon dioxide removal (mCDR) initiatives. By enhancing sensor accuracy and operational efficiency, this method can reduce the need for human intervention and workload, providing a robust framework for continued monitoring of ocean health in a changing climate.

The dataset offers a wide range of applications. It can be utilized to assess long-term ocean acidification trends, shedding light on how coastal regions are responding to global changes in atmospheric CO_2 levels (Duarte et al. 2013). Additionally, it allows for the investigation of dynamic processes such as upwelling and internal tides, which influence the local inorganic carbon system (Ribas-Ribas et al. 2001). The dataset also provides a valuable resource for times-series analysis of coastal carbon dioxide fluxes (Evans et al. 2022), and for exploring the impacts of climate variability, such as El Niño and La Niña cycles, on coastal carbon chemistry (Chavez et al. 2002; Lilly et al. 2019). The dataset also offers the opportunity to study the occurrence of harmful algal blooms (HABs) and red tides, events that can

significantly alter ocean biogeochemistry by impacting oxygen levels, and the local carbon system (Skelton et al. 2024). Understanding how these phenomena relate to pH variability and other environmental factors could provide insights into their drivers and potential links to broader climate patterns.

Methods

Sensor Operation

A custom SeaFET pH sensor package (SF, Bresnahan et al., 2014) used in this study (Figure 1.1). The sensor was mounted on a pier piling approximately 4 meters deep on the southeastern side of the Ellen Browning Scripps Pier in La Jolla, CA, USA (32° 52’ 1.5” N, 117° 15’ 26.5” W). The SF was deployed as part of the Scripps Ocean Acidification Real-time (SOAR) Monitoring Program from December 2013 to April 2024, comprised of 31 distinct deployments. The SF was relocated in July 2021 to a different piling approximately 20 meters away, at the same depth.

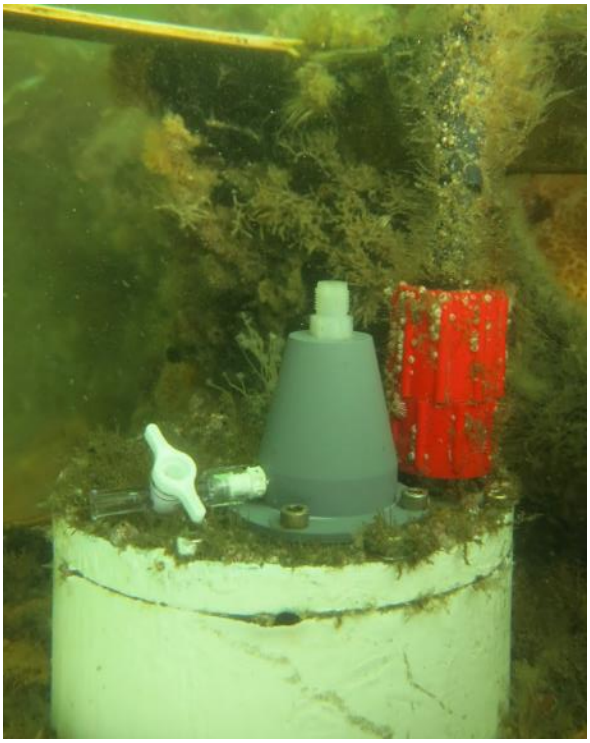

Figure 1.1: SeaFET deployed at Scripps Pier, with conical flow cell attached used for manual tris buffer injection.

The SF measured pH potentiometrically using the Honeywell DuraFET III combination electrode providing an “internal” reference and an Orion chloride ion-selective electrode (Cl-ISE) providing an “external” reference (Martz et al. 2010; Bresnahan et al. 2014; Takeshita et al. 2014). This arrangement provides two reference-source voltages and thus two pH values. We adopt the terminology used by Johnson et al. 2016 utilizing where the sensor calibration coefficients are referred to as “*k0*” and its temperature dependence “*k2*” (Johnson et al. 2018; Bresnahan et al. 2021). The SF’s reported pH in this study comes from the DuraFET internal reference with temperature from the DuraFET thermistor.

In situ calibration data

Two methods were used for in situ calibration to discrete samples of known pH: the traditional collection of seawater bottle samples and the injection of tris buffer into the flow cell of the pH sensors both manually and autonomously.

Seawater was collected using a clear, 2-liter diver-deployed Niskin bottle, transferred to a 500 mL borosilicate bottle using silicone tubing, and poisoned with 240 µL of saturated mercuric chloride within one hour of collection (n = 102; Dickson et al. 2007). The bottle samples were sent to three different laboratories for analysis during the study, depending on availability. Spectrophotometric measurements using m-cresol purple (mCP) were conducted, where two labs used purified mCP and the third used impure dye with a dye impurity correction applied (Carter et al. 2013; Takeshita et al. 2021). Some bottles were concurrently measured for total alkalinity (A_T) and total dissolved inorganic carbon (C_T). A_T was determined via open-cell titration following standard protocols (Dickson et al. 2003). C_T was determined either by coulometric titration[3] (Dickson et al. 2007) or by infrared detection after acidification and CO_2 stripping (Goyet and Snover, 1993; O’Sullivan and Millero, 1998).

For the tris buffer injections, 120 mL of tris buffer was manually injected into a custom conical 25-mL flow manifold installed by scuba divers at time of calibration. The injection was performed using two 60-mL syringes, with a check valve on the outlet to prevent any mixing with

ambient seawater during the measurement process. Both certified tris buffer from the lab of Andrew Dickson at Scripps Institution of Oceanography and self-made tris buffer (Paulsen & Dickson 2020) were utilized.

Calibration procedure

Two methods were used to calibrate sensor pH to the in situ discrete samples: a single-point or mean *k0* value or a linearly fitted *k0* value. Both methods require calculating *k0* using known in situ pH values from the discrete sample data (bottle and tris), internal reference voltage, and temperature at the time of discrete sample collection.

Bottle pH was converted to in situ pH using CO2SYS V3 (Lewis & Wallace 1998; Sharp et al. 2023), with spectrophotometric pH and A_T as input parameters. Bottle salinity was determined by a salinometer and in situ temperature was determined from the SF at time of seawater collection. Nutrient concentrations were set to zero, with K1 and K2 dissociation constants from Lueker et al. 2000, KSO4 dissociation constant from Dickson 1990, KHF dissociation constant from Perez & Fraga 1987, and the boron-salinity ratio from Lee et al. 2010 as recommended for best practice (Orr et al. 2018; Jiang et al. 2022). If bottle A_T was unavailable, A_T was estimated using a linear salinity-A_T regression determined from the bottle samples in this study.

Tris buffer in situ pH was calculated from DuraFET temperature at the time of injection, and a practical salinity of 35 using Eq. 18 from DelValls & Dickson 1998.

During most deployments, multiple bottles were collected and tris buffer injections performed (~monthly), providing 4 choices for in situ sensor calibration: mean bottle *k0*, mean tris *k0,* linear bottle *k0*, or linear tris *k0*. The rationale for the chosen calibration method is discussed below (Figure 1.2, and in the section below). All deployments were individually processed, using a customized graphical user interface (GUI) developed for this dataset.

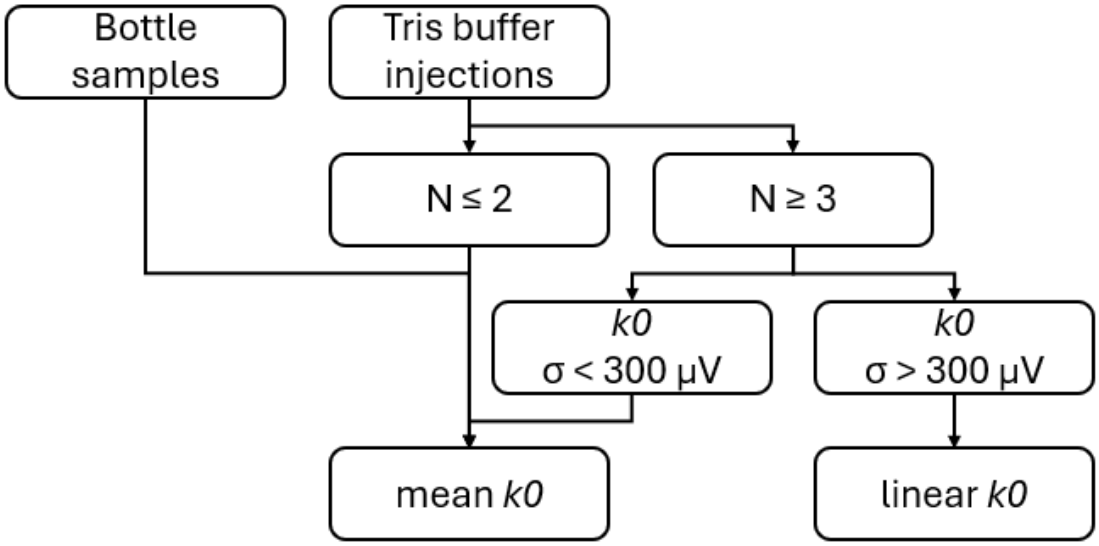

Figure 1.2: Decision tree for selecting the in situ sensor calibration method based on bottle samples and tris buffer injections. The number of tris buffer injections (N) and the standard deviation (σ) of the calibration coefficient (k0) warrant either a single k0 or linear k0 to be applied to the deployment.

Calibration example

Regarding bottle samples for calibration use, we keep with the best practices of using a mean (single) *k0* value, regardless of quantity of bottles collected during the deployment (Bresnahan et al. 2014; 2021). For the remainder of this study, we focus on the tris buffer injection calibration method. A mean *k0* value was also used for tris buffer injections if:

1) 2 or less tris injections were performed.
2) Or the standard deviation of the *k0* values was less than 300 µV. This standard deviation value was chosen as it equates to ~0.006 pH, which is the reported uncertainty of the self-made tris buffer (Paulsen & Dickson 2020) and was the standard deviation seen during the study by Bresnahan et al. 2021 for the DuraFET internal reference calibrated to tris buffer.

Figure 1.3a illustrates an example stable deployment that justifies the use of a mean tris buffer *k0* as all *k0* values (σ = 130 µV) fell within the 300 µV standard deviation threshold. Typically, tris injections for most deployments exhibited standard deviations well within this threshold,

supporting the use of a mean *k0* (N = 21). However, in some cases (N = 10), standard deviations exceeded 300 µV, with a visible linear drift that aligned with the trend observed in bottle samples.

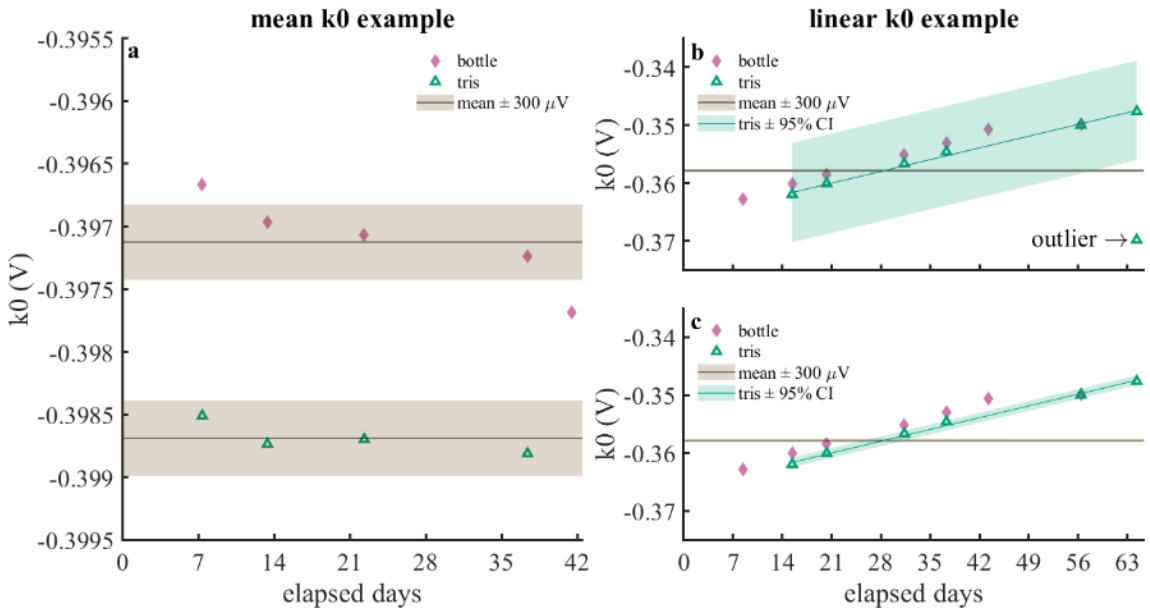

Figure 1.3: Examples of k0 values from bottles (purple diamonds) and tris buffer injections (green triangles) from two deployments: (a) Stable deployment with mean k0 ± 300 µV (black line with tan shaded region) shown for both bottles and tris buffer. Tris buffer k0 values are within ± 300 µV suggesting the use of a mean tris buffer k0 value for this deployment. (b) Drifting deployment with robust linear regression and 95% confidence interval (CI; green line with green shaded region) fit to tris buffer injections including the outlier. Note the narrow mean ± 300 µV (black line with tan shaded region) for this deployment, calculated for tris buffer only. (c) Same as (b) but with normal linear regression fit to tris buffer injections excluding the outlier.

Here we outline the steps used to apply a linear *k0* correction for sensor drift, as has been previously demonstrated for BGC-Argo floats (Johnson et al. 2018). This correction was applied exclusively to tris buffer injections, which provide a direct measure of a known pH without the risk of spatio-temporal mismatch, offering improved consistency over bottle measurements (Bresnahan et al. 2021).

If the standard deviation of tris measurements exceeded 300 µV, *k0* and thus sensor drift was likely (Figure 1.3b). To perform a linear regression, at least three tris buffer injections were required during a deployment. This allowed for the calculation of goodness-of-fit statistics, the identification of potential outliers, and the confirmation that multiple injections exhibited the

same drift direction, ruling out faulty injections. The following steps were taken to apply a linear *k0* calibration for this example (Figure 1.3b):

1) Calculated *k0* values for the tris buffer injections (N = 6; σ = 7.2 mV). Standard deviation was well outside the 300 µV threshold.
2) Visually confirmed if there was a trend in *k0* values and its consistency to the bottle samples.
3) Fitted a robust linear regression (Figure 1.3b). R^2 = 0.745 and 95% confidence interval = 8.0 mV (CI).
4) Identified and removed outliers greater than 2 standard deviations or outside the 95% CI.
5) Refitted a normal linear regression (Figure 1.3c). R^2 = 0.996 and 95% CI = 860 µV.
6) Noted improvement in R^2 value and reduction in the 95% CI, indicating significance of the outlier.
7) Applied this linear *k0* over the duration of the deployment (V/time). To compare to our 300 µV standard deviation threshold for mean k0 deployments, the RMSE for this example was 430 µV.

Using the outlined methodology, we present two example deployments demonstrating the application of a mean and linear *k0* derived from tris buffer injections. Bottle samples are included to validate the alignment between sensor and bottle data following calibration to the tris buffer.

In the stable deployment example (Figure 1.4a), residuals for the mean *k0* of the tris injections remained near zero with a standard deviation of 128 µV (~0.002 pH). Residuals relative to the bottle samples showed an offset of 0.027 ± 0.007 pH. The SF data exhibited a maximum difference of 0.003 pH whether the mean or linear *k0* was used for calibration (Figure 1.4b). This negligible difference, within the uncertainty of tris buffer preparation (<0.006 pH), suggests that using a mean *k0* was appropriate for this deployment.

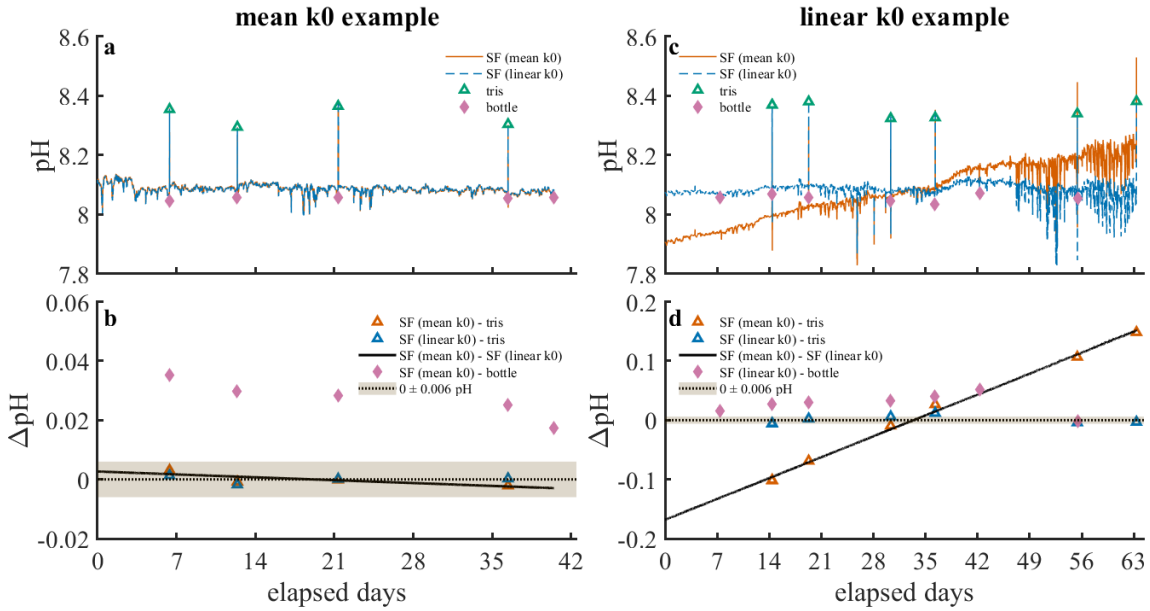

Figure 1.4: Example deployments showing the use of a mean or linear k0. (a) SeaFET (SF) data from a stable deployment calibrated to tris buffer injections using a mean k0 (orange line) and a linear k0 (blue dashed line). In situ tris buffer pH (green triangles) and bottle sample pH (purple diamonds) also shown. (b) Residuals between the SF using both k0 values and the tris buffer injections (triangles), difference between SF data calibrated to mean and linear k0 (black line), and residuals between SF calibrated to the mean k0 and bottle samples (purple triangles). The dashed line and tan shaded region represent a difference of 0 ± 0.006 pH corresponding to the k0 standard deviation threshold of 300 µV. (c) Same as (a) but for a drifting deployment warranting the use of a linear k0 value. (d) Same as (b) for the drifting deployment shown in (c) but the residuals between the SF calibrated to the linear k0 and bottle samples are shown.

In the drifting deployment example (Figure 1.4c), calibration of the SF using a mean *k0* revealed significant drift, as residuals between the SF and in situ tris buffer pH exhibited a clear, linearly increasing trend (Figure 1.4d). A similar trend was observed in the residuals for the in situ bottle sample pH, with a maximum deviation up to 0.15 pH. In contrast, when the SF time series was calibrated using a linear *k0* to adjust to the in situ tris buffer pH, it also showed much closer alignment with the bottle samples. Residuals between the SF (calibrated with a linear *k0*) and tris buffer were 0.000 ± 0.007 pH, while residuals for the bottle samples displayed the same offset observed previously, at 0.028 ± 0.017 pH.

The contrast between calibrating with a mean versus linear *k0* underscores the importance of selecting an appropriate calibration method, as the goal is to maintain sensor

consistency across both tris buffer and bottle sample comparisons. This example highlights the efficacy of the linear *k0* to correct for sensor drift, ensuring sensor data reliability over time.

Data records

SOAR pH time-series

The decade-long (Dec 13, 2013 – April 17, 2024) data set of sensor pH is archived by the University of California San Diego Library. The data set provides comma-separated values (.csv) and MATLAB MAT-file (.mat) of sensor pH data corrected to the in situ tris buffer injections according to our methodology outlined above, as well as secondary pH data corrected to the bottle data. Datetime data is provided in Coordinated Universal Time. Raw sensor voltage and temperature is also provided to allow recalculation of sensor pH data using the in situ calibration data of choice. The calibration coefficients used, and calculated for all four methodologies is also provided. Quality-control (QC) flags for the sensor pH data corrected to the tris buffer injections are provided as follows:

- 1 = good data
- 2 = bottle sample collected during this measurement
- 3 = tris buffer injected during this measurement
- 4 = bad data.

The time series of SeaFET pH data corrected to the tris buffer injections, using QC flags of 1 and 2, is shown in Figure 1.5.

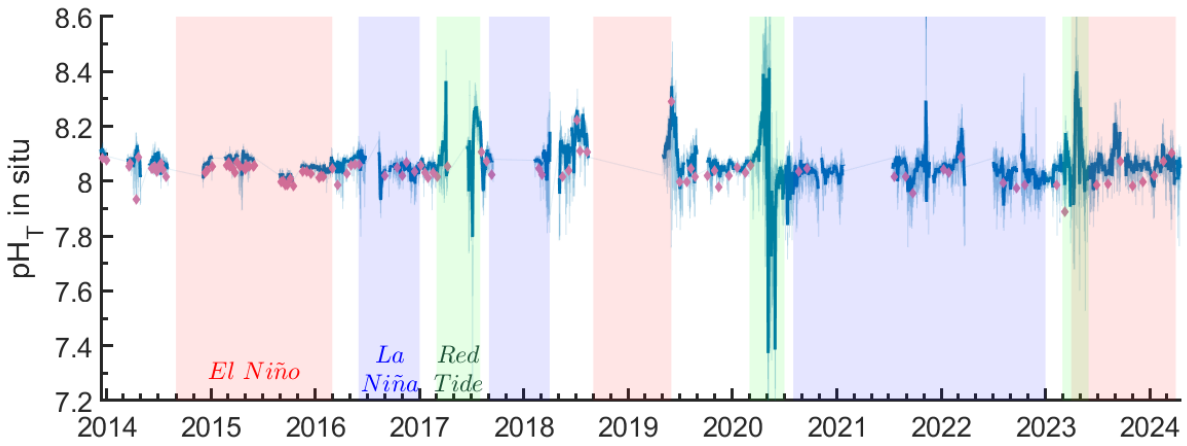

Figure 1.5: Scripps Ocean Acidification Real-time (SOAR) Monitoring Program time-series of SeaFET pH calibrated to in situ tris buffer injections. Light blue line represents high-frequency data, bold blue line is the daily average. Bottle samples (purple diamonds) are also shown.

Bottle sample data

Bottle data is archived by the University of California San Diego Library. The data set provides comma-separated values (.csv) and MATLAB MAT-file (.mat) of the spectrophotometric pH, temperature (°C) from the spectrophotometric analysis, salinity (PSU), A_T (µmol kg^{-1}), C_T (µmol kg^{-1}), and calculated in situ pH. Datetime data is provided in Coordinated Universal Time.

Tris buffer metadata

Tris buffer injection data is archived by the University of California San Diego Library. The data set provides comma-separated values (.csv) and MATLAB MAT-file (.mat) of the datetime of tris buffer injection, in Coordinated Universal Time, temperature (°C), and calculated in situ pH of the tris buffer. Raw sensor voltage (Vint, volts) used in this data set to calculate the calibration coefficients is also included.

Technical validation

Tris buffer vs bottle sample bias

The data set provided an unprecedented opportunity to compare tris buffer injections with the traditional bottle sample calibration method for calibrating ISFET pH measurements. Generally, the sensor pH data tracked well with the bottle samples, indicating that correcting

sensor pH to the tris buffer injections was a valid calibration method. However, a consistent offset of 0.026 pH units was observed between sensor data when corrected to the tris buffer and the bottle pH, suggesting that the bottle pH was consistently lower than expected compared to in situ pH values from the tris buffer (Figure 1.6a).

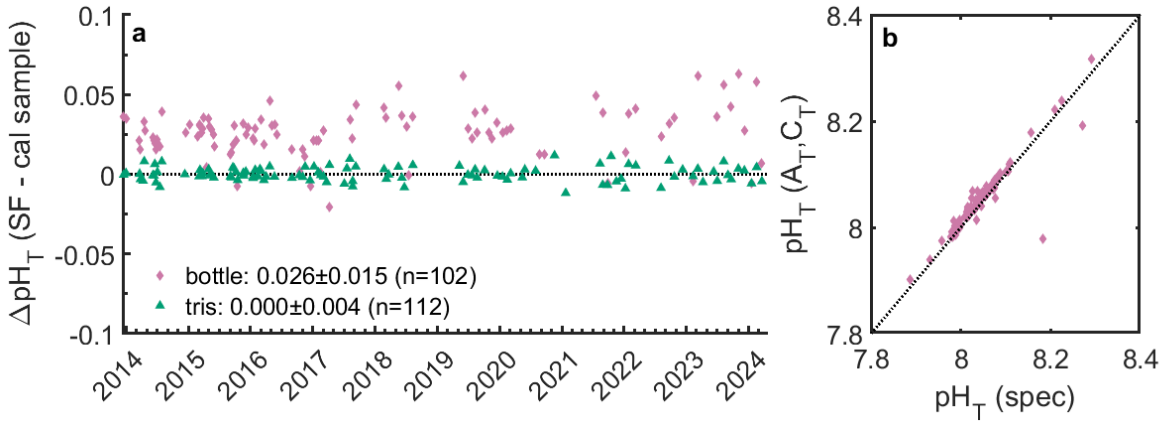

Figure 1.6: (a) Residuals (mean ± 1σ) between the SeaFET (SF, calibrated to tris buffer) and the in situ tris buffer pH (green triangles) and bottle sample in situ pH values from spectrophotometric analysis (purple diamonds).(b) Property-property plot of bottle sample in situ pH calculated from total alkalinity (A_T) and total dissolved inorganic carbon (C_T) vs in situ spectrophotometric pH. Dashed line is 1:1.

This offset persisted throughout the entire decade-long time series, with no observed differences across tris buffer batches, laboratories performing spectrophotometric analysis, sample collectors, or bottle shelf life, which ranged from six months to two years. This bias is equivalent to residuals seen in several studies: ~0.03 pH from Bresnahan et al. 2014 and Velo & Padin et al. 2022, 0.04 pH from Gonski et al. 2018, and better than the residuals seen in these studies: 0.08 from McLaughlin et al. 2017, up to 0.1 from Miller et al. 2018. In contrast, the bias seen from the only previous study using in situ tris buffer injections was 0.008 pH at Lizard Island, Australia (Bresnahan et al. 2021).

Furthermore, the standard deviation of the residuals of the tris buffer injections (0.004 pH) compared to the bottle samples (0.015 pH) demonstrated approximately a fourfold improvement in calibration precision, on par with those seen previously (Bresnahan et al. 2021). Based on the uncertainty of tris buffer preparation (0.006 pH, Paulsen and Dickson 2020) and the standard deviation of SF-tris buffer residuals (0.004 pH), the accuracy of the data set is

reported as 0.006 pH units. Overall, the observed offset between tris and spectrophotometric pH corrected sensor data may be location-dependent, with uncertainties in the spectrophotometric analysis and CO2SYS calculations likely playing a major role in attributing to the 0.026 offset.

A persistent discrepancy of ~0.01 pH was observed in the bottle samples when comparing in situ pH determined spectrophotometrically with that calculated from A_T and C_T (Figure 1.6b). This discrepancy aligns with those from global shipboard measurements (Carter et al. 2023), although those were conducted in the open ocean. Given the greater variability in coastal carbonate chemistry, this suggests that uncertainties related to unidentified A_T sources in coastal environments may contribute to the discrepancy, requiring further research for characterization and determination (Carter et al. 2024).

Calibration coefficient k0 variability

Across the 31 deployments, 9 DuraFET sensors were deployed, yielding a mean *k0* value of -0.3712 ± 0.0111 V based on tris buffer calibrations for the time series (Figure 1.7a). In the 10 deployments using a linear *k0*, drift rates ranged from 8 to 329 µV/day (Figure 1.7b). Excluding the highest outlier, the average drift rate was 30 µV/day, suggesting that it would take approximately 10 days to exceed the 300 µV standard deviation threshold (~0.006 pH) to support using a linear *k0*.

Two deployments exhibited negative drift, but these also had some of the lowest drift rates and mean *k0* standard deviation. For these cases, it would take roughly 30 days to surpass the 300 µV threshold. Overall, for the deployments with linear *k0* corrections, the root mean square error (RMSE) for sensor data compared to tris buffer in situ pH was 0.006 pH. In contrast, using a mean *k0* for the drifting deployments resulted in a *k0* standard deviation of 0.0011 V, increasing the sensor-tris buffer RMSE to ~0.018 pH. This indicates that while most

the deployments that experienced drift were significant, they were robustly correctable to maintain the reported accuracy of the tris buffer injection calibration method of 0.006 pH.

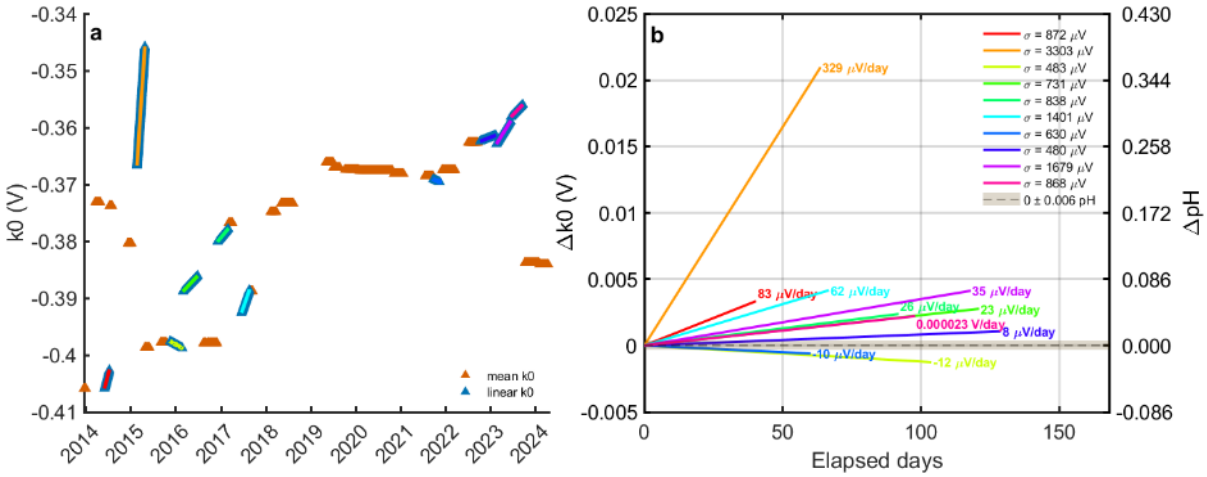

Figure 1.7: (a) Calibration coefficient k0 for tris buffer injections used throughout the time-series. Orange triangles represent when a mean k0 value was used (n=21) and blue triangles represent when a linear k0 was used (n=10). The multi-color lines represent the drift rates for the linear k0 deployments. (b) Drift rates of k0. Line color corresponds to deployments in in (a). Legend shows standard deviation of k0 values of the tris buffer injections before linear correction applied (i.e. > 300 μV threshold).

Using the outlined methodology with a linear *k0* approach, it is important to note that deployments should exceed 30 days to confidently determine if the sensor is drifting, and whether the drift is occurring at a consistent rate and in the same direction across three or more tris buffer injections. Nonlinear drift, or piece-wise drift, as observed in profiling applications (Johnson et al. 2018; Maurer et al. 2021), was not present in any of the deployments used to generate this dataset. Due to the constant pressure experienced by the sensor in fixed or moored applications, it is expected to only experience linear drift on occasion.

Comparison to Self-Calibrating SeapHOx

The Self-Calibrating SeapHOx (SCS), first described and tested by Bresnahan et al. 2021, is identical to the SF but includes an oxygen optode (Aanderaa 5730) and conductivity sensor (Seabird SBE37SI). The SCS was also mounted on a nearby pier piling, at four meters depth. The SCS, deployed from February 2022 to October 2023, comprised of four distinct deployments. Additionally, the SCS uses a pump (Seabird 5P) for active flushing to limit biofouling and has the unique capability to collect fully automated in situ calibration

measurements. For intercomparison and consistency, we also report the SCS's pH from its internal reference using the temperature measurement from the collocated oxygen optode.

The SCS automates the injection of tris buffer from a flexible gas-permeable bag (Wolfe et al. 2021), eliminating the need for human intervention (Bresnahan et al. 2021). This system incorporates a pressure equilibrated 3-way valve to seamlessly and programmatically switch between seawater and tris buffer measurements. The SCS used self-made tris buffer, which was subjected to spectrophotometric testing for quality assurance. This testing confirmed that the pH of the self-made buffer was within 0.006 pH units of the spectrophotometric value (Paulsen & Dickson, 2020).

When deployed alongside for ~1.5 years, the pH data from the two sensors closely matched, despite utilizing separate systems for tris buffer injection (Figure 1.8a). The residuals between the sensors were 0.005 pH units, within the reported accuracy of the tris buffer injection method. The largest discrepancy occurred during the April 2023 red tide event, likely due to differences in flushing mechanisms. The passive system of the SF may have trapped phytoplankton during the bloom, amplifying the high pH signal during a time of high productivity.

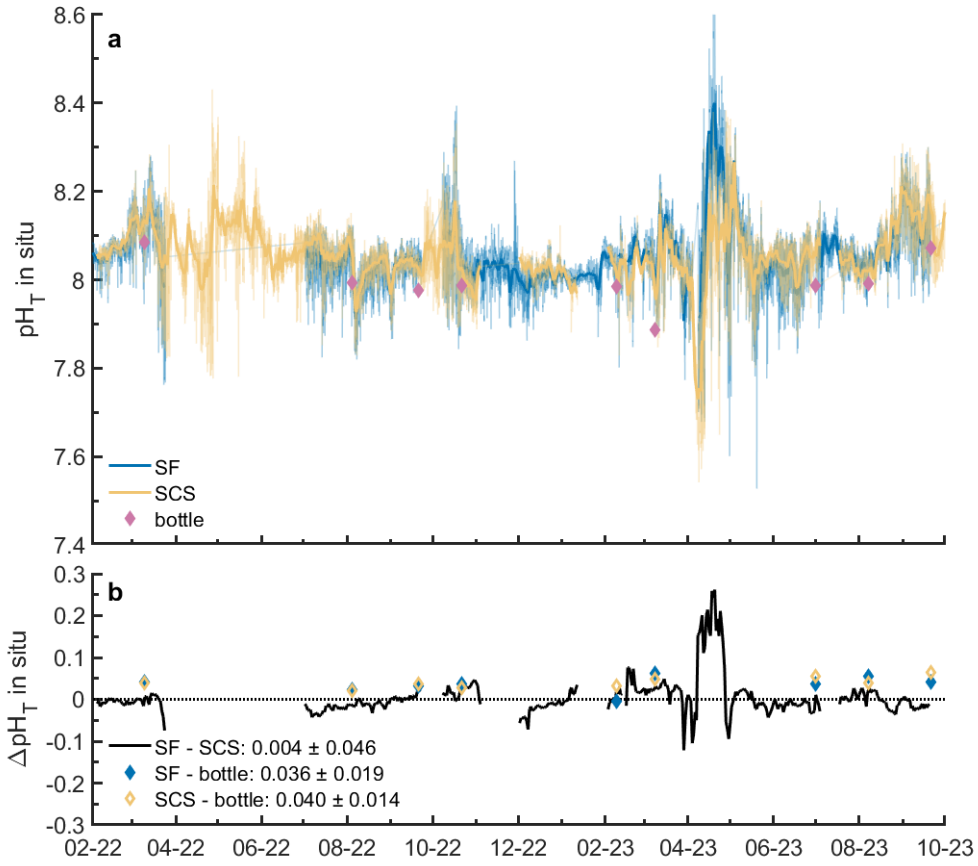

Figure 1.8: (a) Time-series of the SOAR SeaFET data (SF, blue line) and the Self-Calibrating SeapHOx (SCS, gold line), both corrected to their respective in situ tris buffer injections. Bottle samples (purple diamonds) are shown. (b) Residuals between the SF and SCS (black line), SF and bottle (blue diamonds), SCS and bottle (gold diamonds). Legend shows the mean ± 1σ of each residual.

Residuals between both sensors and bottle samples were similarly consistent, 0.036 for the SF compared to 0.040 for the SCS during this period, confirming that the tris buffer calibration method is robust and repeatable across different sensor packages and injection systems (Figure 1.8b). It is important to note that this offset is larger than that seen for the entire dataset, which was 0.026 pH, revealing a potential increasing trend over the time of the bias between tris buffer and bottles. The injection of tris buffer for the SeaFET highlighted the effectiveness of this calibration technique, though it demands considerable human involvement, including scuba diving, the installation of a specialized flow cell, and manual injection via syringe. In contrast, the SCS's automated injection system removes the necessity for manual

handling, providing high-quality in situ calibration data directly when utilized in a real-time monitoring system.

Ocean acidification trend

To further validate the time-series dataset, ocean acidification trends were estimated for the three time-series available: (1) SeaFET sensor pH data corrected using tris buffer injections, (2) SeaFET pH data corrected to bottle samples, and (3) the in situ pH of bottle samples (Figure 1.9). No detrending was performed, in accordance with best practices for estimating ocean acidification trends (Sutton et al. 2022). This evaluation was conducted solely to demonstrate that the relative accuracy of our methods was consistent, and that all methods captured the same variability and trend in the in situ data.

The linear trends for all three time-series were comparable. The tris-corrected SeaFET data showed a trend of -0.0023 pH $year^{-1}$, while the bottle-corrected SeaFET data indicated a trend of -0.0027 pH $year^{-1}$. The trend for the bottle samples alone was identical to that of the SeaFET data corrected to bottle samples, which is expected, as the sensor data was calibrated to the bottle data.

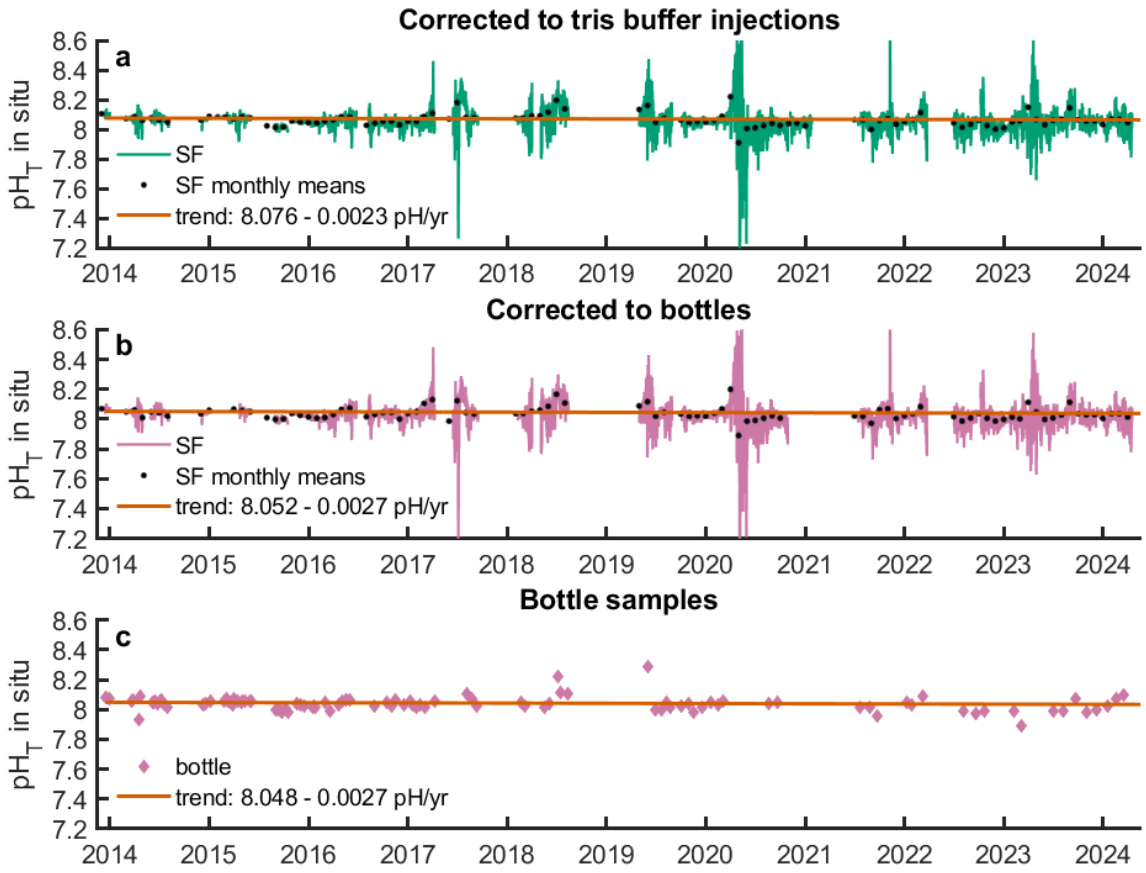

Figure 1.9: (a) Time-series of SeaFET sensor pH corrected to tris buffer injections (gold line) and monthly means (black dots). Linear trend (orange line) fitted to the sensor data, legend shows y-intercept and slope trend. (b) same as (a) but for SeaFET sensor pH corrected to bottle samples. (c) Bottle in situ pH (blue dots).

These trends are consistent with those observed in other long-term monitoring programs around the world (Doney et al. 2009; Bates et al. 2014; Ishida et al. 2021; Ma et al. 2023; Wolfe et al. 2023). The y-intercept offset, or bias, between the two SeaFET time-series differed by 0.024, which was equivalent to the bias between the sensor pH data corrected to tris buffer injections and the in situ pH from bottle samples seen in the above sections.

To reiterate, these results indicate that regardless of the absolute accuracy of the calibration method—whether corrected using tris buffer injections or bottle samples—the observed variability and long-term trend remained consistent.

Conclusion

This study provides a decade-long dataset of sensor pH measurements from the Scripps Ocean Acidification Real-time (SOAR) Monitoring Program with concurrent bottle sample data and tris buffer injection metadata. The archived data, covering the period from December 13, 2013, to April 17, 2024, is accessible through the University of California San Diego Library. The dataset highlights sensor pH data corrected using in situ tris buffer injections, with a reported accuracy of 0.006 pH. Quality control (QC) flags ensure data integrity, providing clear classifications for data quality.

The technical validation of the sensor pH data when calibrated to the tris buffer injections revealed a consistent offset of 0.026 pH when compared to the bottle samples. The magnitude of this offset is in line with previous studies, indicating that the tris buffer calibration approach provides consistent and reliable results. The offset is of concern, as proving the efficacy of the tris buffer injection calibration method relies on obtaining equal accuracy proven by best practices of comparing in situ sensor pH to spectrophotometric values (Martz et al. 2010; Bresnahan et al. 2014; Takeshita et al. 2014). Further research is required to determine the source of this offset, including the discrepancy of the near-shore relationship between A_T and C_T in the determination of in situ pH (Carter et al. 2024).

The comparative time-series from the Self-Calibrating SeapHOx showcased the reliability and consistency of the tris buffer calibration across separate sensor packages, underscoring the advancements in the automated calibration system. The closely aligned pH readings from both sensors, along with equivalent residuals to bottle samples, confirm that there is no significant difference between the tris injection methods. The continued use of the Self-Calibrating SeapHOx is an obvious choice, as it eliminates the need for manual intervention while ensuring the highest-quality in situ calibration for ISFET-based pH sensors, making it indispensable for non-expert users and long-term monitoring programs.

Additionally, the brief evaluation of ocean acidification trends showed a decrease of -0.0023 pH year^{-1}, utilizing the tris buffer-corrected SeaFET data. This trend was comparable to that observed in the bottle-corrected SeaFET data, and the bottle samples alone. This consistency across the multiple datasets emphasizes the reliability of both calibration methods in capturing the same long-term trend.

Overall, the dataset contributes to a deeper understanding of ocean biogeochemistry and highlights the significance of high-quality pH measurements in monitoring ocean acidification. Further refinement is needed to confidently claim the “climate” quality uncertainty goal of 0.003 pH uncertainty for a long-term sensor dataset such as this (Newton et al. 2015). In the end, the accessibility of this comprehensive dataset supports ongoing research efforts and underscores the importance of innovative calibration techniques in enhancing the quality of ocean monitoring programs.

Code availability

Code and the graphical user interface (GUI) application used to process individual deployment files that make up the entirety of this dataset are freely available on GitHub (https://github.com/taylorwirth4/ISFET_APP). The GUI reads in the sensor data file, a file for tris injection meta data, and separate bottle sample data file. Example files with required formats are given. The GUI outputs calibrated pH, corrected to either the bottles and/or tris buffer depending on user preference, along with a pdf summary of the procedure for documentation and note keeping. The GUI can be used for bottle or tris injections separately, requiring the user to specify calling the “null” data file provided for the respective calibration data they do not have or wish to use.

Acknowledgments

The Scripps Ocean Acidification Real-time (SOAR) Monitoring Program is supported by the Kathy and William Scripps Family Foundation, the Bohn Family, and the Ellen Browning

Scripps Foundation. Many individuals contributed to the data collection over its lifetime, including Susan Kram, Kayla Martin, Elena Beckhaus, Dalton Rust, Jimmy Fumo and the collaborators from the Southern California Coastal Ocean Observing System (SCCOOS). Many thanks to the multitude of volunteer scuba divers who accompanied those doing the in situ tris buffer injections.

Chapter 1, in full, is currently being prepared for submission for publication of the material in *Nature: Science Data*. Wirth, T., Clements, S., Takeshita, Y., Carter, M., Bresnahan, P., Martz, T., Smith, J., 2024. A decade of near-shore pH data from the Scripps Ocean Acidification Real-Time (SOAR) Monitoring Program. The dissertation author was the primary investigator and author of this paper.

References

Bates, N. R., Astor, Y. M., Church, M. J., Currie, K., Dore, J. E., González-Dávila, M., Lorenzoni, L., Muller-Karger, F., Olafsson, J., & Santana-Casiano, J. M. (2014). A Time-Series View of Changing Surface Ocean Chemistry Due to Ocean Uptake of Anthropogenic CO_2 and Ocean Acidification. *Oceanography*, *27*(1), 126–141.

Bresnahan, P. J., Martz, T. R., Takeshita, Y., Johnson, K. S., & LaShomb, M. (2014). Best practices for autonomous measurement of seawater pH with the Honeywell Durafet. *Methods in Oceanography*, *9*, 44–60. https://doi.org/10.1016/j.mio.2014.08.003

Bresnahan, P. J., Takeshita, Y., Wirth, T., Martz, T. R., Cyronak, T., Albright, R., Wolfe, K., Warren, J. K., & Mertz, K. (2021). Autonomous in situ calibration of ion-sensitive field effect transistor pH sensors. *Limnology and Oceanography: Methods*. https://doi.org/10.1002/lom3.10410

Bushinsky, S. M., Takeshita, Y., & Williams, N. L. (2019). Observing Changes in Ocean Carbonate Chemistry: Our Autonomous Future. *Current Climate Change Reports*, *5*(3), 207–220. https://doi.org/10.1007/s40641-019-00129-8

Carter, B. R., Radich, J. A., Doyle, H. L., & Dickson, A. G. (2013). An automated system for spectrophotometric seawater pH measurements. *Limnology and Oceanography: Methods*, *11*(1), 16–27. https://doi.org/10.4319/lom.2013.11.16

Carter, B. R., Sharp, J. D., Dickson, A. G., Álvarez, M., Fong, M. B., García-Ibáñez, M. I., Woosley, R. J., Takeshita, Y., Barbero, L., Byrne, R. H., Cai, W.-J., Chierici, M., Clegg, S. L., Easley, R. A., Fassbender, A. J., Fleger, K. L., Li, X., Martín-Mayor, M., Schockman, K. M., & Wang, Z. A. (2023). Uncertainty sources for measurable ocean carbonate chemistry variables. *Limnology and Oceanography*, *n/a*(n/a). https://doi.org/10.1002/lno.12477

Carter, B. R., Sharp, J. D., García-Ibáñez, M. I., Woosley, R. J., Fong, M. B., Álvarez, M., Barbero, L., Clegg, S. L., Easley, R., Fassbender, A. J., Li, X., Schockman, K. M., & Wang, Z. A. (2024). Random and systematic uncertainty in ship-based seawater carbonate chemistry observations. *Limnology and Oceanography*, *n/a*(n/a). https://doi.org/10.1002/lno.12674

Chavez, F. P., Pennington, J. T., Castro, C. G., Ryan, J. P., Michisaki, R. P., Schlining, B., Walz, P., Buck, K. R., McFadyen, A., & Collins, C. A. (2002). Biological and chemical consequences of the 1997–1998 El Niño in central California waters. *Progress in Oceanography*, *54*(1–4), 205–232. https://doi.org/10.1016/S0079-6611(02)00050-2

Claustre, H., Johnson, K. S., & Takeshita, Y. (2020). Observing the Global Ocean with Biogeochemical-Argo. *Annual Review of Marine Science*, *12*(1), 23–48. https://doi.org/10.1146/annurev-marine-010419-010956

DelValls, T. A., & Dickson, A. G. (1998). The pH of buffers based on 2-amino-2-hydroxymethyl-1,3-propanediol ('tris') in synthetic sea water. *Deep-Sea Research Part I: Oceanographic Research Papers*, *45*(9), 1541–1554. https://doi.org/10.1016/S0967-0637(98)00019-3

Dickson, A. G. (1990). Standard potential of the reaction: AgCl(s) +12H2(g) = Ag(s) + HCl(aq)<math><mtext>AgCl(s) + </mtext><mtext>1</mtext><mtext>2</mtext><mtext>H</mtext><msub><mi></mi><mn>2</mn></msub><mtext>(g) = Ag(s) + HCl(aq)</mtext></math>, and and the standard acidity constant of the ion HSO4− in synthetic sea water from 273.15 to 318.15 K. *The Journal of Chemical Thermodynamics*, *22*(2), 113–127. https://doi.org/10.1016/0021-9614(90)90074-Z

Dickson, A. G., Afghan, J. D., & Anderson, G. C. (2003). Reference materials for oceanic CO2 analysis: A method for the certification of total alkalinity. *Marine Chemistry*, *80*(2), 185–197. https://doi.org/10.1016/S0304-4203(02)00133-0

Dickson, A. G., Sabine, C. L., Christian, J. R., Bargeron, C. P., & North Pacific Marine Science Organization (Eds.). (2007). *Guide to best practices for ocean CO2 measurements*. North Pacific Marine Science Organization.

Doney, S. C., Fabry, V. J., Feely, R. A., & Kleypas, J. A. (2009). Ocean Acidification: The Other CO2 Problem. *Https://Doi.Org/10.1146/Annurev.Marine.010908.163834*, *1*, 169–192. https://doi.org/10.1146/ANNUREV.MARINE.010908.163834

Duarte, C. M., Hendriks, I. E., Moore, T. S., Olsen, Y. S., Steckbauer, A., Ramajo, L., Carstensen, J., Trotter, J. A., & McCulloch, M. (2013). Is Ocean Acidification an Open-Ocean Syndrome? Understanding Anthropogenic Impacts on Seawater pH. *Estuaries and Coasts*, *36*(2), 221–236. https://doi.org/10.1007/s12237-013-9594-3

Evans, W., Lebon, G. T., Harrington, C. D., Takeshita, Y., & Bidlack, A. (2022). Marine CO2 system variability along the northeast Pacific Inside Passage determined from an Alaskan ferry. *Biogeosciences*, *19*(4), 1277–1301. https://doi.org/10.5194/BG-19-1277-2022

Gonski, S. F., Cai, W. J., Ullman, W. J., Joesoef, A., Main, C. R., Pettay, D. T., & Martz, T. R. (2018). Assessment of the suitability of Durafet-based sensors for pH measurement in

dynamic estuarine environments. *Estuarine, Coastal and Shelf Science*, *200*, 152–168. https://doi.org/10.1016/j.ecss.2017.10.020

Goyet, C., & Snover, A. K. (1993). High-accuracy measurements of total dissolved inorganic carbon in the ocean: Comparison of alternate detection methods. *Marine Chemistry*, *44*(2), 235–242. https://doi.org/10.1016/0304-4203(93)90205-3

Hofmann, G. E., Smith, J. E., Johnson, K. S., Send, U., Levin, L. A., Micheli, F., Paytan, A., Price, N. N., Peterson, B., Takeshita, Y., Matson, P. G., Crook, E. D., Kroeker, K. J., Gambi, M. C., Rivest, E. B., Frieder, C. A., Yu, P. C., & Martz, T. R. (2011). High-Frequency Dynamics of Ocean pH: A Multi-Ecosystem Comparison. *PLOS ONE*, *6*(12), e28983. https://doi.org/10.1371/journal.pone.0028983

Ishida, H., Isono, R. S., Kita, J., & Watanabe, Y. W. (2021). Long-term ocean acidification trends in coastal waters around Japan. *Scientific Reports*, *11*(1), 5052. https://doi.org/10.1038/s41598-021-84657-0

Jiang, L.-Q., Pierrot, D., Wanninkhof, R., Feely, R. A., Tilbrook, B., Alin, S., Barbero, L., Byrne, R. H., Carter, B. R., Dickson, A. G., Gattuso, J.-P., Greeley, D., Hoppema, M., Humphreys, M. P., Karstensen, J., Lange, N., Lauvset, S. K., Lewis, E. R., Olsen, A., … Xue, L. (2022). Best Practice Data Standards for Discrete Chemical Oceanographic Observations. *Frontiers in Marine Science*, *8*. https://doi.org/10.3389/fmars.2021.705638

Johnson, K. S., Jannasch, H. W., Coletti, L. J., Elrod, V. A., Martz, T. R., Takeshita, Y., Carlson, R. J., & Connery, J. G. (2016). Deep-Sea DuraFET: A Pressure Tolerant pH Sensor Designed for Global Sensor Networks. *Analytical Chemistry*, *88*(6), 3249–3256. https://doi.org/10.1021/acs.analchem.5b04653

Johnson, K. S., Plant, J. N., & Maurer, T. L. (2018). Processing BGC-Argo pH data at the DAC level. *Argo Data Management*, 1–34.

Lee, K., Kim, T.-W., Byrne, R. H., Millero, F. J., Feely, R. A., & Liu, Y.-M. (2010). The universal ratio of boron to chlorinity for the North Pacific and North Atlantic oceans. *Geochimica et Cosmochimica Acta*, *74*(6), 1801–1811. https://doi.org/10.1016/j.gca.2009.12.027

Lewis, E., Wallace, D., & Allison, L. J. (1998). *Program developed for CO{sub 2} system calculations* (ORNL/CDIAC-105). Brookhaven National Lab., Dept. of Applied Science, Upton, NY (United States); Oak Ridge National Lab., Carbon Dioxide Information Analysis Center, TN (United States). https://doi.org/10.2172/639712

Lilly, L. E., Send, U., Lankhorst, M., Martz, T. R., Feely, R. A., Sutton, A. J., & Ohman, M. D. (2019). Biogeochemical Anomalies at Two Southern California Current System Moorings During the 2014–2016 Warm Anomaly-El Niño Sequence. *Journal of Geophysical Research: Oceans*, *124*(10), 6886–6903. https://doi.org/10.1029/2019JC015255

Lueker, T. J., Dickson, A. G., & Keeling, C. D. (2000). Ocean *p*CO2 calculated from dissolved inorganic carbon, alkalinity, and equations for *K*1 and *K*2: Validation based on laboratory measurements of CO2 in gas and seawater at equilibrium. *Marine Chemistry*, *70*(1), 105–119. https://doi.org/10.1016/S0304-4203(00)00022-0

Ma, D., Gregor, L., & Gruber, N. (2023). Four decades of trends and drivers of global surface ocean acidification. *Global Biogeochemical Cycles*, *n/a*(n/a), e2023GB007765. https://doi.org/10.1029/2023GB007765

Martz, T., Daly, K., Byrne, R., Stillman, J., & Turk, D. (2015). Technology for Ocean Acidification Research: Needs and Availability. *Oceanography*, *25*(2), 40–47. https://doi.org/10.5670/oceanog.2015.30

Martz, T. R., Connery, J. G., & Johnson, K. S. (2010). Testing the Honeywell Durafet® for seawater pH applications. *Limnology and Oceanography: Methods*, *8*(5), 172–184. https://doi.org/10.4319/lom.2010.8.172

Maurer, T. L., Plant, J. N., & Johnson, K. S. (2021). Delayed-Mode Quality Control of Oxygen, Nitrate, and pH Data on SOCCOM Biogeochemical Profiling Floats. *Frontiers in Marine Science*, *8*. https://www.frontiersin.org/articles/10.3389/fmars.2021.683207

McLaughlin, K., Dickson, A., Weisberg, S. B., Coale, K., Elrod, V., Hunter, C., Johnson, K. S., Kram, S., Kudela, R., Martz, T., Negrey, K., Passow, U., Shaughnessy, F., Smith, J. E., Tadesse, D., Washburn, L., & Weis, K. R. (2017). An evaluation of ISFET sensors for coastal pH monitoring applications. *Regional Studies in Marine Science*, *12*, 11–18. https://doi.org/10.1016/j.rsma.2017.02.008

Miller, C. A., Pocock, K., Evans, W., & Kelley, A. L. (2018). An evaluation of the performance of Sea-Bird Scientific's SeaFET™ autonomous pH sensor: Considerations for the broader oceanographic community. *Ocean Science*, *14*(4), 751–768. https://doi.org/10.5194/os-14-751-2018

Müller, J. D., Bastkowski, F., Sander, B., Seitz, S., Turner, D. R., Dickson, A. G., & Rehder, G. (2018). Metrology for pH Measurements in Brackish Waters—Part 1: Extending Electrochemical pHT Measurements of TRIS Buffers to Salinities 5–20. *Frontiers in Marine Science*, *5*. https://www.frontiersin.org/articles/10.3389/fmars.2018.00176

Newton, J. A., Feely, R. A., Jewett, E. B., Williamson, P., & Mathis, J. (2015). *Global Ocean Acidification Observing Network: Requirements and Governance Plan Second Edition GOA-ON Global Ocean Acidification Observing Network*. www.iaea.org/ocean-acidification

Orr, J. C., Epitalon, J.-M., Dickson, A. G., & Gattuso, J.-P. (2018). Routine uncertainty propagation for the marine carbon dioxide system. *Marine Chemistry*, *207*, 84–107. https://doi.org/10.1016/j.marchem.2018.10.006

O'Sullivan, D. W., & Millero, F. J. (1998). Continual measurement of the total inorganic carbon in surface seawater. *Marine Chemistry*, *60*(1), 75–83. https://doi.org/10.1016/S0304-4203(97)00079-0

Paulsen, M.-L., & Dickson, A. G. (2020). Preparation of 2-amino-2-hydroxymethyl-1,3-propanediol (TRIS) pHT buffers in synthetic seawater. *Limnology and Oceanography: Methods*, *18*(9), 504–515. https://doi.org/10.1002/lom3.10383

Perez, F. F., & Fraga, F. (1987). Association constant of fluoride and hydrogen ions in seawater. *Marine Chemistry*, *21*(2), 161–168. https://doi.org/10.1016/0304-4203(87)90036-3

Ribas-Ribas, M., Hernández-Ayón, J. M., Camacho-Ibar, V. F., Cabello-Pasini, A., Mejia-Trejo, A., Durazo, R., Galindo-Bect, S., Souza, A. J., Forja, J. M., & Siqueiros-Valencia, A. (2011). Effects of upwelling, tides and biological processes on the inorganic carbon system of a coastal lagoon in Baja California. *Estuarine, Coastal and Shelf Science*, *95*(4), 367–376. https://doi.org/10.1016/j.ecss.2011.09.017

Rivest, E. B., O'Brien, M., Kapsenberg, L., Gotschalk, C. C., Blanchette, C. A., Hoshijima, U., & Hofmann, G. E. (2016). Beyond the benchtop and the benthos: Dataset management planning and design for time series of ocean carbonate chemistry associated with Durafet®-based pH sensors. *Ecological Informatics*, *36*, 209–220. https://doi.org/10.1016/j.ecoinf.2016.08.005

Rodriguez, C., Huang, F., & Millero, F. J. (2015). The partial molal volume and compressibility of Tris and Tris–HCl in water and 0.725m NaCl as a function of temperature. *Deep Sea Research Part I: Oceanographic Research Papers*, *104*, 41–51. https://doi.org/10.1016/j.dsr.2015.06.008

Sharp, J. D., Pierrot, D., Humphreys, M. P., Epitalon, J.-M., Orr, J. C., Lewis, E. R., & Wallace, D. W. R. (2023). *CO2SYSv3 for MATLAB* (Version v3.2.1) [Computer software]. Zenodo. https://doi.org/10.5281/zenodo.7552554

Skelton, Z. R., McCormick, L. R., Kwan, G. T., Lonthair, J., Neira, C., Clements, S. M., Martz, T. R., Bresnahan, P. J., Send, U., Giddings, S. N., Sevadjian, J. C., Jaeger, S., Feit, A., Frable, B. W., Zerofski, P. J., Torres, M., Crooks, J. A., McCullough, J., Carter, M. L., … Wegner, N. C. (2024). Organismal responses to deteriorating water quality during the historic 2020 red tide off Southern California. *Elementa: Science of the Anthropocene*, *12*(1), 00067. https://doi.org/10.1525/elementa.2023.00067

Sutton, A. J., Battisti, R., Carter, B., Evans, W., Newton, J., Alin, S., Bates, N. R., Cai, W.-J., Currie, K., Feely, R. A., Sabine, C., Tanhua, T., Tilbrook, B., & Wanninkhof, R. (2022). Advancing best practices for assessing trends of ocean acidification time series. *Frontiers in Marine Science*, *9*. https://www.frontiersin.org/articles/10.3389/fmars.2022.1045667

Takeshita, Y., Martz, T. R., Coletti, L. J., Dickson, A. G., Jannasch, H. W., & Johnson, K. S. (2017). The effects of pressure on pH of Tris buffer in synthetic seawater. *Marine Chemistry*, *188*, 1–5. https://doi.org/10.1016/J.MARCHEM.2016.11.002

Takeshita, Y., Martz, T. R., Johnson, K. S., & Dickson, A. G. (2014). Characterization of an Ion Sensitive Field Effect Transistor and Chloride Ion Selective Electrodes for pH Measurements in Seawater. *Analytical Chemistry*, *86*(22), 11189–11195. https://doi.org/10.1021/ac502631z

Takeshita, Y., Warren, J. K., Liu, X., Spaulding, R. S., Byrne, R. H., Carter, B. R., DeGrandpre, M. D., Murata, A., & Watanabe, S. (2021). Consistency and stability of purified meta-cresol purple for spectrophotometric pH measurements in seawater. *Marine Chemistry*, *236*, 104018. https://doi.org/10.1016/J.MARCHEM.2021.104018

Tanhua, T., McCurdy, A., Fischer, A., Appeltans, W., Bax, N., Currie, K., DeYoung, B., Dunn, D., Heslop, E., Glover, L. K., Gunn, J., Hill, K., Ishii, M., Legler, D., Lindstrom, E., Miloslavich, P., Moltmann, T., Nolan, G., Palacz, A., … Wilkin, J. (2019). What We Have Learned From the Framework for Ocean Observing: Evolution of the Global Ocean

Observing System. *Frontiers in Marine Science*, *6*. https://doi.org/10.3389/fmars.2019.00471

Velo, A., & Padin, X. A. (2022). Advancing real-time pH sensing capabilities to monitor coastal acidification as measured in a productive and dynamic estuary (Ría de Arousa, NW Spain). *Frontiers in Marine Science*, *9*. https://doi.org/10.3389/fmars.2022.941359

Wang, Z. A., Moustahfid, H., Mueller, A. V., Michel, A. P. M., Mowlem, M., Glazer, B. T., Mooney, T. A., Michaels, W., McQuillan, J. S., Robidart, J. C., Churchill, J., Sourisseau, M., Daniel, A., Schaap, A., Monk, S., Friedman, K., & Brehmer, P. (2019). Advancing Observation of Ocean Biogeochemistry, Biology, and Ecosystems With Cost-Effective in situ Sensing Technologies. *Frontiers in Marine Science*, *6*. https://doi.org/10.3389/fmars.2019.00519

Wanninkhof, R., Sabine, C., & Aricò, S. (2021). *Integrated ocean carbon research: A summary of ocean carbon research, and vision of coordinated ocean carbon research and observations for the next decade.* https://aquadocs.org/handle/1834/42258

Wimart-Rousseau, C., Steinhoff, T., Klein, B., Bittig, H., & Körtzinger, A. (2024). Technical note: Assessment of float pH data quality control methods – a case study in the subpolar northwest Atlantic Ocean. *Biogeosciences*, *21*(5), 1191–1211. https://doi.org/10.5194/bg-21-1191-2024

Wolfe, W. H., Martz, T. R., Dickson, A. G., Goericke, R., & Ohman, M. D. (2023). A 37-year record of ocean acidification in the Southern California current. *Communications Earth & Environment*, *4*(1), Article 1. https://doi.org/10.1038/s43247-023-01065-0

Wolfe, W., Shipley, K., Bresnahan, P., Takeshita, Y., Wirth, T., & Martz, T. (2021). Technical Note: Stability of tris pH buffer in artificial seawater stored in bags. *Ocean Science Discussions*, 1–15. https://doi.org/10.5194/os-2020-120

Chapter 2 Assessment of a pH optode for oceanographic moored and profiling applications

LIMNOLOGY
and
OCEANOGRAPHY: METHODS

ASLO

Limnol. Oceanogr.: Methods 2024

doi: 10.1002/lom3.10646

Assessment of a pH optode for oceanographic moored and profiling applications

Taylor Wirth,[1]* **Yuichiro Takeshita**,[2] **Benjamin Davis**,[2] **Ellen Park**,[3] **Irene Hu**,[2] **Christine L. Huffard**,[2] **Kenneth S. Johnson**,[2] **David Nicholson**,[3] **Christoph Staudinger**,[4] **Joseph K. Warren**,[2] **Todd Martz**[1]

[1]Scripps Institution of Oceanography, University of California San Diego, La Jolla, California, USA
[2]Monterey Bay Aquarium Research Institute, Moss Landing, California, USA
[3]Woods Hole Oceanographic Institution, Woods Hole, Massachusetts, USA
[4]PyroScience GmbH, Aachen, Germany

Abstract

As global ocean monitoring programs and marine carbon dioxide removal methods expand, so does the need for scalable biogeochemical sensors. Currently, pH sensors are widely used to measure the ocean carbonate system on a variety of autonomous platforms. This paper assesses a commercially available optical pH sensor (optode) distributed by PyroScience GmbH for oceanographic applications. Results from this study show that the small, solid-state pH optode demonstrates a precision of 0.001 pH and relative accuracy of 0.01 pH using an improved calibration routine outlined in the manuscript. A consistent pressure coefficient of 0.029 pH/1000 dbar is observed across multiple pH optodes tested in this study. The response time is investigated for standard and fast-response versions over a range of temperatures and flow rates. Field deployments include direct comparison to ISFET-based pH sensor packages for both moored and profiling platforms where the pH optodes experience sensor-specific drift rates up to 0.006 pH d^{-1}. In its current state, the pH optode potentially offers a viable and scalable option for short-term field deployments and laboratory mesocosm studies, but not for long term deployments with no possibility for recalibration like on profiling floats.

The existing suite of commercially available oceanographic sensors for measuring the inorganic carbonate system is limited (Martz et al. 2015; Bushinsky et al. 2019). Commercially available pH sensors have grown in number and diversity of methodology, with current options based on electrochemical, spectrophotometric, potentiometric, and optical technology (IOCCP 2024). Glass pH electrodes have been used for decades to measure seawater pH on the benchtop. In situ glass pH electrode sensors (e.g., Idronaut, Sea-Bird Scientific SBE27, YSI EXO) are small and easily integrated into sensor packages and platforms, but suffer from reduced accuracy of ≥ 0.1 pH (Johengen et al. 2015) and sensor drift requiring frequent calibration (Martz et al. 2010; Rérolle et al. 2012).

In contrast, spectrophotometric-based instruments (e.g., Sunburst Sensors SAMI-pH, Clearwater Sensors lab on chip) have proven to be accurate to ~ 0.005 pH for long durations with low drift rates (Mowlem et al. 2021). However, their large size and long measurement intervals due to the microfluidics complexities (valves, pumps) pose challenges for fast profiling and platform integration (Yin et al. 2021).

Potentiometric pH sensors based on the Honeywell Ion Sensitive Field Effect Transistor (ISFET; Martz et al. 2010) have been successfully deployed on a wide variety of autonomous platforms and vehicles such as profiling floats (Johnson et al. 2016), underwater gliders (Saba et al. 2019; Takeshita et al. 2021*a*), moorings (Lilly et al. 2019), and autonomous surface vehicles (Chavez et al. 2018). They have been used to quantify natural variability across a wide range of marine ecosystems (Hofmann et al. 2011), estimate carbon dioxide (CO_2) fluxes (Gray et al. 2018), investigate the potential for seagrass meadows to locally ameliorate impacts of ocean acidification (Ricart et al. 2021), examine feedbacks between physical and biological forcings on seawater chemistry (Cyronak et al. 2020), quantify benthic net community production and calcification rates on coral reefs (Takeshita et al. 2018), and used as feedback control in ocean acidification mesocosm studies (Hughes et al. 2018; Donham et al. 2023). In summary, the ISFET has become a cornerstone of global ocean carbon

*Correspondence: twirth@ucsd.edu

Additional Supporting Information may be found in the online version of this article.

observing, through many observational networks worldwide such as the Integrated Ocean Observing System (IOOS, US IOOS 2021), Global Ocean Acidification Observing Network (GOA-ON, Rivest et al. 2016), and Biogeochemical Argo (Johnson et al. 2017; Claustre et al. 2020; Maurer et al. 2021).

Despite the wide breadth and usage, Honeywell, the sole producer of ISFETs widely used in DuraFET and Deep-Sea-DuraFET pH sensors, announced a halt in production in June 2022, leaving a void in the availability of scalable pH sensors for oceanographic applications. Production has since been restarted, but the potential cease in ISFET availability would have significantly hindered the ability to effectively observe the ocean carbon cycle.

Motivated to address this sole-source vulnerability in global ocean carbon observing, this study aims to contribute to the ongoing discourse on pH instrumentation by assessing a commercially available optical pH sensor, the Pico-pH-SUB pH optode, distributed by PyroScience GmbH. This optical technology, similar in design to the very popular oxygen optodes currently deployed on profiling floats and various platforms, holds promise as oxygen optode sensors have proven to be extremely robust (Tengberg et al. 2006; Bittig et al. 2018) and are indeed the most widely deployed type of chemical sensor in the ocean.

The performance of the pH optodes has been characterized in the laboratory, briefly in the field and shows promise (Fritzsche et al. 2018; Staudinger et al. 2018; Staudinger et al. 2019; Monk et al. 2021). However, further characterization focused specifically on oceanographic applications is necessary preceding widescale use of this sensor in the ocean. The objectives of this study include assessing the performance of the factory-recommended calibration procedure, developing an improved calibration method, verifying temperature response on the various calibration coefficients, quantifying response time and pressure coefficients, and assessing sensor performance and stability in different ocean environments.

This study involves deploying the pH optode on fixed platforms in the deep ocean and a highly dynamic coastal environment. Sensor drift and a proposed correction method are rigorously evaluated in these two diverse settings. In addition, the pH optode is deployed on a Spray underwater glider to assess its performance for profiling applications. Through these comprehensive analyses, a thorough assessment of the Pico-pH-SUB in multiple ocean environments is provided. The assessment generated from this study is intended to offer insights and recommendations to the broader oceanographic community. The findings contribute to advancing the understanding of pH measurement technologies, ensuring continued progress in monitoring and managing the health of marine ecosystems.

Materials and procedures

Sensor description and operating principles

We used the Pico-pH-SUB model manufactured by PyroScience GmbH (Aachen, Germany) for this study. This OEM sensor (~ 2k USD) is pressure rated to 4000 dbar and has a low power draw of 50 mW during operation (< 500 μW during sleep). Operating at a maximum sampling rate of 20 Hz, it communicates via UART protocol. The pH optode can be fully powered off in between measurements without compromising performance. For an accurate calculation of pH from the Pico-pH-SUB, a concurrent temperature measurement is required. A PT100 resistance temperature detector can be soldered directly to the Pico-pH-SUB as recommended from PyroScience GmbH, or the temperature correction can be applied post processing using an external temperature sensor, as done in this study. The performance of the Pico-pH-SUB should be identical to the other pH optodes in the PyroScience GmbH product line, such as the AquapHOx, and when integrated into a custom logger (5k–11k USD).

The pH sensitive material or "foil" is contained in the "sensor tip" which is secured by the "sensor cap" (Fig. 1a). The sensor cap also acts as a guard to protect the sensor tip. The sensor tip and cap are sold as a single assembly, separate from the optoelectronics, and installed by the user. In this study, we used both the commercially available sensor cap, and designed our own custom sensor cap to secure the sensor tip to the Pico-pH-SUB.

The pH optode's operational principle is based on the Dual Lifetime Referencing scheme (Klimant et al. 2001). The foil is comprised of an immobilized fluorescent indicator (an aza-BODIPY dye synthesized by PyroScience GmbH) and phosphorescent reference (Egyptian blue) on a support material (a PET thermoplastic). An additional outermost protective layer is equipped for optical isolation to minimize effects from direct sunlight such as oversaturation of the photodiode and bleaching of the indicator (Clarke et al. 2015; Staudinger et al. 2019). The optoelectronics utilize a 625 nm LED for excitation and a photodetector in combination with a long-pass emission filter are used to measure the luminescence intensity ratio between the pH sensitive indicator and the reference dye. The pH optode sensor signal (R) is the ratio between the indicator fluorescence intensity and reference phosphorescence intensity (Staudinger et al. 2019). This analog signal is compensated for device effects such as sensor internal temperature and signal intensity. The response of the pH optode can be described by a Boltzmann sigmoid in relation to pH (Fig. 1b and Eq. 1):

$$\mathrm{pH} = pKa' + \mathrm{slope}' \times \log\left(\frac{R1' - R2'}{R - R2'} - 1\right) + \mathrm{cal\_offset} \quad (1)$$

where $R1'$ and $R2'$ are the top and bottom asymptote terms, respectively, pKa' represents the point of inflection, $slope'$ is the slope at the point of inflection. The *cal_offset* term refers to an empirical pH offset determined during calibration and/or deployment. The prime symbol indicates the terms are at in situ temperature, and all terms expand to include the coefficient at a reference temperature of 20°C (e.g., $R1$), and a

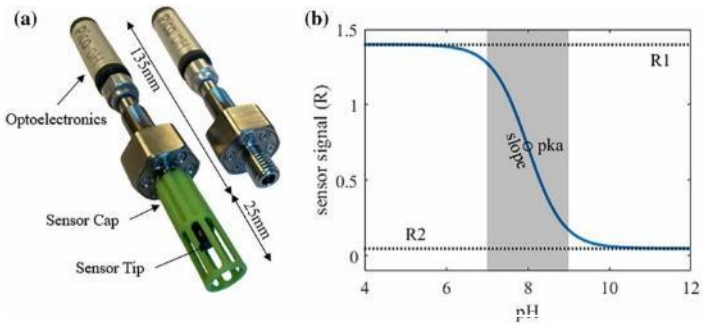

Fig. 1. (**a**) The Pico-pH-SUB sensor with and without PHCAP-PK8T-SUB sensor cap and tip installed. (**b**) Boltzmann sigmoid sensor signal R vs. pH. Nominal values of 1.4 for *R1*, 0.05 for *R2*, 8.0 for *pKa*, and 1.0 for *slope* were used. The shaded region indicates the functional pH measurement range of 7–9.

linear temperature coefficient (e.g., $R1_T$) (Eqs. 2–5). Additional salinity coefficients, pKa_{is1} and pKa_{is2}, are applied to *pKa* only:

$$R1' = R1 \times (1 + R1_T \times (T_c - 20)) \quad (2)$$

$$R2' = R2 \times (1 + R2_T \times (T_c - 20)) \quad (3)$$

$$slope' = slope \times (1 + slope_T \times (T_c - 20)) \quad (4)$$

$$pKa' = pKa + pKa_T \times (T_C - 20) - 0.5 \times pKa_{is1} \times \left[\frac{\sqrt{\frac{20 \times S}{1000}}}{1 + \sqrt{\frac{20 \times S}{1000}}} - 0.2791745 - pKa_{is2} \times \left(\frac{20 \times S}{1000} - 0.15 \right) \right] \quad (5)$$

where T_C is the temperature in °C, S is practical salinity.

The PHCAP-PK8T-SUB sensor cap from PyroScience GmbH, designed to measure seawater pH on the total scale, was employed for all tests. The pH indicator material has a *pKa* of around 8, which aligns closely with the nominal ocean pH value. The sensor responds to changes in pH between 7 and 9, allowing coverage of the full range of ocean pH except in rare extreme environments. In addition, a fast-response version of this sensor tip was tested, which was custom developed for this project. The fast-response sensor tip is identical in makeup using the same pH sensitive material, but with the outermost optical protective layer removed to reduce the distance of diffusion between sample and the immobilized indicator in the foil. All laboratory tests and field deployments performed in this study were either indoors, with opaque flow manifolds or in the deep sea eliminating any negative effects due to direct sunlight.

Laboratory calibration and characterization

In the laboratory, the accuracy and assumptions associated with the manufacturer recommended calibration protocol were assessed (Three-point and temperature cycle calibration); an improved (but more time and labor intensive) calibration protocol was developed (Seawater multipoint calibration), and the pressure response (Pressure response) and the response time were quantified (Response time). Three Pico-pH-SUB units were used for sections Three-point and temperature cycle calibration and Seawater multipoint calibration. The same batch of sensor cap, thus the same batch of sensor tip and sensing material, was installed on each Pico-pH-SUB. Each sensor cap, with installed sensor tip, comes with predetermined factory coefficients from PyroScience GmbH, which are applied to the entire production batch. Three different Pico-pH-SUB units were used for section Pressure response, and two different Pico-pH-SUB units were used for section Response time. Sensor caps from the same batch were used in each section, except Pressure response, with different batches used across sections.

Three-point and temperature cycle calibration

PyroScience GmbH advises the user to conduct a 1- or 2-point calibration before initiating measurements. The first calibration point quantifies *R1* by immersing the Pico-pH-SUB in an acidic solution of pH < 4, and the second quantifies *R2* in a basic solution of pH > 10. An optional third point quantifies *cal_offset* using a solution with known pH. The determination of these three coefficients allows for the definition and adjustment of the sigmoid response curve, assuming the *pKa* and *slope* remain unchanged from the factory values. Among these coefficients, *R1* and *R2* have a nonlinear impact and can have an outsized effect on the calculated pH values (Fig. 2), underscoring the critical importance of their characterization.

For the first two calibration points, an acidic solution of pH ~ 2 was prepared using 0.08 mol L^{-1} citric acid, and a basic solution of pH ~ 11 was prepared using 0.1 mol L^{-1} sodium carbonate. Both solutions were prepared with and without a 0.7 mol L^{-1} sodium chloride (NaCl) background to compare

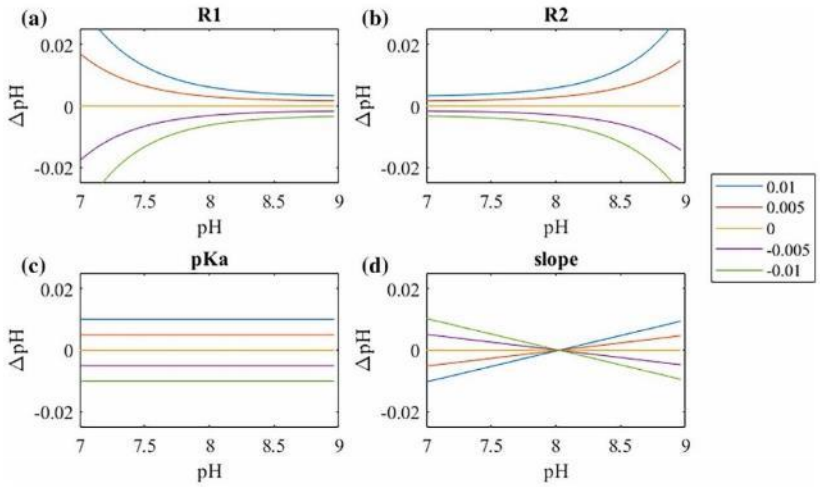

Fig. 2. The difference in calculated pH from the Pico-pH-SUB if the following sigmoid coefficient is varied by ± 0.01: (**a**) *R*1, (**b**) *R*2, (**c**) *pKa*, (**d**) *slope*. Nominal values for *R*1 = 1.5, *R*2 = 0.05, *pKa* = 8.0, *slope* = 1.0 were used.

results if a natural seawater ionic was used. PyroScience GmbH provides these solutions in small volumes to be prepared in deionized water, which posed challenges for temperature regulation and multi-day tests. Therefore, larger volume solutions were prepared for this study with separately sourced chemicals. To ensure stable readings in each solution, the Pico-pH-SUB was immersed in seawater for at least 24 h preceding the three-point calibration. Hydration of the sensing material reduced conditioning observed when a dry sensor was immersed in the acidic solution. During calibration, each solution was continuously stirred, and temperature was measured in all three solutions with a QTI DirecTemp USB thermometer (DTU6028-002), which is accurate to 0.1°C (with resolution of 0.01°C). The sensor signal, *R*, was recorded for 1 h at 1 Hz in the acidic and basic calibration solutions. *R*1 and *R*2 were calculated as the average of the final 15 readings in each solution.

The *cal_offset* was then determined by immersing the sensor in seawater with salinity of 33.5 and at 20°C, while solution pH was measured spectrophotometrically using an automated system with *meta*-cresol purple (mCP) indicator dye (Clayton and Byrne 1993; Carter et al. 2013). The biases from impurities in the mCP dye were corrected through direct comparisons with purified mCP obtained from the laboratory of R. Byrne, as described in Takeshita et al. (2021*b*). The *cal_offset* was defined as the difference between spectrophotometric pH and pH calculated from the Pico-pH-SUB, and then applied for all subsequent measurements following the calibration process.

To verify manufacturer-provided temperature coefficients ($R1_T$ and $R2_T$), the Pico-pH-SUB was operated in the acidic and basic solutions, respectively, between 5°C and 25°C, spaced at 5° intervals. Each discrete temperature step was held for a duration exceeding 2 h to allow the system and sensors to stabilize. Subsequently, the final 8 data points (spanning 2 min) for each temperature step were averaged, and a least squares linear regression was fitted. The slope of the linear regression represents the temperature coefficient.

Seawater multipoint calibration

The manufacturer recommended three-point calibration method described above assumes that the *pKa* and *slope* remain unchanged from the factory characterization. Furthermore, the *R*1 and *R*2 characterization occurs in non-seawater media, thus, matrix effects could add uncertainty to this calibration. To address these issues, we developed an automated calibration method using natural seawater that is directly traceable to spectrophotometric pH measurements, which from here on will be referred to as the "Seawater multipoint calibration." Multiple discrete spectrophotometric pH measurements were made within the functional range of the sensor (pH 7–9), and the four coefficients *R*1, *R*2, *pKa*, and *slope* were simultaneously fitted to Eqs. 1–5. This approach was conducted at a single temperature (typically 20°C) and assumed that the temperature coefficients previously determined for each sensor remain unchanged. When performed at 20°C, all the temperature dependencies in Eqs. 2–5 are minimized or zero, so no errors would propagate due to temperature coefficient uncertainty. Manufacturer values for pKa_T, $slope_T$, pKa_{is1}, and pKa_{is2} were used.

A minimum of four discrete pH points within the functional range are required to properly constrain the

multivariate optimization solver of the four sigmoid coefficients. Seawater pH was cycled between 7.4 and 8.2, at increments of 0.1 pH, resulting in nine points. This pH range was chosen to encompass the expected pH range for the field deployments in this study. Each pH increment was held for a minimum of 2 h. At the end of each pH increment, an automated spectrophotometric pH measurement was made. The seawater multipoint routine was performed three times for the three Pico-pH-SUB units to assess reproducibility and accuracy.

To conduct the seawater multipoint calibration, a customized high-precision pH and temperature control system was developed, hereafter referred to as the "pHstat system." The pHstat system utilized a 4-liter jacketed beaker connected to a recirculating temperature-controlled bath (Fisher Scientific Isotemp 4100) for maintaining temperature at specified levels. A custom cap, sealed with an O-ring, housed the sensors and tubing. The pH of the solution was controlled through a PID feedback loop that adjusted the proportion of CO_2-free gas (either pure nitrogen (N_2) or compressed air with an Ascarite II scrubber) and a 5% CO_2-air mixture that was bubbled into solution. The two gasses were mixed before delivery into the beaker, and the proportion was controlled by adjusting the flow rates of the two gasses using mass flow controllers with a range of 0–1 SLPM for the CO_2-free gas and 0–14 SCCM for the CO_2 blend (Sierra Instruments SmartTrak 50). A Honeywell DuraFET III pH sensor (51453503-501) was used as the feedback sensor for the PID control and was regularly calibrated to spectrophotometric samples. The DuraFET was chosen as it has a short-term precision of 0.0005 (Martz et al. 2010) and has a Nernstian response over a large pH range (Takeshita et al. 2014). The same spectrophotometric pH system described in section Three-point and temperature cycle calibration was integrated into the pHstat system, operating asynchronously to automatically draw samples from the jacketed beaker. The pHstat system demonstrated remarkable pH and temperature control precision, with a standard deviation of < 0.001 pH across a pH range of 7–8.5 and 0.01°C of temperature across a range of 5–30°C.

Pressure response

To determine the unknown pressure response of the Pico-pH-SUB, the sensor response was measured over a range of temperatures and pressures in a solution of known pH. For this, an equimolar tris buffer prepared in artificial seawater was utilized, as this is a standard solution for pH measurements in seawater, and its pH can be calculated over a range of temperatures and pressures (DelValls and Dickson 1998; Rodriguez et al. 2015; Takeshita et al. 2017; Müller et al. 2018). A custom pressure and temperature control (PTC) system at the Monterey Bay Aquarium Research Institute was used for this experiment. This system has been used for establishing the pressure coefficients of hundreds of Deep-Sea-DuraFET pH sensors (Johnson et al. 2016; Johnson et al. 2017).

The temperature was cycled between 5°C and 25°C at 5°C intervals. At each temperature step, pressure was cycled from 0 to 2000 dbar over an 8-h period. Temperature, pressure, and outputs from the Pico-pH-SUB were recorded at 30-s intervals. The calculated pH of tris buffer was compared against the pH output from the Pico-pH-SUB units at each temperature and pressure combination to determine the pressure response. The pressure response was characterized for three Pico-pH-SUB units, each equipped with different sensor caps for comparison across sensor material batches. Furthermore, one Pico-pH-SUB unit underwent a duplicate test to assess repeatability.

Response time

The response time for the Pico-pH-SUB was assessed for the standard-response sensor tip and a fast-response sensor tip, using two different protocols. The response time for the standard-response tip was rigorously tested in a flume with known flow velocities, whereas the response time for the fast-response tip was tested in a stirred beaker because it was not available when the flume experiments were being conducted. The results for the fast-response tip, while less quantitative regarding test controls (flow rate and temperatures), serve to demonstrate the substantial improvement in response time.

The response time of two Pico-pH-SUB units equipped with the standard-response tip was assessed within the seawater Aquatron Flume tank at Dalhousie University. Tests were performed at low and high temperatures (~ 7°C and 17°C) over a range of flow velocities from 5 to 25 cm s^{-1}, at ~ 5 cm s^{-1} increments, for both rising and falling pH step changes. The Pico-pH-SUB was first immersed in a separate temperature-controlled bath for 20 min, set to match the flume temperature. The pH of the bath was adjusted from 8.0, which was the approximate flume pH, by ~ 0.5 pH units upward or downward using sodium hydroxide or hydrochloric acid, respectively. After the 20-min conditioning period, a custom sensor cover was affixed over the Pico-pH-SUB sensor cap to trap the high or low pH solution, and the sensors were transferred to the flume. Once steady flow resumed in the flume, the sensor covers were quickly removed to produce a step change of pH. The Pico-pH-SUB measurements were recorded at 1 Hz for 20 min. Throughout all tests, the orientation of the Pico-pH-SUB remained uniform, with the sensor tip (foil surface) positioned perpendicular to the flow. This approach ensured a systematic evaluation of response times under varied conditions within the flume environment.

The response time of two Pico-pH-SUB units equipped with fast-response tips were measured by switching between two stirred seawater solutions at pH ~ 7.1 and pH ~ 8.5. Stirring speed was constant for all tests. Seawater pH was adjusted by bubbling N_2 and CO_2 gas. The temperature of both solutions was controlled at 6°C, using a 250 mL jacketed beaker. Sensors were switched between the solutions three times to assess repeatability.

Response time is reported as the time constant (63.2% or e-folding time), τ, of the exponential step response. The Pico-pH-SUB units with the standard-response sensor tips had a previous firmware version which did not utilize the *R* output but the phase shift value *dPhi* (Staudinger et al. 2018). The sensor signal (*R*) or cot(*dPhi*) measured by the Pico-pH-SUB was fit to quantify the response time. The response was initially fitted to the model:

$$y = A \times \left(1 - e^{-\frac{x}{\tau}}\right) + b \tag{6}$$

where A is the amplitude of the pH step change, x is the elapsed time starting from when the sensor cover was removed or beaker was switched, and b is the offset. A and b were then used to normalize the data, and the slope of the linearized Eq. 6 (outlined in Bittig et al. 2014) was used to determine the response time τ:

$$y_{\text{norm}} = 1 - e^{-\frac{x}{\tau}} \tag{7}$$

Field deployments

The in situ performance of the pH optode was assessed through three field deployments: a nearly yearlong deployment at 4000 m depth off the coast of California, a 2.5-month deployment in a shallow, dynamic coastal environment in Southern California, and on a Spray underwater glider that profiled to 1000 m off the Central California Coast.

Station M

Two AquapHOx-LX were deployed at 4000 m depth on a benthic lander at Station M (34.5°N, 123°W; Smith et al. 1983) off the coast of California for approximately 1 yr (09 October 2021–29 September 2022). One unit was secured just above the seafloor or benthic boundary layer (labeled as "BBL"), and the other 1 m above the seafloor (labeled as "1m"; Fig. 3a). The AquapHOx-LX is a data logger distributed by PyroScience GmbH that houses the Pico-pH-SUB using the standard-response sensor tip and an integrated thermistor. Measurement interval was set to 10 min. The Pico-pH-SUB units were calibrated using the three-point method before deployment. These Pico-pH-SUB units also had a previous firmware version which reported *dPhi* instead of *R*, but performance is comparable between versions as hardware characteristics of the sensor did not change between versions. Even though these units do not provide a direct comparison with the current firmware versions used throughout this study, the year-long deployment provides insights into long-term drift in a deep, cold, and stable environment. The measured pH was compared against pH estimated using an empirical algorithm (ESPER-LIR, Carter et al. 2021). ESPER-LIR inputs included temperature measured by the AquapHOx-LX, estimated oxygen of 133 μmol/kg and salinity (PSS-78) of 34.68 (Smith et al. 2022), and estimated nitrate of 37 μmol kg^{-1} derived from GLODAP V2.2022 (Lauvset et al. 2022), location and date. The uncertainty of the ESPER-LIR input oxygen is 1%, consistent with the historic variability at Station M from weekly oxygen measurements between 2015 and 2020 using a benthic rover (Supporting Information Fig. S1a; Smith et al. 2021). The remaining ESPER input uncertainties were set to 0.003 for temperature and salinity and 2% for nitrate.

Scripps pier

The Pico-pH-SUB was deployed alongside a Self-Calibrating SeapHOx (SCS) at Scripps Pier in La Jolla, CA for ~ 2.5 months (18 July–05 October 2023). The SCS is a sensor package containing a DuraFET pH sensor and is capable of autonomous in situ calibration with tris buffer prepared in artificial seawater (Bresnahan et al. 2021). Deployment depth was approximately 4 m, fixed to a pier piling. The nearshore environment experiences seasonal wind-driven upwelling, where pH and temperature can be as low as ~ 7.7 and 10.5°C, respectively, even at shallow depths (Kekuewa et al. 2022). The Pico-pH-SUB was integrated into its own housing with a custom controller to poll and record the measurements at 10-min intervals. A custom sensor cap was developed to house the standard-response sensor tip, which included an O-ring seal and separate flow manifold (Fig. 3b). The outflow of the SCS was directly plumbed to the flow manifold of the Pico-pH-SUB, which ensured a pumped flow stream to the sensor tip and allowed for a direct comparison of the measurements. In addition, two automated tris buffer injections of the SCS flowed through the Pico-pH-SUB manifold to provide high quality validation samples.

Prior to deployment, the Pico-pH-SUB was calibrated using (1) the three-point calibration with factory temperature coefficients, (2) the three-point calibration with sensor-specific re-determined temperature coefficients, and (3) the multipoint calibration with re-determined temperature coefficients. Calibration methods 1 and 2 were highly similar, resulting in exclusion of method 2 from the discussion below. The pH reported by the SCS was calibrated to the automated tris buffer injections performed during the deployment, following the methodology outlined in Bresnahan et al. (2021). Two discrete bottle samples were collected, poisoned, and analyzed on a spectrophotometric system using purified mCP.

Using the two automated tris buffer injections, an in situ adjustment to *cal_offset* and drift correction method is explored. To determine the optimal number of validation samples required, an analysis involving the hypothetical collection of 2–10 validation samples uniformly spaced between the deployment's start and end dates was conducted.

Spray glider

The Pico-pH-SUB was integrated onto a Spray underwater glider (Sherman et al. 2001) to evaluate the sensor performance on profiling platforms. The Spray glider was also equipped with a Deep-Sea-DuraFET (DSD) pH sensor (Johnson et al. 2016; Takeshita et al. 2021*a*), allowing for a direct comparison between the two pH sensors. A custom housing with a

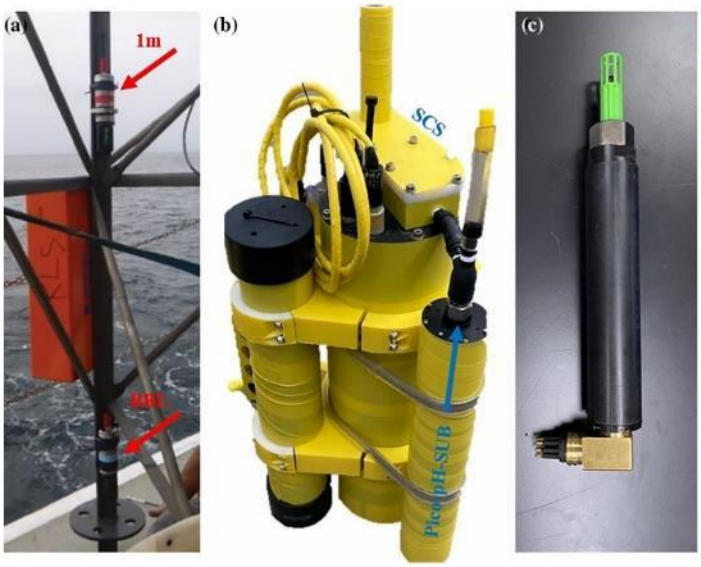

Fig. 3. (**a**) Two Pico-pH-SUB loggers (AquapHOx-LX, red arrows) mounted on a benthic lander. (**b**) The Self-Calibrating SeapHOx (SCS) pictured with the Pico-pH-SUB (blue arrow) housing. (**c**) The Pico-pH-SUB housing with SubConn connector used to integrate into the Spray glider. Flow manifold not shown.

flow manifold designed to fit around the factory sensor cap was fabricated for the Pico-pH-SUB and integrated into the pumped flow stream of the Spray glider (Fig. 3c). The Pico-pH-SUB was powered and polled by the main glider controller and measured on both the ascent and descent for some profiles to assess performance between the two, which would indicate errors due to slow sensor response. The Pico-pH-SUB underwent the pre-deployment temperature cycle and seawater multipoint calibration procedures.

Two missions were conducted to ~ 25 km offshore in Monterey Bay, CA, with maximum dives to 1000 m. The first mission (15 February–02 March 2023) utilized the standard-response sensor tip, whereas the second mission (10–17 July 2023) utilized the fast-response sensor tip. For both missions, dives were conducted to 500 m, then dive depths were sequentially increased to 1000 m at 100-m intervals, while making measurements on both the ascent and descent. Unfortunately, the cabling to the DSD failed during the first mission, thus, the Pico-pH-SUB with the standard foil was compared to pH estimated from CANYON-B (Bittig et al. 2018), as this algorithm estimates pH accurately near Monterey Bay, particularly at depths below 300 m (Takeshita et al. 2021*a*). The Pico-pH-SUB with the fast-response sensor tip was directly compared to the DSD for the second mission. For each mission, the difference between algorithm pH and pH measured by the Pico-pH-SUB for the first dive below 900 dbar determined the *cal_offset* applied to every profile. The pressure coefficient determined in this study was also applied to every profile. The DSD data were adjusted following Takeshita et al. (2021*a*).

Assessment

Three-point and temperature cycle calibration

The addition of 0.7 mol L^{-1} NaCl in the acidic solution produced an increase in $R1$ of 0.0433 ± 0.0008 for the three Pico-pH-SUB units. This offset in $R1$ changes calculated pH depending on the solution pH. For example, pH can shift by ~ 0.03 at pH 8, and ~ 0.05 at pH 7.6 due to a 0.05 shift in $R1$. As $R1$ is the acidic asymptote, there is a larger effect at lower pH values (Fig. 2). This was a surprising, yet repeatable effect that was not reported in previous studies (Staudinger et al. 2018) and highlights the importance of characterizing $R1$ in a solution with similar ionic strength as the target environment. On the other hand, there was no shift in $R2$ observed with the NaCl addition, indicating that it can be characterized without the addition of NaCl, which simplifies solution preparation.

Values for the $R1$, $R2$, and *cal_offset* coefficients obtained using the three calibration methods for the three Pico-pH-SUB units are shown in Table 1. Large variability in $R1$ was observed between the three units and had a range of ~ 0.08

Table 1. Coefficients for three Pico-pH-SUB units, determined by varying calibration methods. *R1* and *R2* for the temperature cycle method were determined by interpolating a linear regression to 20°C.

		Three-point			Temperature cycle			Seawater multipoint		
	Pyro Sci	Pico 1	Pico 2	Pico 3	Pico 1	Pico 2	Pico 3	Pico 1	Pico 2	Pico 3
R1	1.6181	1.5920	1.5633	1.5115	1.4201	1.4004	1.3551	1.4900	1.4692	1.4141
R2	0.0579	0.0399	0.0309	0.0285	0.0278	0.0120	0.0168	0.0039	0.0040	0.0045
pKa	8.0840	-	-	-	-	-	-	8.1174	8.1109	8.1101
slope	1.0340	-	-	-	-	-	-	1.0226	1.0150	1.0126
$R1_T$	−0.0008	-	-	-	−0.0031	−0.0031	−0.0030	-	-	-
$R2_T$	−0.0011	-	-	-	0.0016	0.0016	0.0016	-	-	-
cal_offset	-	0.0509	0.0475	0.0434	-	-	-	-	-	-
Date	-	11 Oct 2023			31 Oct 2023			08 Dec 2023		

during each calibration. The relative magnitude of *R1* between the sensors were consistent across each calibration (e.g., Pico 1 had the highest *R1* during each calibration), indicating that the differences in observed *R1* reflect real differences in the calibration coefficient. Furthermore, all *R1* values obtained in this study were significantly lower than the manufacturer assigned value. These results suggest that each sensor tip should be calibrated individually for *R1* to obtain the most accurate results. On the other hand, the variability between sensors for the other three coefficients were smaller, with a range of ~ 0.01 for *R2*, 0.007 for *pKa*, and 0.01 for *slope*. This indicates that batch calibration may be sufficient for these coefficients. While these values were slightly different from the manufacturer assigned values, the resulting biases are < 0.01 pH (Fig. 2), unless measuring solution pH of > 8.5, where biases may increase to > 0.01. Therefore, it may be sufficient to utilize the manufacturer provided values for *R2*, *pKa*, and *slope* for most applications where accuracy of pH better than 0.01 are not required, requiring only a single point calibration in acidic solution. However, to achieve the highest accuracy possible, it is recommended to individually calibrate each Pico-pH-SUB with its respective sensor tip for all three coefficients.

Accurate temperature coefficients must be established if the Pico-pH-SUB is to be used over a wide range of temperatures. There was excellent agreement in the $R1_T$ and $R2_T$ between each Pico-pH-SUB unit (Table 1; Supporting Information Fig. S2), suggesting that the temperature coefficients are consistent across the same sensor tip batch. However, there was a small difference of ~ 0.0025 between the temperature coefficients provided by the manufacturer and those determined by this study ($R1_T$ was lower, and $R2_T$ was higher relative to the manufacturer values). A difference of this magnitude for $R1_T$ results in a maximum difference of calculated pH of 0.03 at 5°C or 35°C (vs. 20°C), while at pH 8 (Supporting Information Fig. S3). The larger the deviation from 20°C, the greater the difference in calculated pH.

The $R2_T$ coefficient determined by the temperature cycle method was opposite in sign than compared to the factory-determined value (Table 1). The change in $R2_T$ does not affect calculated pH as significantly as $R1_T$ for most oceanographic applications, since its impact is larger as solution pH increases above ~ 8.1 (*pKa*). A difference of 0.0025 for $R2_T$ equates to a maximum pH difference of only ~ 0.002 at 5°C or 35°C (Supporting Information Fig. S3). A lower pH yields a lower pH difference for this change in $R2_T$, ~ 0.001 at pH 7.6. The presence of NaCl did not alter the slope, hence the temperature coefficients are not affected by a salinity background.

Seawater multipoint calibration

Results from the seawater multipoint calibrations for three Pico-pH-SUB units indicate that the measurements were within ± 0.004 pH for a single calibration run against spectrophotometric measurements between pH 7.4–8.2 (Fig. 4a). This is derived from the range of all residuals between the pH optodes and the spectrophotometric measurements. These residuals are comparable with those from the DuraFET. The calibration can be further improved if the pH range is reduced. Reducing the range to 7.8–8.1 pH produced residuals of ± 0.002 between the Pico-pH-SUB and spectrophotometric samples. However, errors for measurements outside of the pH fit range increase substantially and can be as high as 0.1, highlighting the tradeoff associated with choice of calibration range. For each pH step of the seawater multipoint method, the precision (standard deviation) of the calculated pH output of the Pico-pH-SUB after calibration was ± 0.0006. For comparison, the DuraFET pH precision was ± 0.0004 demonstrating that the pHstat system was reliably stable and precise at each pH step.

The short-term accuracy of ± 0.004 pH was only achievable during single calibration runs. To investigate the repeatability of the seawater multipoint calibration method over multiple runs, coefficients determined from the first run were applied to three subsequent runs for a single Pico-pH-SUB unit,

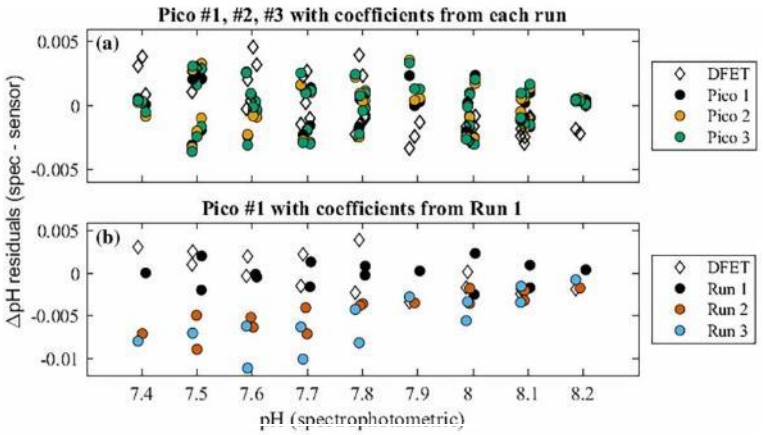

Fig. 4. (**a**) Residuals between spectrophotometric pH and the DuraFET pH (open diamonds) and pH calculated from the Pico-pH-SUB (filled circles) for three Pico-pH-SUB units during a seawater multipoint calibration. (**b**) Residuals between spectrophotometric pH and the DuraFET pH (open diamonds) and a single Pico-pH-SUB unit using coefficients from run 1 applied to sequential seawater multipoint calibration runs (filled circles).

conducted over 1 week (Fig. 4b). The residuals around the *pKa*, pH ~ 8, remained consistent between the calibration runs, but the magnitude of the residuals increased to ~ 0.01 pH at lower solution pH. Results were equivalent for all three Pico-pH-SUB units. Thus, we report a relative accuracy for the Pico-pH-SUB to be 0.01 over the nominal ocean pH range of 7.4–8.2.

If the PyroScience factory coefficients or three-point calibration coefficients were used to calculate pH during the seawater multipoint routine, residuals to the spectrophotometric samples were between 0.1 and 0.3 across the calibration range. This was anticipated, as the coefficients were established months before the seawater multipoint calibration. We conclude that drift, particularly in the *R*1 coefficient, invalidated the factory calibration. This emphasizes the importance of calibrating the Pico-pH-SUB as close as possible to time of use.

Pressure dependence

During the temperature and pressure cycling, the pH of the tris buffer was calculated as a function of temperature and pressure and compared to the pH output of the Pico-pH-SUB units. During pressurization, the pH of the tris buffer decreased while pH output from the Pico-pH-SUB increased (Fig. 5a). There was no pressure input for internal data processing on the Pico-pH-SUB, so the increase in pH observed in the Pico-pH-SUB output represents all combined pressure effects on the foil including the chemical properties of the fluorescent indicator.

When comparing the Pico-pH-SUB pH output to known pH of the tris buffer across the pressure range, there was good agreement across the three units and the replicates of Pico-pH-SUB unit 4 were almost identical to each other (Fig. 5b). Negligible effect in the pressure response was seen due to temperature. Thus, a constant pressure response of 0.029 pH/1000 dbar is recommended for all Pico-pH-SUB units. It is unknown if this response remains valid above 2000 dbar but was assumed applicable to the full 4000 dbar rating due to the linear relationship seen in this study. Further testing is required to verify the pressure coefficient above 2000 dbar.

Response time

The response time ranged from 195 to 750 s for the standard-response sensor tip, depending on temperature, and whether pH was increasing or decreasing (Fig. 6). In general, the direction of pH change played a significant role in response time, with a rising pH producing longer τ compared to falling pH at all temperatures. Average τ for both Pico-pH-SUB units at lower temperatures (~ 7°C) were 298 ± 34 s for falling and 660 ± 76 s for rising pH changes. Higher temperatures (~ 17°C) produced an average τ of 245 ± 48 s for falling and 378 ± 64 s for rising pH changes. Flow rate had a negligible impact on response time, which suggests that either diffusion within the sensor tip is the dominant process controlling the response time, or that the flow rates tested here with the sensor foil faced perpendicular to the flow was insufficient to significantly alter the boundary layer thickness at the sensor-water interface (Frankær and Sørensen 2019).

The τ values from this study were larger than reported in a previous study which stated response times of 125 s at 25°C and 145 s at 4°C for a similar pH sensitive material (Staudinger et al. 2019). They did not explore bidirectional changes in pH, or effects from flow rates. It is not clear why there was such a difference between the two studies.

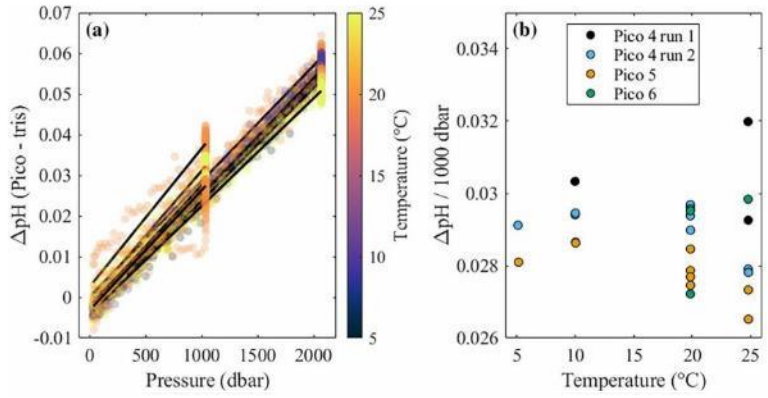

Fig. 5. (**a**) Difference in pH between the Pico-pH-SUB and tris buffer over 2000 dbar colored by temperature. Points correspond to both increasing and decreasing pressure. The black lines are the linear regression for each pressurization cycle at stable temperatures. (**b**) The difference in pH per 1000 dbar (slope magnitudes in (**a**)) for each Pico-pH-SUB. Pico 4 was temperature and pressure cycled twice.

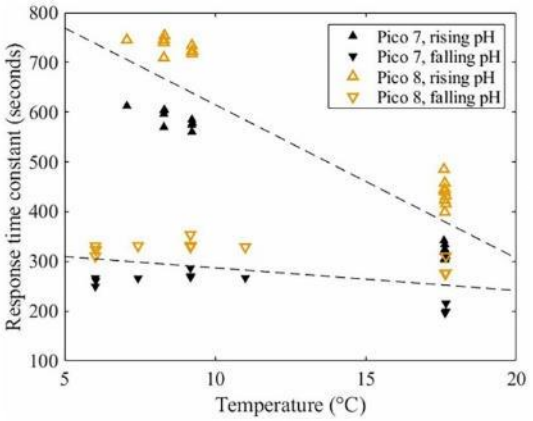

Fig. 6. Response time for two Pico-pH-SUB units with standard-response sensor tips as a function of temperature. Upward triangles represent a rising pH step change. Downward triangles represent a falling pH step change. Dashed lines are linear regressions through the rising and falling points, applied to both Pico-pH-SUB units.

The response time for the fast-response sensor tip was approximately 10 times faster than the standard foil (Table 2): 19 ± 3 s for falling and 62 ± 19 s for rising pH changes. These values align with the only previous study using the fast-response sensor tip (Staudinger et al. 2018). We did not explore the temperature effects on the response time of the fast-response sensor tip, but response time would decrease with increasing temperature, if diffusion processes control response time as hypothesized.

Table 2. Average response time constants (63.2%) for the Pico-pH-SUB from this study and previous literature. The downward arrow (↓) corresponds to tests done with falling pH step changes, upward arrow (↑) corresponds to rising pH step changes. The asterisk (*) represents the response time reported in each respective study, not necessarily the response time constant. The dash (-) represents unknown or not mentioned values.

Reference	Sensor tip type	Temperature (°C)	τ_{63} (s)
This study	Standard	7	298↓–659↑
		17	245↓–378↑
This study	Fast	6	19↓–62↑
Staudinger et al. (2019)	Standard	4	145↑
		25	125↑
Fritzsche et al. (2018)	-	-	20*
Staudinger et al. (2018)	Fast	-	< 60*

Field deployments

Station M

Throughout the nearly yearlong deployment, the temperature recorded by the AquapHOx-LX sensors remained stable, exhibiting a mean of 1.360 ± 0.006°C. Although there was a difference of ~ 0.12°C from the temperature reported by Smith et al. (2021) (Supporting Information Fig. S1b), the focus of this study lies more on the stability of the deep conditions and pH measurements than on absolute accuracy.

An initial conditioning of the Pico-pH-SUB loggers, lasting approximately 3 weeks was observed, yet the cause, whether pressure or temperature-related remains uncertain (Fig. 7). An

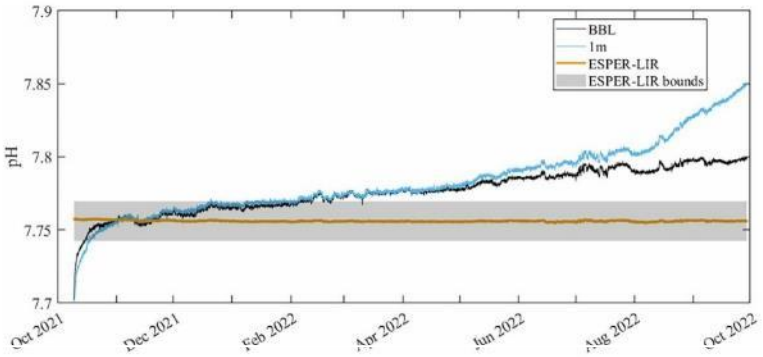

Fig. 7. Time series of two Pico-pH-SUB loggers attached to a bottom lander approximately 4000 m deep at Station M. One logger was just above the benthic boundary layer (BBL, black line) and another 1 m above the bottom (1m, blue line). A linearly interpolated regression (ESPER-LIR, yellow line) was estimated for the time series, with uncertainty bounds shown (shaded region). The logger pH values were adjusted to ESPER-LIR 21 d after deployment on 01 November 2021.

additional in situ *cal_offset* was applied at the 21-d mark on 01 November 2021 (0.063 pH for BBL logger and 0.016 pH for 1m logger) to facilitate visualization of sensor performance compared to the stable ESPER-LIR pH estimate.

Both sensors exhibited significant drift in the cold and stable environment, surpassing ESPER-LIR estimated uncertainty bounds of ± 0.014 within 3 months. Drift rates of the two sensors were nearly consistent for the first 6 months at a rate of 0.00016 pH d^{-1}. After 6 months the BBL logger continued a near linear drift while the 1m sensor drift increased significantly up to a maximum of 0.0008 pH d^{-1}.

Scripps pier

The nearshore environment at Scripps Pier exhibited a temperature range of 13–24°C and a pH range of 7.9–8.3 during the deployment (Fig. 8; Supporting Information Fig. S4). The SCS underwent two automated tris injections for sensor validation and correction, which yielded mean residuals within ± 0.004 pH between the SCS and in situ tris buffer pH values. The tris corrected SCS pH residuals to the two discrete bottle samples showed a consistent offset of −0.034 ± 0.016 pH, indicating no significant drift for the SCS pH. We are aware of this offset between the tris buffer and bottle sample residuals but maintain the methodology outlined in Bresnahan et al. (2021) to calibrate to the fourfold more consistent tris buffer injections. The deployment was divided into two periods: (1) 18 July–15 August 2023, characterized by stable conditions, and (2) 15 August–05 October 2023, marked by increased pH variability and significant drift of the Pico-pH-SUB.

During the first period, the mean difference between the Pico-pH-SUB and SCS was 0.108 ± 0.010 for the three-point calibration method and 0.004 ± 0.012 for the seawater multipoint method (Fig. 8). In the subsequent period of the deployment, the Pico-pH-SUB exhibited an increasing linear drift compared to the SCS for both calibration methods.

The availability of automated tris injections presented an opportunity for in situ adjustment of *cal_offset* and drift correction. The process involved calculating the difference between the in situ pH of the tris buffer at the time of injection and the pH recorded by the Pico-pH-SUB (Fig. 9). The adjusted *cal_offset* was then applied from the beginning of the deployment (18 July) to the first tris injection (15 August). A linear regression was fit from the first tris injection (15 August) to the second tris injection (12 September). This regression slope was then applied to the remaining measurements of the deployment after the first tris injection. The correction results were similar if the discrete bottle samples were used instead of the tris injections. Applying this correction to both calibration methods did not alter the results for the first month of the deployment besides improving the offset of the three-point calibration method to be more aligned with the SCS.

The in situ adjusted *cal_offset* applied to the multipoint calibration method at the first tris injection was negligible, measuring less than 0.001 pH. In contrast, the in situ adjusted *cal_offset* applied to the three-point calibration method was 0.082 pH. This in situ *cal_offset* adjustment relative to the first tris buffer injection is less than the difference between the Pico-pH-SUB and the SCS described above (0.108). This discrepancy may be due to the three-point calibration method deviating in accuracy away from the *pKa* of the sensor as the in situ pH of the tris buffer was ~ 8.3 for the first injection, or from a slower response to rising pH changes.

During the second period of the deployment, drift rates determined by the linear regression between the first and second tris injections were consistent for both calibration methods, measuring at 0.002 pH d^{-1}, aligning with previous

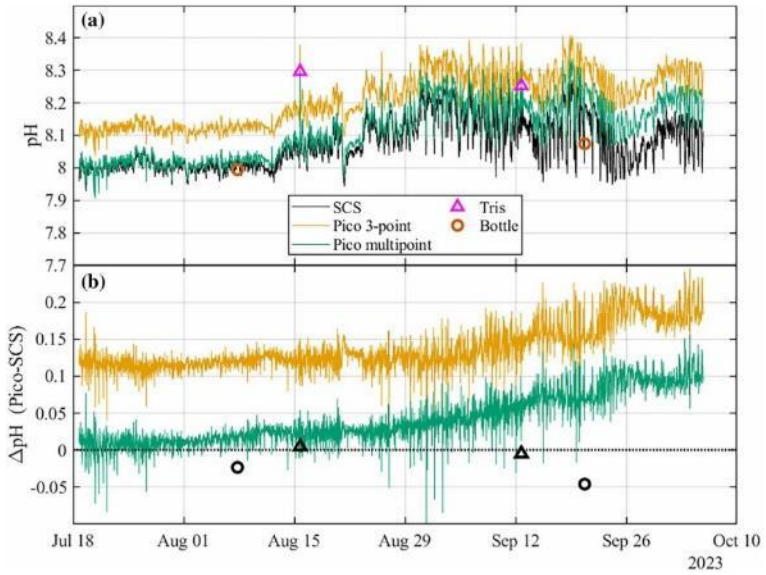

Fig. 8. (**a**) Time-series from Scripps Pier of tris-corrected Self-Calibrating SeapHOx (SCS) pH (black line) and uncorrected pH from the Pico-pH-SUB calculated using the pre-deployment three-point calibration (yellow line) and seawater multipoint calibration (green line). Discrete tris buffer (magenta triangles) and bottle samples (orange circles) also shown. (**b**) Difference between the Pico-pH-SUB and SCS pH for both calibration methods (yellow and green lines) and the difference between discrete samples (tris and bottle) in situ pH and SCS pH (black triangles and circles, respectively).

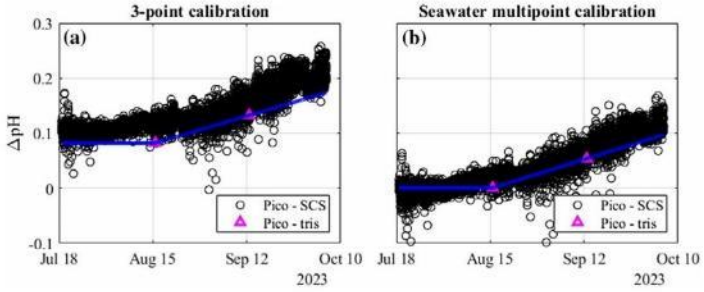

Fig. 9. (**a**) Difference in pH between the Pico-pH-SUB and Self-Calibrating SeapHOx (SCS) for the three-point calibration. (**b**) Difference in pH between the Pico-pH-SUB and SCS for the seawater multipoint calibration method (right). In situ pH offset and linear correction shown in blue lines corrected to the tris injections (magenta triangles).

studies (Fritzsche et al. 2018; Staudinger et al. 2018; Staudinger et al. 2019).

Post deployment in situ adjustments of *cal_offset* resulted in significantly improved agreement over the entire deployment (Fig. 10a). For the duration of the deployment, after the corrections to tris buffer were applied, residuals between the Pico-pH-SUB with the three-point calibration and the SCS were 0.027 ± 0.015, while those with the multipoint calibration were 0.010 ± 0.014. Both calibration methods exhibited good alignment with the SCS, although a larger difference was still observed for the three-point calibration method as previously noted. An observable reduction in the amplitude of Pico-pH-SUB measurements was observed in the second half of the deployment during coincident low pH and temperature

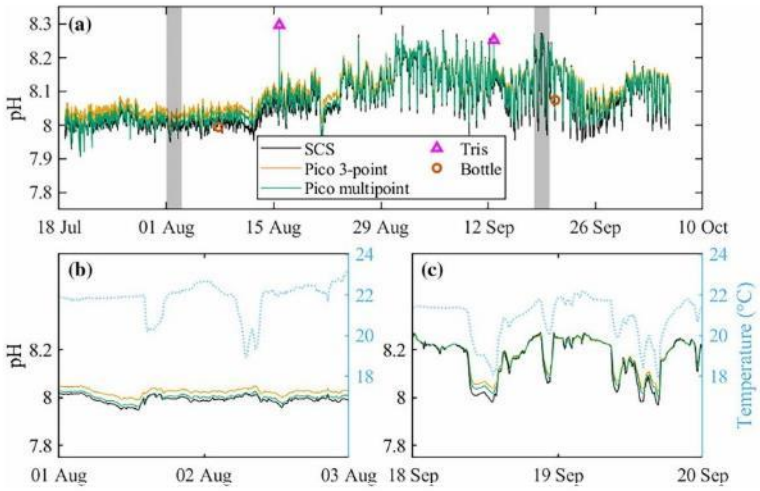

Fig. 10. (**a**) Time-series of the Self-Calibrating SeapHOx (SCS, black line) and Pico-pH-SUB with *cal_offset* adjustment and linear drift correction applied to both the three-point calibration method (yellow line) and seawater multipoint calibration (green line). Shaded regions show a zoom in between 01–03 August (**b**) and 18–20 September 2023 (**c**) with temperature (blue dashed line).

excursions (Fig. 10c). While some of the reduced amplitude of the Pico-pH-SUB relative to the SCS might be attributable to sensor lag, the sustained period of several hours on 18 September where the Pico-pH-SUB never "catches up" to the SCS may indicate a pH-dependent calibration error that is not captured by adjustments to *cal_offset* alone.

To assess the number of corrections necessary to recover data from a drifting Pico-pH-SUB, 2–10 simulated validation points were performed relative to the SCS (Supporting Information Fig. S5; $n = 6$ shown). This exercise indicated that an increase in the number of validation samples beyond two did not contribute to the improvement of Pico-pH-SUB correction, where the mean and standard deviation of the Pico-pH-SUB corrected pH relative to the hypothetical validation samples remained unchanged. This finding suggests that only two validation samples taken every 4 weeks was sufficient to correct the drift for this deployment.

Spray glider

The Pico-pH-SUB functioned properly throughout both glider missions, demonstrating the capability to withstand repeated profiles to 1000 dbar. Over multiple dives, Pico-pH-SUB measurements at depths below 800 dbar (where pH is generally constant) agreed to better than 0.003, which is comparable to the performance of the DSD (Johnson et al. 2016; Takeshita et al. 2021*a*,*b*). However, the standard-response sensor tip experienced a large hysteresis that reached > 0.1 pH near the surface between ascending and descending profiles (Fig. 11a). An additional *cal_offset* of 0.05 pH was required to align the Pico-pH-SUB with CANYON-B estimates below 900 dbar. Relative to the estimated pH from the CANYON-B algorithm, the Pico-pH-SUB pH was lower on the descent and higher on the ascent in the upper part of the water column. This pattern indicates that this hysteresis was caused by the slow response time of the sensor. In theory, the slow response time can be accounted for, as is done for oxygen optodes (Bittig et al. 2018). However, applying corrections with a response time of 400 s using this approach resulted in excessively noisy readings > 0.5 pH throughout the entire profile.

In contrast, the fast-response sensor tip exhibited significantly smaller hysteresis between ascending and descending profiles (Fig. 11b). The magnitude of the hysteresis was < 0.02 pH. Small scale vertical variability and features were captured by the Pico-pH-SUB above 300 dbar, similar to the DSD. However, there was a large discrepancy between the DSD and Pico-pH-SUB utilizing pre-deployment calibration coefficients for this deployment. These Pico-pH-SUB profiles appeared skewed and muted, indicating a sigmoid shift between pre-deployment calibration and deployment. The cause of this shift remains unknown, but potential sources include the expulsion of an air bubble between the sensor tip and optoelectronics during pressurization or movement of the screw-on sensor tip.

Immediately following the fast-response sensor tip recovery, the Pico-pH-SUB underwent a post-deployment recalibration using the seawater multipoint method. Applying these post-deployment calibrations resulted in improved alignment with the DSD pH, demonstrating that the calibration coefficients did in fact shift before deployment. This is

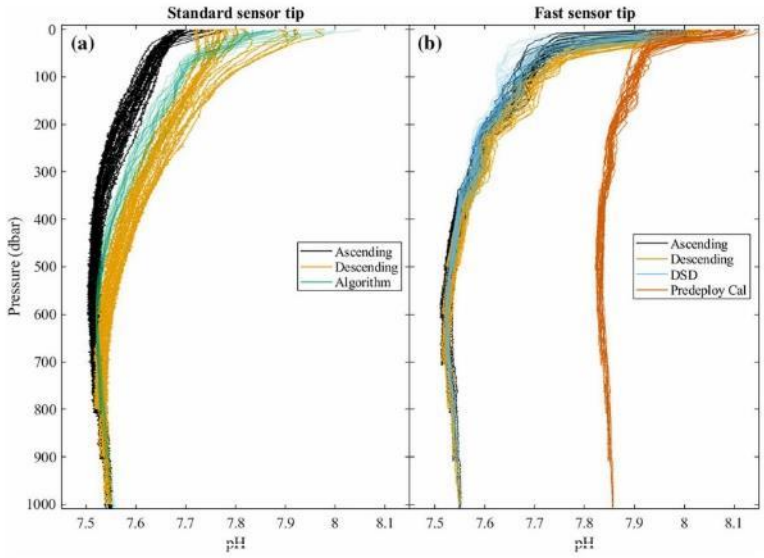

Fig. 11. (**a**) Profiles of the standard-response sensor tip that measured on both the ascent (black) and descent (yellow), greater than 500 dbar. CANYON-B algorithm (green) calculated for ascending profiles only. (**b**) Ascending and descending profiles of the fast-response sensor tip down to 500 dbar and deeper utilizing post-deployment calibration coefficients (black and yellow). Profiles using pre-deployment calibration coefficients are shown for ascending profiles only (orange). Ascending Deep-Sea DuraFET (DSD) profiles (blue) were only available on the fast-response sensor tip deployment.

troubling, as the pH optode was calibrated within 1 week of deployment on the glider. An additional *cal_offset* of 0.081 pH was required to align the Pico-pH-SUB with CANYON-B estimates below 900 dbar. Ascending profiles exhibited improved alignment with DSD profiles, likely influenced by increasing temperature and shortened response time during ascent.

During the short deployments, Pico-pH-SUB profiles displayed drift discernable for both the standard and fast-response sensor tips (Supporting Information Fig. S6). To calculate the drift rate, ascending profiles starting from depths over 500 dbar were selected. The mean pH value between 500 and 600 dbar was calculated for only ascending profiles to exclude hysteresis effects, and because this range had more profiles where pH was assumed to be stable. A linear regression of mean pH with time yielded drift rates of 0.005 pH d^{-1} for the standard-response sensor tip and 0.006 pH d^{-1} for the fast-response sensor tip at an average temperature of $\sim 6°C$. No drift was observed for the DSD.

Discussion

In this study, we conducted a thorough assessment of the Pico-pH-SUB pH optode for oceanographic applications, aiming to evaluate its potential as an alternative pH sensor to currently available technologies. Multiple calibration methods were scrutinized, with the seawater multipoint method yielding the most accurate results as it determines all four sigmoid coefficients within the functional range in natural seawater media. This calibration method had a relative, short-term accuracy of 0.004 in the lab over a pH range of 7.4–8.2 compared against spectrophotometric measurements. The accuracy was improved when analyzed over a smaller pH range, ~ 0.002 for pH 7.8–8.1. This accuracy would only apply to measurements immediately following calibration, and only over this range. Repetitions over 1 week resulted in an accuracy of 0.01 for the full range (7.4–8.2), which is applicable to most practices using the Pico-pH-SUB and the accuracy reported here. The residuals were largest at lower pH values, suggesting that the $R1$ coefficient was potentially drifting or changing between calibration runs, or a pH-dependent drift was present. The offset in $R1$ during the three-point calibration due to NaCl addition highlights the importance of using solutions with similar ionic strength or composition as the target solution. Calibration should be carried out as close in time to deployment as possible, and an additional *cal_offset* may be required once the sensor is deployed.

Minor variances were noted in $R1_T$ and $R2_T$ when comparing manufacturer-provided values with those derived from the temperature cycle method. The changes in calculated pH due to changes in $R1_T$ and $R2_T$ are small, but for applications

spanning large temperature and pH ranges they can be significant. These variances were attributed to methodological disparities between this study and those from the manufacturer. PyroScience temperature coefficients were determined by subjecting artificial seawater to temperature cycling across the functional pH range. Producing the temperature coefficients at the top and bottom of the asymptote will provide a more robust and repeatable value, but determining the coefficients in seawater may be advantageous for oceanographic applications, analogous to the seawater multipoint methodology.

Drift was observed across all field deployments, ranging from 0.0002 pH d^{-1} (deep, cold environment), 0.002 pH d^{-1} (shallow, dynamic environment) to 0.006 pH d^{-1} (profiling). The unexplained initial conditioning of approximately 3 weeks only observed during the Station M deployment raises concerns for short-term deployments in the deep sea. It is implied that Pico-pH-SUB units with sensor tips from the same batch may exhibit similar drift for the initial 6 months but may be batch-dependent. The difference in drift rates seen throughout the study suggests that they were temperature and pH dependent. Lower temperature deployments had lower drift rates, and lower in situ pH had higher drift rates. The presence of nonlinear drift rates complicates drift correction, emphasizing the need for further exploration and quantification of these phenomena.

Despite a relatively long response time of the standard-response sensor tip, the pH optode effectively tracked dynamic pH variability in the near-shore environment at Scripps Pier, showcasing comparable performance to the SCS and DuraFET pH sensor. The multipoint calibration method proved to be a more accurate calibration approach, but both calibration methods captured the dynamic variability nearly equally once an in situ *cal_offset* adjustment was applied. This in situ *cal_offset* adjustment is similarly used for oxygen optodes that experience calibration shifts between the lab and field (Takeshita et al. 2013; Bittig et al. 2018). The larger in situ *cal_offset* adjusted value of 0.082 pH for the three-point calibration method is due to the seawater multipoint method's characterization of sigmoid over the desired the pH range and its timing, performed 2 months before the seawater multipoint method.

Using the automated in situ tris buffer validation samples proved to be a robust method for correcting the initial offset and linear drift. By examining a range of hypothetical validation samples, taking more than two samples did not improve the correction, suggesting that taking validation samples every 4 weeks is sufficient. However, caution is advised against delaying validation sample collection too long after the start of deployment, as sensor drift may have already influenced the data, potentially leading to an overestimation of the in situ *cal_offset* adjustment.

The standard-response sensor tip proved unsuitable for profiling applications. The fast-response sensor tip showed promise for profiling applications but experienced a calibration shift between the lab and deployment. For long-term profiling applications, like profiling floats, which are typically not recovered, post-deployment calibration of the sigmoid coefficients is challenging. Extrapolating the drift rate observed for the fast-response sensor tip, the expected drift rate would be 0.06 pH per profile for a standard 10-d profiling interval for BGC-Argo floats, which would be unacceptably large.

In its current state, the Pico-pH-SUB seems best suited for short-term deployments on the order of weeks to months, aimed to capture weather-scale pH variability of 0.02 (Newton et al. 2015). With careful attention to calibration, the sensor could provide high-quality short-term measurements on shipboard rosette profiles and underway mapping applications in addition to shore-based experiments such as controlling or monitoring pH levels for mesocosm studies focused on ocean acidification and marine carbon dioxide removal experiments (Bockmon et al. 2013; Fuhr et al. 2024). The swappable sensor tips, uncomplicated three-point calibration and sensor integration make it a valuable addition to the short list of viable pH sensor technologies available to the oceanographic community.

Comments and recommendations

From this work, here we outline recommendations for Pico-pH-SUB users to achieve the highest quality data possible:

- Hydrate the sensor tip in sea water for at least 24 h preceding any measurements.
- Temperature cycling to verify $R1_T$ and $R2_T$ is simple, and the coefficients can be applied to an entire batch of sensor tips. This is most likely unnecessary for most applications, as these coefficients do not greatly affect calculated pH.
- For laboratory calibration, the seawater multipoint method is the most accurate, but likely too difficult and time intensive for most users.
  - The three-point calibration proved to be comparable in performance and is recommended for most users. Only two-points may be sufficient (*R*1 and *R*2) as *cal_offset* adjustment will most likely be required after the laboratory calibration.
  - Performing either calibration method as close to time of deployment may minimize the *cal_offset* adjustment.
  - Laboratory calibration should be performed in solutions similar in ionic strength to the deployment location.
- An in situ *cal_offset* adjustment based on a discrete validation sample taken alongside the sensor may be required and is recommended to be conducted early in the deployment (< 1 week) before drift takes over.
- It may be possible to correct for drift with multiple validation samples taken throughout the deployment. Validation samples every 3–4 weeks and at the end of the deployment are recommended to maintain the weather objective quality of 0.02 pH.
- Short-term profiling applications on Spray gliders or other profiling platforms would require use of the fast-response

sensor foil, with sensor refinement to reduce or eliminate the potential for offsets between calibration and deployment. Recoverable, short-term deployments may allow for post-deployment re-calibration.

References

Bittig, H. C., B. Fiedler, R. Scholz, G. Krahmann, and A. Körtzinger. 2014. Time response of oxygen optodes on profiling platforms and its dependence on flow speed and temperature. Limnol. Oceanogr.: Methods **12**: 617–636. doi:10.4319/lom.2014.12.617

Bittig, H. C., and others. 2018. Oxygen optode sensors: Principle, characterization, calibration, and application in the ocean. Front. Mar. Sci. **4**: 429. doi:10.3389/fmars.2017.00429

Bockmon, E. E., C. A. Frieder, M. O. Navarro, L. A. White-Kershek, and A. G. Dickson. 2013. Technical note: Controlled experimental aquarium system for multi-stressor investigation of carbonate chemistry, oxygen saturation, and temperature. Biogeosciences **10**: 5967–5975. doi:10.5194/BG-10-5967-2013

Bresnahan, P. J., and others. 2021. Autonomous in situ calibration of ion-sensitive field effect transistor pH sensors. Limnol. Oceanogr.: Methods. **19**: 132–144. doi:10.1002/lom3.10410

Bushinsky, S. M., Y. Takeshita, and N. L. Williams. 2019. Observing changes in ocean carbonate chemistry: Our autonomous future. Curr. Clim. Change Rep. **5**: 207–220. doi:10.1007/s40641-019-00129-8

Carter, B. R., J. A. Radich, H. L. Doyle, and A. G. Dickson. 2013. An automated system for spectrophotometric seawater pH measurements. Limnol. Oceanogr.: Methods **11**: 16–27. doi:10.4319/lom.2013.11.16

Carter, B. R., and others. 2021. New and updated global empirical seawater property estimation routines. Limnol. Oceanogr.: Methods **19**: 785–809. doi:10.1002/lom3.10461

Chavez, F. P., J. Sevadjian, C. Wahl, J. Friederich, and G. E. Friederich. 2018. Measurements of pCO_2 and pH from an autonomous surface vehicle in a coastal upwelling system. Deep-Sea Res. II: Top. Stud. Oceanogr. **151**: 137–146. doi:10.1016/j.dsr2.2017.01.001

Clarke, J. S., E. P. Achterberg, V. M. C. Rérolle, S. Abi Kaed Bey, C. F. A. Floquet, and M. C. Mowlem. 2015. Characterisation and deployment of an immobilised pH sensor spot towards surface ocean pH measurements. Anal. Chim. Acta **897**: 69–80. doi:10.1016/j.aca.2015.09.026

Claustre, H., K. S. Johnson, and Y. Takeshita. 2020. Observing the global ocean with biogeochemical-Argo. Annu. Rev. Mar. Sci. **12**: 23–48. doi:10.1146/annurev-marine-010419-010956

Clayton, T. D., and R. H. Byrne. 1993. Spectrophotometric seawater pH measurements: Total hydrogen ion concentration scale calibration of *m*-cresol purple and at-sea results. Deep-Sea Res. I: Oceanogr. Res. Pap. **40**: 2115–2129. doi:10.1016/0967-0637(93)90048-8

Cyronak, T., and others. 2020. Diel temperature and pH variability scale with depth across diverse coral reef habitats. Limnol. Oceanogr.: Lett. **5**: 193–203. doi:10.1002/lol2.10129

DelValls, T. A., and A. G. Dickson. 1998. The pH of buffers based on 2-amino-2-hydroxymethyl-1,3-propanediol ('tris') in synthetic sea water. Deep-Sea Res. Part 1 Oceanogr. Res. Pap. **45**: 1541–1554. doi:10.1016/S0967-0637(98)00019-3

Donham, E. M., I. Flores, A. Hooper, E. O'Brien, K. Vylet, Y. Takeshita, J. Freiwald, and K. J. Kroeker. 2023. Population-specific vulnerability to ocean change in a multistressor environment. Sci. Adv. **9**: eade2365. doi:10.1126/sciadv.ade2365

Frankær, C. G., and T. J. Sørensen. 2019. Investigating the time response of an optical pH sensor based on a polysiloxane–polyethylene glycol composite material impregnated with a pH-responsive triangulenium dye. ACS Omega **4**: 8381–8389. doi:10.1021/acsomega.9b00795

Fritzsche, E., and others. 2018. A validation and comparison study of new, compact, versatile optodes for oxygen, pH and carbon dioxide in marine environments. Mar. Chem. **207**: 63–76. doi:10.1016/j.marchem.2018.10.009

Fuhr, M., and others. 2024. Alkaline mineral addition to anoxic to hypoxic Baltic Sea sediments as a potentially efficient CO_2-removal technique. Front. Clim. **6**: 1338556. doi:10.3389/fclim.2024.1338556

Gray, A. R., and others. 2018. Autonomous biogeochemical floats detect significant carbon dioxide outgassing in the high-latitude Southern Ocean. Geophys. Res. Lett. **45**: 9049–9057. doi:10.1029/2018GL078013

Hofmann, G. E., and others. 2011. High-frequency dynamics of ocean pH: A multi-ecosystem comparison. PLoS One **6**: e28983. doi:10.1371/journal.pone.0028983

Hughes, B. B., S. C. Lummis, S. C. Anderson, and K. J. Kroeker. 2018. Unexpected resilience of a seagrass system exposed to global stressors. Glob. Change Biol. **24**: 224–234. doi:10.1111/gcb.13854

International Ocean Carbon Coordination Project (IOCCP). 2024. Instruments and sensors: Hardware pH directory. Accessed 7 August 2024. https://www.ioccp.org/index.php/hardware-listing/hardware-ph

Johengen, T., G. J. Smith, D. Schar, M. Atkinson, H. Purcell, D. Loewensteiner, Z. Epperson, and M. Tamburri. 2015. Performance Demonstration for Autonomous pH sensor technologies, UMCES Technical Report Series: Ref. No. [UMCES] CBL 2015-008, CBL 2015-009, CBL 2015-010, CBL 2015-011, CBL 2015-012, CBL 2015-013, CBL 2015-014. Accessed 7 August 2024. http://www.act-us.info/

Johnson, K. S., H. W. Jannasch, L. J. Coletti, V. A. Elrod, T. R. Martz, Y. Takeshita, R. J. Carlson, and J. G. Connery. 2016. Deep-Sea DuraFET: A pressure tolerant pH sensor designed for global sensor networks. Anal. Chem. **88**: 3249–3256. doi:10.1021/acs.analchem.5b04653

Johnson, K. S., and others. 2017. Biogeochemical sensor performance in the SOCCOM profiling float array. J. Geophys. Res.: Oceans **122**: 6416–6436. doi:10.1002/2017JC012838

Kekuewa, S. A. H., T. A. Courtney, T. Cyronak, and A. J. Andersson. 2022. Seasonal nearshore ocean acidification and deoxygenation in the Southern California Bight. Sci. Rep. **12**: 17969. doi:10.1038/s41598-022-21831-y

Klimant, I., C. Huber, G. Liebsch, G. Neurauter, A. Stangelmayer, and O. S. Wolfbeis. 2001. Dual lifetime referencing (DLR)—A new scheme for converting fluorescence intensity into a frequency-domain or time-domain information, p. 257–274. *In* B. Valeur and J. C. Brochon [eds.], New trends in fluorescence spectroscopy. Springer. doi:10.1007/978-3-642-56853-4_13

Lauvset, S. K., and others. 2022. GLODAPv2.2022: The latest version of the global interior ocean biogeochemical data product. Earth Syst. Sci. Data **14**: 5543–5572. doi:10.5194/essd-14-5543-2022

Lilly, L. E., U. Send, M. Lankhorst, T. R. Martz, R. A. Feely, A. J. Sutton, and M. D. Ohman. 2019. Biogeochemical anomalies at two Southern California Current System moorings during the 2014–2016 warm anomaly-El Niño sequence. J. Geophys. Res.: Oceans **124**: 6886–6903. doi:10.1029/2019JC015255

Martz, T. R., J. G. Connery, and K. S. Johnson. 2010. Testing the Honeywell Durafet® for seawater pH applications. Limnol. Oceanogr.: Methods **8**: 172–184. doi:10.4319/lom.2010.8.172

Martz, T., K. Daly, R. Byrne, J. Stillman, and D. Turk. 2015. Technology for Ocean Acidification Research: Needs and availability. Oceanography **25**: 40–47. doi:10.5670/oceanog.2015.30

Maurer, T. L., J. N. Plant, and K. S. Johnson. 2021. Delayed-mode quality control of oxygen, nitrate, and pH data on SOCCOM biogeochemical profiling floats. Front. Mar. Science **8**: 683207. doi:10.3389/fmars.2021.683207

Monk, S. A., and others. 2021. Detecting and mapping a CO_2 plume with novel autonomous pH sensors on an underwater vehicle. Int. J. Greenhouse Gas Control **112**: 103477. doi:10.1016/j.ijggc.2021.103477

Mowlem, M., and others. 2021. Industry partnership: Lab on chip chemical sensor technology for ocean observing. Front. Mar. Sci. **8**: 697611. doi:10.3389/fmars.2021.697611

Müller, J. D., F. Bastkowski, B. Sander, S. Seitz, D. R. Turner, A. G. Dickson, and G. Rehder. 2018. Metrology for pH measurements in brackish waters—Part 1: Extending electrochemical pHT measurements of Tris buffers to salinities 5–20. Front. Mar. Sci. **5**: 176. doi:10.3389/fmars.2018.00176

Newton, J. A., R. A. Feely, E. B. Jewett, P. Williamson, and J. Mathis. 2015. Global ocean acidification observing network: Requirements and governance plan. GOA-ON Global Ocean Acidification Observing Network. https://www.iaea.org/sites/default/files/18/06/goa-on-second-edition-2015.pdf

Rérolle, V. M. C., C. F. A. Floquet, M. C. Mowlem, D. P. Connelly, E. P. Achterberg, and R. R. G. J. Bellerby. 2012. Seawater-pH measurements for ocean-acidification observations. TrAC Trends Anal. Chem. **40**: 146–157. doi:10.1016/j.trac.2012.07.016

Ricart, A. M., and others. 2021. Coast-wide evidence of low pH amelioration by seagrass ecosystems. Glob. Change Biol. **27**: 2580–2591. doi:10.1111/GCB.15594

Rivest, E. B., M. O'Brien, L. Kapsenberg, C. C. Gotschalk, C. A. Blanchette, U. Hoshijima, and G. E. Hofmann. 2016. Beyond the benchtop and the benthos: Dataset management planning and design for time series of ocean carbonate chemistry associated with Durafet®-based pH sensors. Eco. Inform. **36**: 209–220. doi:10.1016/j.ecoinf.2016.08.005

Rodriguez, C., F. Huang, and F. J. Millero. 2015. The partial molal volume and compressibility of Tris and Tris–HCl in water and 0.725 m NaCl as a function of temperature. Deep-Sea Res. I: Oceanogr. Res. Pap. **104**: 41–51. doi:10.1016/j.dsr.2015.06.008

Saba, G. K., and others. 2019. The development and validation of a profiling glider deep ISFET-based pH sensor for high resolution observations of coastal and ocean acidification. Front. Mar. Sci. **6**: 664. doi:10.3389/FMARS.2019.00664

Sherman, J., R. E. Davis, W. B. Owens, and J. Valdes. 2001. The autonomous underwater glider "spray". IEEE J. Oceanic Eng. **26**: 437–446. doi:10.1109/48.972076

Smith, K. L., Jr., M. B. Laver, and N. O. Brown. 1983. Sediment community oxygen consumption and nutrient exchange in the central and eastern North Pacific. Limnol. Oceanogr. **28**: 882–898. doi:10.4319/lo.1983.28.5.0882

Smith, K. L., Jr., A. D. Sherman, P. R. McGill, R. G. Henthorn, J. Ferreira, T. P. Connolly, and C. L. Huffard. 2021. Abyssal Benthic Rover, an autonomous vehicle for long-term monitoring of deep-ocean processes. Science Robotics **6**: eabl4925. doi:10.1126/scirobotics.abl4925

Smith, K. L., Jr., M. Messié, T. P. Connolly, and C. L. Huffard. 2022. Decadal time-series depletion of dissolved oxygen at abyssal depths in the Northeast Pacific. Geophys. Res. Lett. **49**: e2022GL101018. doi:10.1029/2022GL101018

Staudinger, C., and others. 2018. A versatile optode system for oxygen, carbon dioxide, and pH measurements in seawater with integrated battery and logger. Limnol. Oceanogr.: Methods **16**: 459–473. doi:10.1002/lom3.10260

Staudinger, C., M. Strobl, J. Breininger, I. Klimant, and S. M. Borisov. 2019. Fast and stable optical pH sensor materials for oceanographic applications. Sens. Actuators B Chem. **282**: 204–217. doi:10.1016/j.snb.2018.11.048

Takeshita, Y., T. R. Martz, K. S. Johnson, J. N. Plant, D. Gilbert, S. C. Riser, C. Neill, and B. Tilbrook. 2013. A climatology-based quality control procedure for profiling float oxygen data. J. Geophys. Res.: Oceans **118**: 5640–5650. doi:10.1002/jgrc.20399

Takeshita, Y., T. R. Martz, K. S. Johnson, and A. G. Dickson. 2014. Characterization of an ion sensitive field effect transistor and chloride ion selective electrodes for pH

measurements in seawater. Anal. Chem. **86**: 11189–11195. doi:10.1021/ac502631z

Takeshita, Y., T. R. Martz, L. J. Coletti, A. G. Dickson, H. W. Jannasch, and K. S. Johnson. 2017. The effects of pressure on pH of Tris buffer in synthetic seawater. Mar. Chem. **188**: 1–5. doi:10.1016/J.MARCHEM.2016.11.002

Takeshita, Y., T. Cyronak, T. R. Martz, T. Kindeberg, and A. J. Andersson. 2018. Coral reef carbonate chemistry variability at different functional scales. Front. Mar. Sci. **5**: 175. doi:10.3389/FMARS.2018.00175

Takeshita, Y., and others. 2021*a*. Accurate pH and O_2 measurements from spray underwater gliders. J. Atmos. Ocean. Technol. **38**: 181–195. doi:10.1175/JTECH-D-20-0095.1

Takeshita, Y., and others. 2021*b*. Consistency and stability of purified meta-cresol purple for spectrophotometric pH measurements in seawater. Mar. Chem. **236**: 104018. doi:10.1016/J.MARCHEM.2021.104018

Tengberg, A., and others. 2006. Evaluation of a lifetime-based optode to measure oxygen in aquatic systems. Limnol. Oceanogr.: Methods **4**: 7–17. doi:10.4319/lom.2006.4.7

U.S. Integrated Ocean Observing System (US IOOS). 2021. Manual for real-time quality control of water level data Version 2.1: A guide to quality control and quality assurance of water level observations. doi:10.25923/vpsx-dc82

Yin, T., and others. 2021. A novel lab-on-chip spectrophotometric pH sensor for autonomous in situ seawater measurements to 6000 m depth on stationary and moving observing platforms. Environ. Sci. Technol. **55**: 14968–14978. doi:10.1021/acs.est.1c03517

Acknowledgments

This work was funded by NSF OCE2300399, NSF OCE2300400, and the David and Lucile Packard Foundation. Dariia Atamanchuk, Mathieu Dever, Clark Richards and the rest of the Dalhousie Aquatron Flume team were instrumental in conducting the response time experiments. The Station M deployment and data collection was made possible by Ken Smith Jr., Alana Sherman, Rich Henthorn, and Paul McGill. Melissa Carter and Kayla Martin facilitated the deployment and recovery at Scripps Pier. We thank Jacki Long, James McClure, Chris Wahl, and Brent Jones for Spray glider preparation, deployment, and recovery.

Conflict of Interest

Christoph Staudinger was employed by PyroScience GmbH. All other authors declare no conflict of interest.

Submitted 17 June 2024
Revised 12 August 2024
Accepted 22 August 2024

Associate editor: Isaac Santos

Acknowledgements

Chapter 2, in full, is a reprint of the material as it appears in *Limnology & Oceanography: Methods*. Wirth, T., Takeshita, Y., Davis, B., Park, E., Hu, I., Huffard, C. L., Johnson, K. S., Nicholson, D., Staudinger, C., Warren, J. K., & Martz, T., 2024. The dissertation author was the primary investigator and author of this paper.

Chapter 3 Subsurface biogeochemical variability in the equatorial Pacific observed by BGC-Argo floats over the 2019-2024 ENSO cycle

Key Points

- BGC-Argo profiling floats in the equatorial Pacific revealed greater subsurface biogeochemical variability than at the surface, depending on ENSO state.
- Biogeochemical variability was primarily driven by vertical movement of the thermocline and meridional transport of South Pacific Tropical Water (SPTW).
- A Biogeochemical Multivariate ENSO Index (BMEI) was developed and used to investigate the disparity between modes of surface and subsurface biogeochemical variability.

Abstract

The El Niño Southern Oscillation (ENSO) cycles from 2019 to 2024 featured an unprecedented sequence of extreme events, initiated by a weak El Niño transitioning into a rare three-year (“triple-dip”) La Niña, followed by one of the strongest El Niño on record. While these events are known to induce significant physical changes in the ocean, little has been reported on the corresponding subsurface biogeochemical variability and its relationship to the ENSO state. Leveraging observations from an array of BGC-Argo profiling floats in the equatorial Pacific Niño 3.4 region, we investigated the biogeochemical impacts of ENSO during this period, focusing on subsurface anomalous features relative to a climatology. Anomalies of oxygen, nitrate and dissolved inorganic carbon were most pronounced at depths below the mixed layer, revealing distinct correlations with Kelvin Wave activity and meridional transport. Redistribution of phytoplankton was also observed, with higher concentrations deeper in the water column during the El Niño phases relative to La Niña. We propose the concept of a Biogeochemical Multivariate ENSO Index (BMEI), analogous to the multitude of other multivariate indexes used in this region, exploring modes of variability and its utility to gauge intensity of ENSO phases.

This study underscores the importance of continued BGC-Argo observations to enhance our understanding of subsurface biogeochemical processes and their potential for assessing the severity of future ENSO cycles.

Plain Language Summary

From 2019 to 2024, the El Niño Southern Oscillation (ENSO) cycles experienced a rare three-year La Niña, followed by a very strong El Niño. These extreme events are known to cause significant changes in ocean temperature and circulation, but how they affect the ocean's subsurface biogeochemistry is less understood. Using data from Biogeochemical Argo (BGC-Argo) profiling floats in the equatorial Pacific, this study examined how ENSO impacted the ocean's biogeochemical variability of oxygen, nutrients, carbon, and chlorophyll-a, highlighting features at depths below the surface that have been difficult to capture with previous monitoring efforts.

Introduction

The El Niño Southern Oscillation (ENSO) is a naturally occurring climate phenomenon characterized by fluctuations in oceanic and atmospheric conditions across the tropical Pacific. Under normal conditions, trade winds push warm surface water toward the western Pacific, pooling it near Asia and Australia. However, during ENSO events, these trade winds weaken or even reverse, allowing the warm water to spread eastward across the Pacific toward the Americas. This shift in oceanic circulation defines the two main ENSO phases: El Niño, the warm phase, and La Niña, the cold phase (Trenberth, 1997). Typically, ENSO cycles occur every 2-7 years, with varying intensity and duration. These events have far-reaching impacts, influencing global weather patterns, including altering precipitation, temperature, and atmospheric circulation across many regions of the world.

Historically, oceanic monitoring of ENSO has focused primarily on physical parameters such as sea surface temperature (SST) and salinity, largely through surface measurements in

the Equatorial Pacific. Data from ships, the Tropical Atmosphere Ocean (TAO) mooring array, and the Tropical Pacific Observing System (TPOS) have provided continuous surface observations over several decades (McPhaden et al., 1998; Smith et al., 2010; McPhaden et al., 2010). The advent of satellite remote sensing expanded this capability, allowing for high-resolution SST monitoring across vast ocean regions. Since the early 2000s, the Argo program has also contributed by enabling global subsurface temperature and salinity observations down to 2000 meters (Roemmich et al., 2009). However, despite these advancements, the subsurface ocean, particularly its biogeochemical characteristics, has been less extensively studied in the context of ENSO variability (Christian et al., 2001; Smith et al., 2019).

Some previous studies have explored various biogeochemical processes in the equatorial Pacific, such as changes in primary production (Strutton & Chavez, 2000; Gierach et al., 2012; Brainard et al., 2018), but these investigations were typically limited to large spatial scales using satellite or shipboard measurements. Similarly, variability in surface CO_2 flux has been studied using moorings (Sutton et al., 2014; Liao et al., 2020; Pittman et al., 2022), leaving the subsurface inorganic carbon system relatively unexplored. Oxygen variability, often tied to vertical shifts in thermocline depth and upwelling modulated by ENSO, has also been observed, with oxygen sensors being the most common biogeochemical sensor deployed on floats (Czeschel et al., 2012; Eddebbar et al., 2017; Leung et al., 2019). Additionally, changes in nutrient supply, closely linked to ENSO phases, show surface nutrient depletion during El Niño events due to reduced equatorial upwelling (Strutton et al., 2008; Turk et al., 2011). Despite these efforts, a comprehensive understanding of subsurface biogeochemical dynamics and interactions remains elusive, particularly in relation to ENSO's varying phases.

Since 2019, the Biogeochemical Argo (BGC-Argo) program has provided a new observational tool, enabling continuous measurements of biogeochemical parameters such as oxygen, pH, nutrient and chlorophyll-a concentrations at depths down to 2000 meters (Claustre et al., 2020). These datasets offer the ability to view how subsurface biogeochemical processes

respond to ENSO-driven physical changes in the ocean. Given the complexity of the tropical Pacific and its role as the epicenter of ENSO activity, there is a growing interest in understanding the interplay between subsurface biogeochemical variability and the well-established physical indicators of ENSO (Turk et al., 2001; Mathis et al., 2014; Kessler & Cravatte, 2021).

The ENSO state is traditionally quantified using the Oceanic Niño 3.4 (ONI) index, which measures sea surface temperature anomalies relative to a 30-year climatological average in the central equatorial Pacific region, spanning from 5°S-5°N and 170°W-120°W. The period from 2019 to 2024 presents a unique case for investigation, characterized by an unusual sequence of ENSO events, including a historic "triple-dip" La Niña encompassing March 2020 – February 2024 (Li et al., 2023; Jiang et al., 2023), followed by the onset of one of the strongest El Niños on record. This study aims to explore subsurface biogeochemical variability throughout these extreme ENSO phases, using data from BGC-Argo floats in the Niño-3.4 region. Specifically, we examine how biogeochemical parameters align with the Oceanic Niño Index (ONI) and extend this analysis into the subsurface. By investigating where and when biogeochemical variability corresponds or diverges from physical ENSO patterns, this work seeks to provide new insights into the ocean's biogeochemical response to these significant climatic events.

Data and Methods

Oceanic Niño Index

The NOAA Oceanic Niño Index (ONI, Figure 3.1a) represents the monthly sea surface temperature anomaly in the Niño-3.4 region (5°S-5°N, 170°W-120°W). The anomalies were calculated relative to a 30-year baseline period from 1991 to 2020. ONI data were obtained from NOAA's National Centers for Environmental Prediction (NCEP).

BGC-Argo profiling floats

Biogeochemical Argo (BGC-Argo) profiling floats are drifting, autonomous robots that collect measurements in the upper 2000 meters of the ocean every ~10 days. They measure temperature and salinity, along with a suite of biogeochemical sensors. At the surface, data is telemetered back to shore via satellite before resuming the 10-day profiling routine. This process continues until the float's battery is depleted, typically after 4-5 years.

In the Niño-3.4 region (5°S to 5°N, 170°W to 120°W), 23 BGC-Argo floats were selected, covering the period from October 1, 2019, to July 1, 2024 (Figure 3.1b). The floats were equipped with multiple biogeochemical sensors: all 23 floats measured temperature (°C), salinity (PSS-78) and oxygen concentration (O_2, μmol kg^{-1}), 20 floats measured pH, 18 floats measured chlorophyll-a concentration (Chl-a, mg m^{-3}) and optical backscatter, and 11 floats measured nitrate concentration (NO_3, μmol kg^{-1}). The data used in this analysis were from the delayed-mode quality control dataset, with only data flagged as QC level 1 being selected for inclusion (Schmechtig et al., 2023).

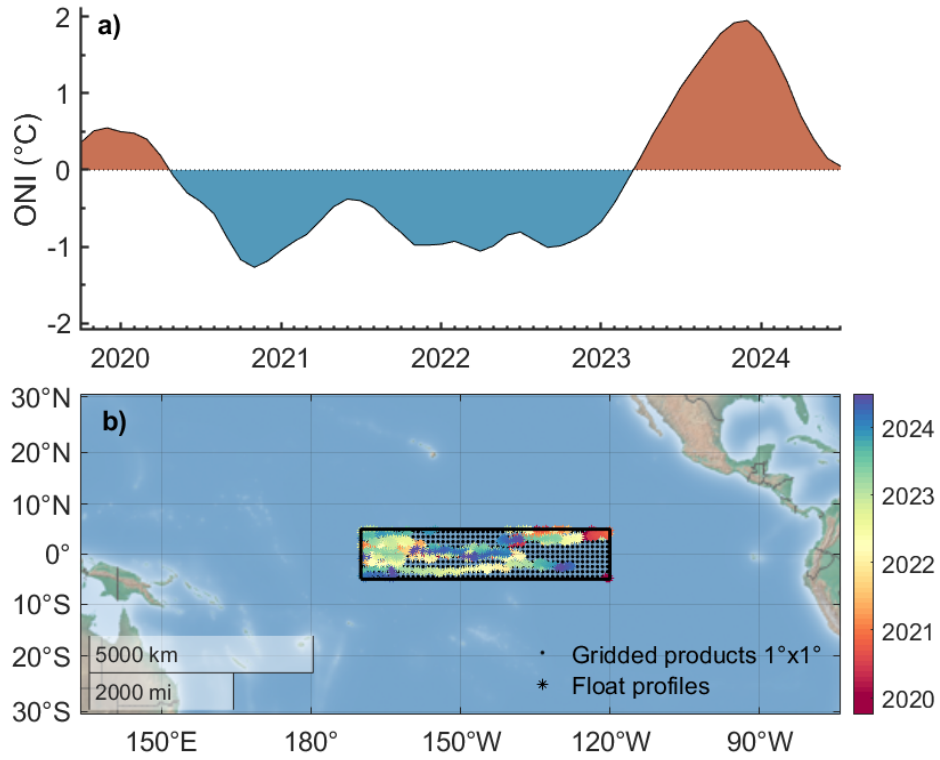

Figure 3.1: (a) The Oceanic Niño Index (ONI) surface temperature anomaly from NOAA's National Centers for Environmental Prediction. (b) Map of the equatorial Pacific Ocean, with the Niño-3.4 region (5°S to 5°N, 170°W to 120°W) shown with the black box. Float profile locations (stars) are colored by year, and a 1°x1° grid (black dots) represents the climatological spatial coverage used in this study.

The World Meteorological Organization IDs (WMOID) for each float were obtained using the OneArgo-Mat toolbox for MATLAB (Frenzel et al., 2022). After selection, corresponding data files were downloaded from the MBARI FloatViz QC directory. These files contained estimates of total alkalinity (TA, μmol kg^{-1}), derived using the Linearly Interpolated Alkalinity Regression (LIARv2) method, using a combination of temperature, salinity, oxygen and nitrate when available (Carter et al., 2016). Derived carbonate system parameters, such as total dissolved inorganic carbon (DIC, μmol kg^{-1}) were then calculated using the LIAR-estimated TA and the measured float pH values with CO2SYS (Lewis and Wallace, 1998; Sharp et al., 2023).

The mixed layer pressure (MLP) was calculated using the Gibbs Seawater Oceanography Toolbox V3.06.12, where the MLP is defined as the pressure at which density exceeds surface density by 0.03 kg m^{-3} (de Boyer Montégut et al., 2004, McDougall & Barker 2011). The mixed layer depth (MLD) in meters was then calculated from the mixed layer

pressure and latitude for each profile and used throughout this study. All float profiles within the Niño-3.4 region were included in the estimated of the MLD, with monthly mean MLD values used for further analysis.

The depth (m) of the 20°C isotherm (Z20), calculated for each profile, was used as a proxy to describe the depth of the thermocline in this region even though recent studies challenge this theory (Yang and Wang, 2009; Castaño-Tierno et al., 2018 and references therein). As for the MLD, all profiles of Z20 were used with a monthly mean used for analysis.

We also utilized apparent oxygen utilization (AOU, μmol kg^{-1}), calculated as the difference between the oxygen concentration at saturation (Garcia & Gordon, 1992) and the float-measured oxygen concentration. Ocean spiciness (or mintiness) is used to describe how warm (cold) and salty (fresh) the seawater is, which aids in tracking ocean mixing and water masses through density-compensated anomalies of temperature and salinity (Munk, 1981; Zeller et al., 2021). Spiciness was computed using the GSW toolbox (McDougall & Barker, 2011). Lastly preformed nitrate ($preNO_3$) was calculated as the difference between float-measured nitrate and AOU multiplied by the Redfield Ratio of nitrate to oxygen, N:O = -10, serving as another conservative tracer after accounting for biological process (Broecker, 1974; Emerson & Hayward, 1995; Johnson et al., 2010).

Gridded climatology products

We utilized the 1°x1° gridded GLODAPv2.2016b product (Key et al., 2015; Lauvset et al., 2016), which included temperature, salinity, oxygen, nitrate, pH, and dissolved inorganic carbon (DIC) averaged over the years 1972–2013. The product contained data at depth levels of 0, 10, 20, 30, 50, 75, 100, 125, 150, and 200 meters for the upper ocean. The derived parameters of spiciness, AOU and preNO3 were also calculated for the gridded product data, using the methods outlined in the previous section.

Since GLODAP did not include data for chlorophyll-a or particulate organic carbon (derived from backscatter), we used the global 3D SOCA-BBP product from the EU Copernicus

Marine Service Information (CMEMS; Sauzède et al., 2016). This dataset, available on a 0.25°x0.25° grid, was re-gridded and averaged to match the 1°x1° resolution of the GLODAP product. The SOCA-BBP product also included multiple depth levels extending down to 1000 meters, which were interpolated to align with GLODAP depth levels. However, chlorophyll-a concentrations were available only to a depth of 120 meters.

Lastly, monthly extensions of the Roemmich-Gilson Argo Climatology from October 2019 to July 2024 provided a 1°x1° gridded temperature and salinity anomaly product down to 2000 meters provided an additional asset for the analysis of wide scale features (Roemmich & Gilson, 2009).

Float time-series and anomalies

Float profiles were averaged into 10-meter depth bins, spanning from the surface down to 200 meters. Below 200 meters, float data and anomalies were very stable, providing minimal signals and features warranting further exploration. In addition to depth binning, the data were averaged into monthly time bins. Importantly, minimal data features were lost during this process when compared to either a 1-week or moving filter, ensuring that the original signal integrity was maintained throughout the binning process. All profiles were then averaged in space over the entire Niño-3.4 region, providing a time-series of biogeochemistry in the upper 200 meters.

To ensure comparability with the float data, the gridded climatology data were interpolated onto the same 10-meter depth intervals and location as the float profiles. Anomalies were then computed as the difference between float data and the interpolated climatology. Positive anomalies indicated that the float data values exceeded those of the climatology, while negative anomalies reflected float data values that were lower than climatology.

Biogeochemical Multivariate ENSO Index (BMEI)

To investigate subsurface biogeochemical variability, we developed an index incorporating O_2, DIC and Chl-a. Due to a significant one-year data gap in 2021, NO_3 was

excluded from this index. However, as NO_3 trends generally tracked those of DIC, its exclusion did not significantly alter the resulting index. To facilitate comparisons across the three different variables with differing anomaly ranges, each anomaly time-series was standardized using Z-scores, ensuring all variables were expressed in comparable units.

We then applied Principal Compenent Analysis (PCA) of the three variables' standardized anomaly time-series to identify the dominant modes of variability. We utilized the pca function in MATLAB 2023b to produce the coefficients (loadings) and variance (eigenvalues) of each principal component. Recognizing that several principal components (PCs) could meaningfully contribute to overall variability, we created a unified index by performing a weighted average of the PCs, with each PC weighted according to its explained variance. This approach enabled us to consolidate multiple PCs into a single, representative index of biogeochemical variability.

Results and Discussion

Float time-series and anomalous events

Interannual variability above the mixed layer depth (MLD) in the Niño-3.4 region generally tracked as expected, as measured by BGC-Argo floats (Figure 3.2a-e). Surface oxygen levels remained stable, staying near saturation due to atmospheric exchange above the MLD. During El Niño events, elevated surface temperatures coincided with reductions in nitrate (NO_3) and dissolved inorganic carbon (DIC), consistent with diminished upwelling of deep waters and the shoaling of the MLD and depth of the 20°C isotherm (Z20; Wyrtki et al., 1981). At the onset of the "triple-dip" La Niña (March 2020), there was a notable rebound in chlorophyll-a (Chl-a) in surface waters (Chavez et al., 2002; Lim et al., 2022).

The anomalies in float data compared to the gridded climatology indicated significant events, all occurring below the MLD. To facilitate analysis of this biogeochemical variability, three prominent events were selected, labeled E1, E2, and E3 (Figure 3.2f-j), each

corresponding to notable anomalies. Further discussion of the anomalous events is reserved to O_2, NO_3, and DIC, while the variability in primary productivity (Chl-a) is addressed in the following section.

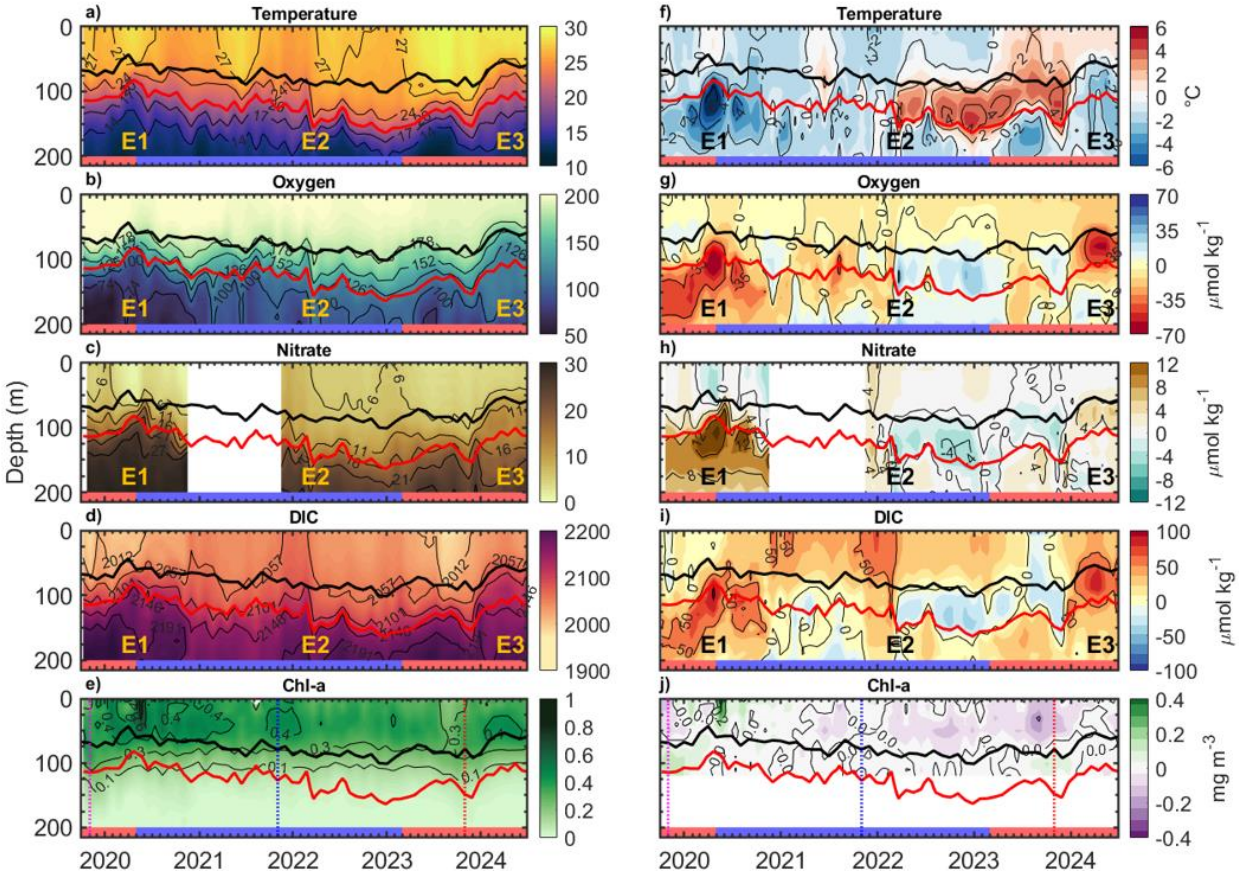

Figure 3.2: Time-depth sections of BGC-Argo float data in the Niño-3.4 region and their respective anomalies. Variables shown include temperature (a & e), oxygen concentration (b & g), nitrate concentration (c & h), dissolved inorganic carbon (DIC, d & i) and chlorophyll-a concentration (Chl-a, e & j). The mixed later depth (MLD, solid black line) and depth of the 20°C isotherm (Z20, solid red line) are shown. E1, E2 & E3 label anomalous subsurface events discussed in the study. The vertical dashed lines in (e) and (j) represent time points of November 2019 (magenta), 2021 (blue), and 2023 (red). Red and blue shading on the x-axis represent durations of El Niño and La Niña, respectively.

Event 1 (E1) follows the transition from a weak El Niño to a strong La Niña in early 2020. During this period, the MLD and Z20 shoaled, resulting in low temperature, O_2 and high NO_3, DIC values below the MLD. Similar signals appear in Event 3 (E3), where shoaling of the MLD and Z20 produced comparable patterns. The anomalies are similar in both magnitude and depth, though they were stronger during the 2020 transition from weak El Niño to La Niña

compared to the 2023 transition from a strong El Niño toward La Niña. These anomalies align with the shoaling of the MLD and Z20 align.

To investigate potential drivers of E1 and E3, we analyzed longitude-time contours of upper ocean temperature anomalies across the equatorial Pacific extracted from Argo floats (Figure 3.3). Distinct phases of warm and cold anomalies in the upper 200 meters exhibited a clear west-to-east propagation, indicating Kelvin wave activity (McPhaden, 2002; Matthews et al., 2007). During E1 in early 2020 and E3 in early 2024, a relatively strong upwelling Kelvin wave crossed the Niño-3.4 region, evidenced by a cold upper-ocean anomaly. The duration of this upwelling event, approximately two months, aligns with the expected transit time of a Kelvin wave across this region (Rydbeck et al., 2019). Shoaling of the MLD and thermocline brought low O_2, high NO_3 and DIC water upwards, creating the anomalies we see at these depths. Notably, anomalies associated with MLD and Z20 (thermocline) shoaling did not appear at the surface. Deeper waters with upwelling characteristics may have remained trapped below the MLD, isolated from direct atmospheric interaction, enhancing their anomalous signature.

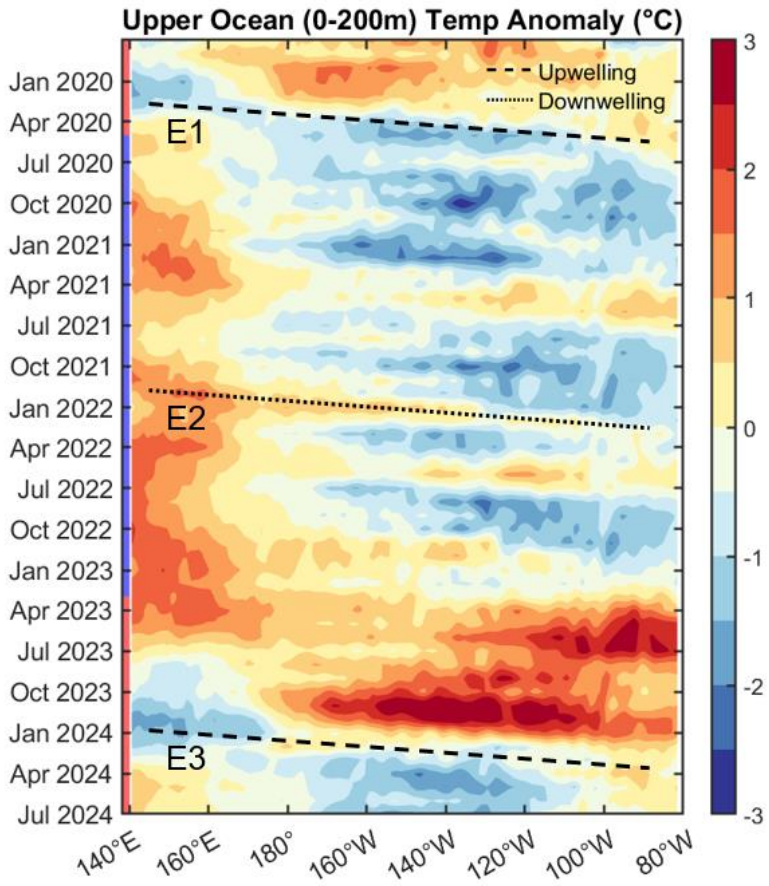

Figure 3.3: Longitude-time contour plot of upper ocean (0-200 meters) temperature anomaly across the equatorial Pacific (2.5°S-2.5°N) from the Roemmich-Gilson Argo climatolagy. Upwelling (thick dashed lines) and downwelling (thin dashed lines) Kelvin Waves shown, with events E1, E2 & E3 corresponding to those in **Figure 3.2**.

Event 2 (E2) was unique and did not follow the pattern of other events. During E2, the Z20 deepened relatively quickly, over ~1 month, without any significant change in the MLD. This isotherm shift created large sub-MLD anomalies lasting for about a year, beginning in the La Niña phase and extending into the strong 2023 El Niño, marked by a sustained increase in temperature, O_2 and a decrease in NO_3, DIC. A downwelling Kelvin wave, known to depress the thermocline, was considered a potential driver. Although a downwelling Kelvin wave was observed during this period (Figure 3.3), its magnitude was relatively weak, and the duration of the event progressed faster than typical Kelvin wave speeds.

Density and spiciness followed temperature trends, highlighting all sub-MLD anomalous events. AOU mirrored oxygen levels without showing any new anomalous signatures due to biological effects.

At the onset of E2, a salinity maximum was observed between the MLD and Z20 at ~ 100 meters, corresponding with high spiciness and low $preNO_3$ values (Figure 3.4a). This high salinity is characteristic of South Pacific Tropical Water (SPTW, O'Connor et al., 2005), while surface salinity lows in the region arise from precipitation, with internal lows linked to Ekman pumping and convergence (Yu, 2015). The subsurface salinity maximum along with high spiciness anomaly, originating south of the equator, reflects transport from SPTW (Qu et al., 2013).

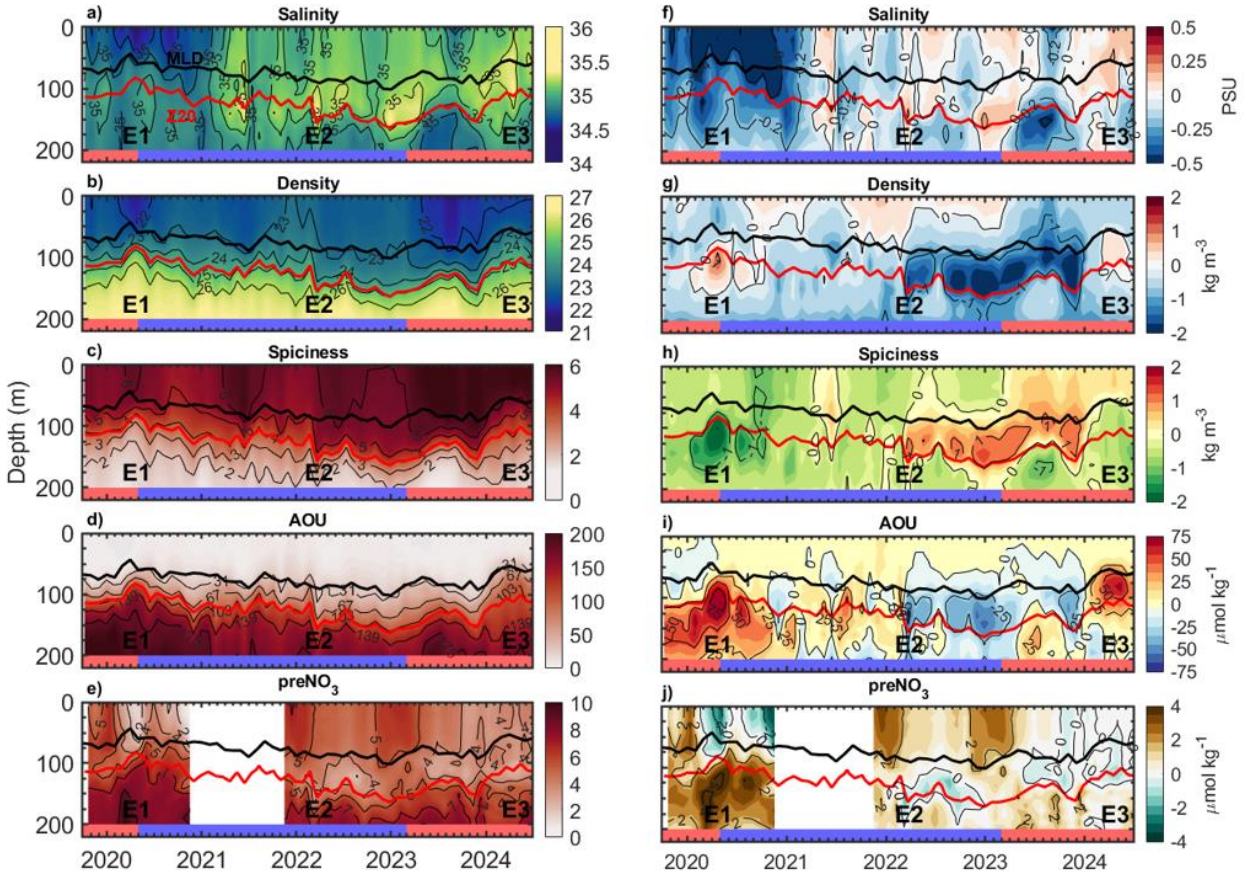

Figure 3.4: Time-depth sections of BGC-Argo salinity and derived parameters in the Niño-3.4 region and their respective anomalies. Variables shown include salinity (a & e), density (b & g), spiciness (c & h), apparent oxygen utilization (AOU, d & i) and preformed nitrate ($preNO_3$, e & j). The mixed later depth (MLD, solid black line), depth of the 20°C isotherm (Z20, solid red line) and events E1, E2 & E3 are the same as **Figure 3.2**.

Subtropical Pacific gyres, where SPTW originates, also contain low or even negative $preNO_3$ values below the surface (Johnson et al., 2010; Smyth and Letscher, 2023). It is hypothesized that the concurrent high salinity, high spiciness and low $preNO_3$ values below the MLD result from meridional transport of SPTW towards the equator. As SPTW water moves into the Niño-3.4 region, it carries with it high temperature and O_2, and low NO_3 and DIC as SPTW was recently at the surface, and subducted equatorward (Wijffels et al., 1996; Izumo, 2005). As the higher sub-MLD salinity values persist into early 2023, it is apparent that meridional transport of SPTW was responsible for maintaining these anomalous values (Nonaka & Sasaki, 2007; Sasaki & Iwai, 2022). Whether this northward transport was initiated by the downwelling Kelvin Wave, wind anomalies or any combination of physical drivers is not further explored in this study.

Redistribution of phytoplankton

A shown in Figure 3.2e, Chl-a trends did not always correlate with other biogeochemical variables. Notable features in the Chl-a data include the high Chl-a "rebound" in early 2020 and the typically low surface Chl-a during the 2023 El Niño. These details were also evident in the anomaly between float and climatology data, with the rebound showing the most positive and the 2023 El Niño the most negative anomalous values in the time series. While float data can capture these events, examining the anomalies reveals positive Chl-a anomalies below the MLD (Figure 3.2j). During both the weak 2020 El Niño and strong 2023 El Niño, positive Chl-a anomalies appeared below the MLD, indicating that while surface primary productivity declined, it increased at depth relative to climatological averages. Turk et al., 2001 reported a similar finding for the western equatorial Pacific, with more recent studies focusing on surface productivity variability in relation to ENSO phases in the central equatorial Pacific (Chavez et al., 2011; Pittman et al., 2022).

To further examine these subsurface differences in primary productivity, we selected three specific time points that differ from those in the previous section – November 1 ± 7 days of

each: November 1, 2019 (weak El Niño, n=3 profiles), November 1, 2022 (midway through the "triple-dip" La Niña, n=4), and November 1, 2023 (strong El Niño, n=10). November 1, 2021 was excluded due to missing NO_3 data. The time points were chosen to consistently represent different phases of the ENSO cycle while preserving the same time of year, thus minimizing any bias in selection of the time points.

Figure 3.5 presents profile data for the three selected time points. During the weak 2020 and strong 2023 El Niño events, we observed the same low surface Chl-a, contrasting with the increased surface Chl-a during La Niña as in the previous section. Conversely, below the MLD (~75 meters), Chl-a was higher during El Niño events, while La Niña displayed reduced sub-MLD Chl-a, even lower than the float average for the study period (n=1077 profiles). Additionally, the subsurface Chl-a maximum shifted deeper during the weak 2020 El Niño. These features are difficult to interpret in the time-series section figures but show significant differences when viewing the profiles.

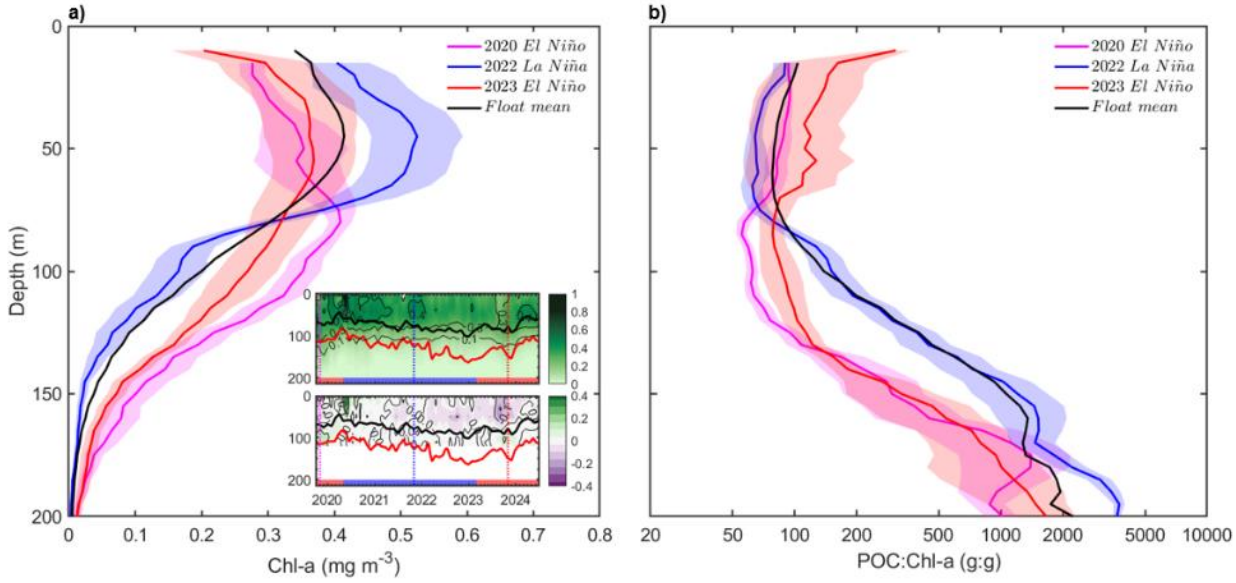

Figure 3.5: Profiles of chlorophyll-a concentration (Chl-a, a) and particulate organic carbon to chlorophyll-a ratio (POC:Chl-a, b) for the time points shown in the inlayed section plots: November 1, 2020 weak El Niño (magenta), November 1, 2022 La Niña (blue) and November 1, 2024 strong El Niño (red). Profile shading is the standard deviation of profile values. Mean profile of all float data shown by the black line without standard deviation. Note the logarithmic x-axis scale for POC:Chl-a.

Below the MLD, Chl-a levels were higher during El Niño than La Niña, suggesting possible phytoplankton redistribution in the water column depending on ENSO phase. Several mechanisms may contribute to this pattern. The first mechanism is the reduction of upwelling during El Niño (Strutton & Chavez 2000; Liao et al., 2020). Despite reduced upwelling, NO_3 levels in surface waters remained above 3 μmol kg^{-1} (Figure 3.6c). El Niño profiles showed increased NO_3 and DIC levels below the MLD, along with decreased O_2, indicating that deeper, nutrient-rich waters still reached the euphotic zone (Turk et al., 2001). The second mechanism is increased stratification during El Niño. Profiles of temperature, O_2, DIC, and NO_3 during El Niño all exhibit more pronounced gradients compared to La Niña profile, suggesting that deep water mixes less effectively into surface waters during El Niño (Liu et al., 2016).

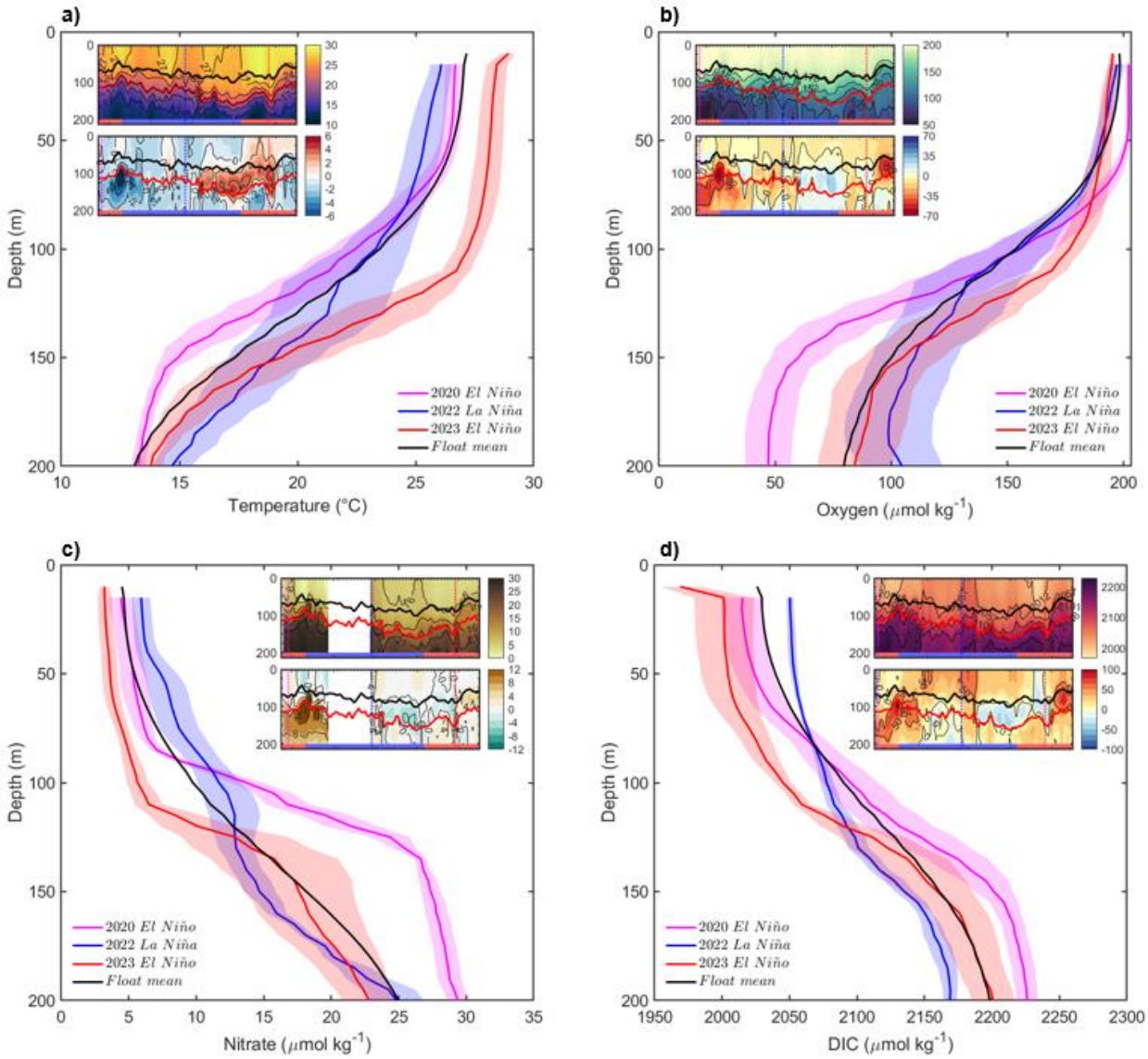

Figure 3.6: Profiles of temperature (a), oxygen concentration (b), nitrate concentration (c) and dissolved inorganic carbon (DIC, d) for the time points shown in the inlayed section plots, as in **Figure 3.5**.

The 3-6 μmol kg nitrate, persistently found in the surface is a result of iron limitation of primary productivity in the equatorial Pacific (Martin et al., 1994; Takeda, 1998; Chavez et al., 1999). The primary iron source to the Niño-3.4 region is via the Equatorial Under Current (EUC), which delivers iron-rich water into the euphotic zone, supporting productivity (Slemons et al., 2010; Coale et al., 1996). As the EUC flows eastward, iron concentrations decrease, with lower

levels in the upper EUC where mixing into the thermocline allows iron uptake by phytoplankton (Slemons et al., 2010).

With the observed increase in NO_3, DIC and decrease in O_2 below the MLD during El Nino years (Figure 3.6), we infer that this water likely contains elevated iron levels (Aufdenkampe & Murray, 2001; Winckler et al., 2016; Rafter 2024). During El Niño, Kelvin wave activity shoals the thermocline and MLD, allowing this micronutrient-rich water to rise higher in the water column. Although increased stratification limits its mixing to the surface, phytoplankton at depth within the euphotic zone can still access the iron from the EUC, causing the higher Chl-a values and positive anomalies at depth below the MLD during El Niño.

To further evaluate these theories, we analyzed the particulate organic carbon to chlorophyll-a (POC:Chl-a) ratios during key periods to gain additional insights into the phytoplankton community dynamics (Figure 3.5b). The POC:Chl-a ratio serves as a useful proxy for assessing phytoplankton dominance, as well as light, nutrient, or temperature limitations, and can be indicative of community composition (Schallenberg et al., 2019). In surface waters, we observed that the POC:Chl-a ratio did not significantly differ between El Niño and La Niña years. Below the MLD, however, elevated POC:Chl-a ratios coincide with lower Chl-a levels during La Niña. Elevated POC:Chl-a ratios are typically associated with iron limitation, as phytoplankton experiencing iron stress exhibit reduced chlorophyll-a pigmentation (Westberry et al., 2016). This supports our hypothesis that increased iron availability may have occurred during El Niño, as indicated by lower POC:Chl-a ratios. It is also worth noting that other sources of POC during La Niña could contribute to increased POC:Chl-a ratios, suggesting an influx of non-photosynthetic organisms and particles (Wang et al., 2009; Wang et al., 2013).

Biogeochemical Multivariate ENSO Index (BMEI)

To further quantify and assess modes of biogeochemical variability in the Niño-3.4 region and the influence by ENSO phases, we developed a Biogeochemical Multivariate ENSO Index (BMEI), similar to the Multivariate ENSO Index that computes a single index from multiple

input variables (Wolter & Timlin, 2011). Given the distinct biogeochemical variability between the surface and subsurface, as well as across different variables, we computed two indices: $BMEI_{SURF}$ for surface interactions (in the MLD) and $BMEI_{SUB}$ for subsurface interactions (below the MLD). After calculating the three principal components (PCs) for each index, we combined PC1 and PC2, which accounted for most of the variability—83% for $BMEI_{SURF}$ and 94% for $BMEI_{SUB}$ (Table 3.1).

Table 3.1: Loadings for each Principal Component (PC) from each variable in the Biogeochemical Multivariate ENSO Index (BMEI), and the percent of variance for each PC.

Loadings (Coefficients)						
	$BMEI_{SURF}$			**$BMEI_{SUB}$**		
	PC1	**PC2**	**PC3**	**PC1**	**PC2**	**PC3**
Oxygen	0.20	0.87	-0.45	0.65	0.29	0.67
DIC	0.64	-0.47	-0.61	-0.67	-0.11	0.74
Chl-a	0.75	0.17	0.65	-0.28	0.95	-0.11
Percent	48%	35%	17%	60%	34%	6%

The BMEI time series, shown in Figure 3.7, revealed that the $BMEI_{SURF}$ inversely tracked the Oceanic Niño Index (ONI) with a correlation coefficient of -0.7 ($p < 0.01$). This negative correlation aligned with ENSO impacts on surface conditions, as O_2 and DIC were influenced by atmospheric interactions and saturation effects related to temperature (e.g., warmer temperatures decrease surface O_2 and CO_2 saturation). Additionally, Chl-a productivity decreased during El Niño and increased during La Niña, further reinforcing the negative correlation.

The principal components (PCs) supported this trend, as no single PC captured the majority of the variability. PC1 was primarily influenced by Chl-a and DIC, while PC2 was driven primarily by oxygen. Oxygen showed a positive but lower correlation with DIC and Chl-a in PC1, indicating a shared mode of variability, though DIC may also be affected by upwelling and slower atmospheric equilibration. Notably, $BMEI_{SURF}$ showed no significant correlation with the

MLD, suggesting that surface variability was primarily influenced by atmospheric conditions and productivity rather than by upwelling or downwelling of the MLD and thermocline.

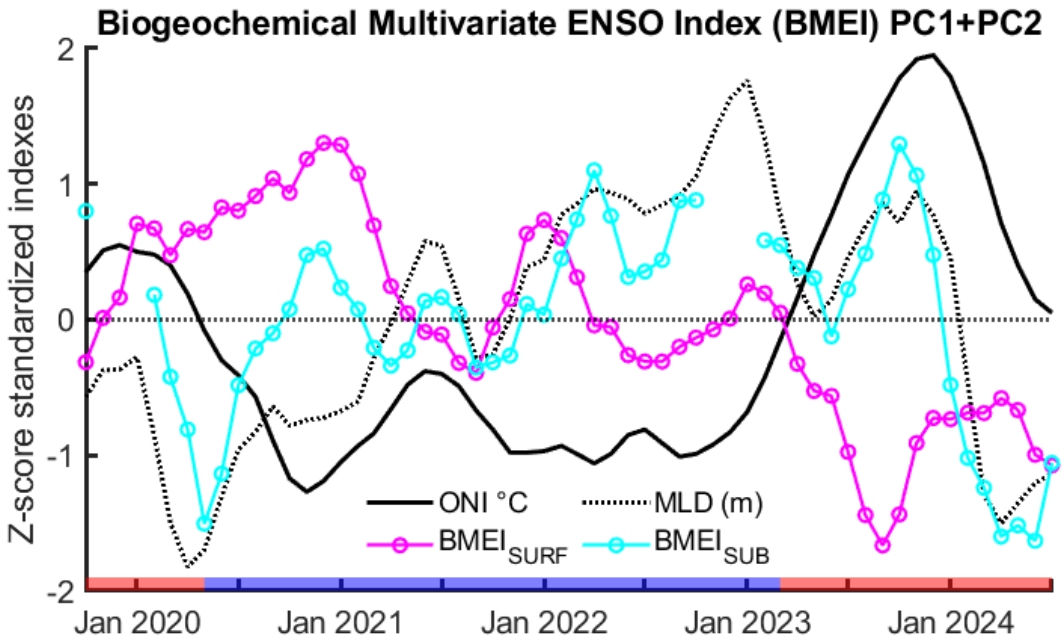

Figure 3.7: Biogeochemical Multivariate ENSO Index (BMEI) from October 2019 to July 2024 for within ($BMEI_{SURF}$, magenta) and below ($BMEI_{SUB}$, cyan) the mixed layer depth (MLD, dashed black line). The Oceanic Niño Index (ONI) shown with the solid black line. Red and blue shading on the x-axis represents durations of El Niño and La Niña, respectively.

In contrast, $BMEI_{SUB}$ showed a strong correlation with the MLD, with a significant correlation coefficient of 0.8 ($p < 0.01$). The MLD was standardized such that positive values equate to deepening (greater depth) of the MLD. As the MLD shoaled or deepened, this caused the biogeochemical anomalies to vary at depth. Notably, $BMEI_{SUB}$ did not correlate with the ONI, indicating distinct surface and subsurface biogeochemical responses, driven by different factors.

Most of the $BMEI_{SUB}$ variability (60%) was explained by PC1, dominated by O_2 and DIC, which tracked with MLD movement driven by Kelvin Waves during the extreme anomalous events (Section 3.1). For example, in early 2020 (E1) and 2023 (E3), upwelling Kelvin Waves caused the MLD and Z20 to shoal, promoting O_2 anomalies to decrease and DIC anomalies to increase (hence the inverse signs of the loadings). PC2 explained 34% of the variability, primarily driven by Chl-a anomalies, which were prominent below the MLD during El Niño

events compared to La Niña with the redistribution of phytoplankton due to iron availability in deeper water and increased stratification.

Though four years is a relatively brief study period in the context of ENSO, our findings clearly demonstrate the added dimension of observing subsurface biogeochemistry, which is often under sampled (Kessler & Cravatte, 2021). Continued profiling float observations, including floats with nitrate, will fill the much-needed gaps in our understanding of subsurface biogeochemical variability in the equatorial Pacific. Additionally, measuring iron or establishing links between biogeochemical parameters and iron would enhance understanding of primary productivity feedbacks in this region (Rafter et al., 2017). Employing the BMEI may aid in monitoring ENSO cycle intensity and improving prediction efforts by integrating subsurface phenomena observable from profiling floats. Our main finding that the region's biogeochemistry was primarily influenced by physical processes highlights the need for continued monitoring and study of biogeochemical-physical interactions, in conjunction with the other monitoring efforts to fully understand the drivers of biogeochemical variability in response to ENSO phases.

Conclusions

In this study, we presented novel insights into biogeochemical variability in the Niño-3.4 region from 23 BGC-Argo profiling floats in relation to the 2019-2024 ENSO cycles, which provided information inaccessible by other monitoring systems. We highlighted the spatial and temporal extent of the biogeochemical variability, investigating some potential drivers. The BGC-Argo float time-series and anomalies revealed greater variability and larger anomalies at depth, likely driven by Kelvin wave activity and subducted meridional transport of South Pacific Tropical Water (SPTW), altering sub-MLD biogeochemistry. Above the MLD, atmospheric interactions maintained steadier conditions.

Many parameters utilized were derived from float-measured variables, introducing some uncertainties. For instance, dissolved inorganic carbon (DIC) was calculated from float-

measured pH and estimated total alkalinity (TA). Surface LIAR-estimated TA uncertainty is about 6 μmol kg^{-1} for this region (Carter et al., 2016), and pH uncertainty from floats is 0.01 (Maurer et al., 2021; Wimart-Rousseau et al., 2024), resulting in a DIC uncertainty of ~10 μmol kg^{-1} at the surface estimated from CO2SYS error propagation (Orr et al., 2018; Sharp et al., 2023). The anomalous DIC features observed significantly exceed this margin, underscoring their reliability. Profiling floats thus offer extensive information that complements data from other monitoring programs, like the tropical mooring array and climatological data from ships and satellite observations

The equatorial Pacific is highly physically dynamic, with multiple drivers of seasonal and interannual variability. Tropical Instability Waves (TIWs), for example, propagate along the equator and create vortices that facilitate deep ventilation, thermocline mixing, and meridional transport on short timescales (~1 month), particularly around wave cusps (Willett et al., 2006; Eddebbar et al., 2021).

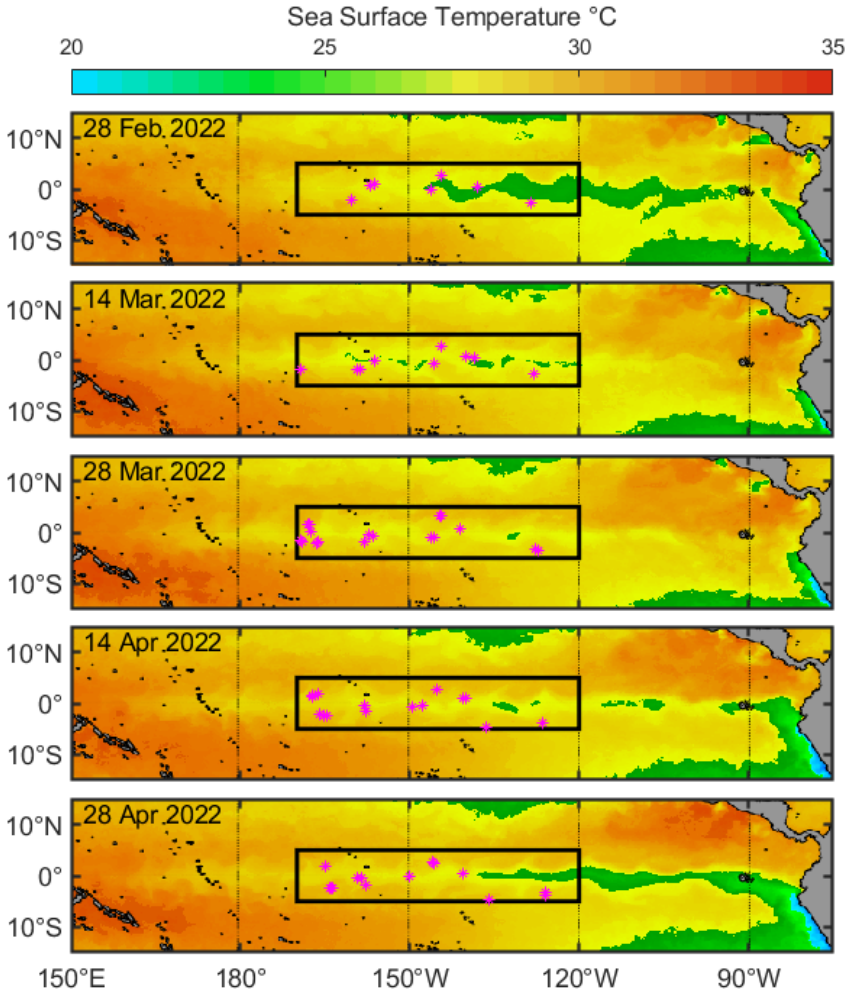

Figure 3.8: Sea Surface Temperature (°C) in the equatorial Pacific from the NOAA Coral Reef Watch daily global 5km product. Panels represent different daily snapshots of SST, with magenta stars representing float profile locations of those days ± 3 days. Boxed outline is the Niño-3.4 region.

During Event 2, we evaluated whether TIWs could bias the time-series by interacting with the limited float profiles, leading to the observed downwelling feature (Figure 3.8). TIWs were active in February 2022, with several (n=4) float profiles positioned near cooler surface water cusps, which coincided with a rapid thermocline deepening observed. By March 2022, TIW activity decreased, likely due to a downwelling Kelvin wave (Holmes & Thomas, 2016), then resumed in April and continued through boreal summer and fall, its peak season (Kiladis et al., 2009). During this period, float profile coverage remained zonally uniform, with profiles north and south of the equator. Averaging profiles across the region would then obscure small-scale TIW-induced variability as well as zonal and meridional gradients, such as the east-to-west

nutrient and Chl-a decline (Christian et al., 2001). The persistence of sub-MLD anomalies from 2022 into 2023 suggests that while TIWs may promote some variability, they were likely not the primary driver.

During El Niño, phytoplankton were redistributed deeper in the water column, likely to access elevated iron levels supplied by the Equatorial Under Current (EUC; Browning et al., 2023). The EUC is influenced by ENSO cycles, slowing during El Niño and accelerating during La Niña (Karnauskas et al., 2020). Iron recycling in this region also plays a role and depends on residence time, where longer residence durations allowing for more iron regeneration and uptake, which further supports primary productivity (Rafter, 2024).

ENSO cycles drive multiple mechanisms affecting primary productivity distribution, such as increased warming and stratification, which reduce surface mixing with nutrient-rich deeper waters (Behrenfeld et al., 2006). Floats provide unique insights into this subsurface variability and capture anomalous events that are challenging for traditional measurements. Moorings lack adequate depth coverage of biogeochemical measurements, ships are too infrequent, and satellites only capture surface data (Smith et al., 2019). Floats thus offer an unprecedented view of this remote region and the impact of ENSO on primary productivity. Understanding the phytoplankton subsurface variability can refine net primary productivity and carbon export estimates (Guidi et al., 2007).

Researchers frequently develop indices for the tropical Pacific to relate ENSO dynamics and cycles with other natural phenomena, including the NOAA Oceanic Niño Index, Multivariate ENSO Index (Wolter et al., 2011), Kelvin Wave Index (Rydbeck et al., 2009), El Niño Modoki Index (Ashok et al., 2007), and Tropical Instability Wave Index (Johnson & Proehl, 2004).

In this study, we created a biogeochemical multivariate ENSO index (BMEI) based on measured anomalies in oxygen (O_2), dissolved inorganic carbon (DIC), and chlorophyll-a (Chl-a) in the Niño-3.4 region, comparing it to the canonical ONI. Observed biogeochemical variability above and below the MLD led us to develop separate indices: $BMEI_{SURF}$ and $BMEI_{SUB}$. $BMEI_{SURF}$

correlated with the ONI, primarily reflecting surface temperature and atmospheric equilibrium. In contrast, $BMEI_{SUB}$ correlated with the MLD, where upwelling, downwelling, and sub-MLD meridional transport influenced biogeochemistry. Additionally, anomalous primary productivity events drove a unique mode of variability, distinct from other biogeochemical parameters which can also differ depending on types of El Niño events (Gierach et al., 2012). This study underscores the value of BGC-Argo floats and the BMEI for tracking biogeochemical variability and improving our understanding of ENSO's impact on ocean biogeochemistry.

Acknowledgements

Chapter 3, in part, is currently being prepared for submission for publication of the material in *Geophysical Research Letters*. Wirth, T., Martz, T., 2024. Subsurface biogeochemical variability in the equatorial Pacific observed by BGC-Argo floats over the 2019-2024 El Niño/La Niña cycle. The dissertation author was the primary investigator and author of this paper.

References

Ashok, K., Behera, S. K., Rao, S. A., Weng, H., & Yamagata, T. (2007). El Niño Modoki and its possible teleconnection. *Journal of Geophysical Research: Oceans*, *112*(C11). https://doi.org/10.1029/2006JC003798

Aufdenkampe, A. K., & Murray, J. W. (2002). Controls on new production: The role of iron and physical processes. *Deep Sea Research Part II: Topical Studies in Oceanography*, *49*(13–14), 2649–2668. https://doi.org/10.1016/S0967-0645(02)00052-8

Behrenfeld, M. J., O'Malley, R. T., Siegel, D. A., McClain, C. R., Sarmiento, J. L., Feldman, G. C., Milligan, A. J., Falkowski, P. G., Letelier, R. M., & Boss, E. S. (2006). Climate-driven trends in contemporary ocean productivity. *Nature*, *444*(7120), 752–755. https://doi.org/10.1038/nature05317

Brainard, R. E., Oliver, T., McPhaden, M. J., Cohen, A., Venegas, R., Heenan, A., Vargas-Ángel, B., Rotjan, R., Mangubhai, S., Flint, E., & Hunter, S. A. (2018). Ecological Impacts of the 2015/16 El Niño in the Central Equatorial Pacific. *Bulletin of the American Meteorological Society*, *99*(1), S21–S26. https://doi.org/10.1175/BAMS-D-17-0128.1

Bresnahan, P. J., Takeshita, Y., Wirth, T., Martz, T. R., Cyronak, T., Albright, R., Wolfe, K., Warren, J. K., & Mertz, K. (2021). Autonomous in situ calibration of ion-sensitive field effect transistor pH sensors. *Limnology and Oceanography: Methods*. https://doi.org/10.1002/lom3.10410

Broecker, W. S. (1974). “NO”, a conservative water-mass tracer. *Earth and Planetary Science Letters*, *23*(1), 100–107. https://doi.org/10.1016/0012-821X(74)90036-3

Browning, T. J., Saito, M. A., Garaba, S. P., Wang, X., Achterberg, E. P., Moore, C. M., Engel, A., Mcllvin, M. R., Moran, D., Voss, D., Zielinski, O., & Tagliabue, A. (2023). Persistent equatorial Pacific iron limitation under ENSO forcing. *Nature*, *621*(7978), 330–335. https://doi.org/10.1038/s41586-023-06439-0

Carter, B. R., Williams, N. L., Gray, A. R., & Feely, R. A. (2016). Locally interpolated alkalinity regression for global alkalinity estimation. *Limnology and Oceanography: Methods*, *14*(4), 268–277. https://doi.org/10.1002/lom3.10087

Castaño-Tierno, A., Mohino, E., Rodríguez-Fonseca, B., & Losada, T. (2018). Revisiting the CMIP5 Thermocline in the Equatorial Pacific and Atlantic Oceans. *Geophysical Research Letters*, *45*(23), 12,963-12,971. https://doi.org/10.1029/2018GL079847

Chavez, F. P., Messié, M., & Pennington, J. T. (2011). Marine Primary Production in Relation to Climate Variability and Change. *Annual Review of Marine Science*, *3*(1), 227–260. https://doi.org/10.1146/annurev.marine.010908.163917

Chavez, F. P., Pennington, J. T., Castro, C. G., Ryan, J. P., Michisaki, R. P., Schlining, B., Walz, P., Buck, K. R., McFadyen, A., & Collins, C. A. (2002). Biological and chemical consequences of the 1997–1998 El Niño in central California waters. *Progress in Oceanography*, *54*(1–4), 205–232. https://doi.org/10.1016/S0079-6611(02)00050-2

Chavez, F. P., Strutton, P. G., Friederich, G. E., Feely, R. A., Feldman, G. C., Foley, D. G., & McPhaden, M. J. (1999). Biological and Chemical Response of the Equatorial Pacific Ocean to the 1997-98 El Niño. *Science*, *286*(5447), 2126–2131. https://doi.org/10.1126/science.286.5447.2126

Christian, J. R., Verschell, M. A., Murtugudde, R., Busalacchi, A. J., & McClain, C. R. (2001). Biogeochemical modelling of the tropical Pacific Ocean. I: Seasonal and interannual variability. *Deep Sea Research Part II: Topical Studies in Oceanography*, *49*(1), 509–543. https://doi.org/10.1016/S0967-0645(01)00110-2

Claustre, H., Johnson, K. S., & Takeshita, Y. (2020). Observing the Global Ocean with Biogeochemical-Argo. *Annual Review of Marine Science*, *12*(1), 23–48. https://doi.org/10.1146/annurev-marine-010419-010956

Coale, K. H., Johnson, K. S., Fitzwater, S. E., Gordon, R. M., Tanner, S., Chavez, F. P., Ferioli, L., Sakamoto, C., Rogers, P., Millero, F., Steinberg, P., Nightingale, P., Cooper, D., Cochlan, W. P., Landry, M. R., Constantinou, J., Rollwagen, G., Trasvina, A., & Kudela, R. (1996). A massive phytoplankton bloom induced by an ecosystem-scale iron fertilization experiment in the equatorial Pacific Ocean. *Nature*, *383*(6600), 495–501. https://doi.org/10.1038/383495a0

Czeschel, R., Stramma, L., & Johnson, G. C. (2012). Oxygen decreases and variability in the eastern equatorial Pacific. *Journal of Geophysical Research: Oceans*, *117*(C11). https://doi.org/10.1029/2012JC008043

de Boyer Montégut, C., Madec, G., Fischer, A. S., Lazar, A., & Iudicone, D. (2004). Mixed layer depth over the global ocean: An examination of profile data and a profile-based climatology. *Journal of Geophysical Research: Oceans*, *109*(C12), 1–20. https://doi.org/10.1029/2004JC002378

Eddebbar, Y. A., Long, M. C., Resplandy, L., Rödenbeck, C., Rodgers, K. B., Manizza, M., & Keeling, R. F. (2017). Impacts of ENSO on air-sea oxygen exchange: Observations and mechanisms. *Global Biogeochemical Cycles*, *31*(5), 901–921. https://doi.org/10.1002/2017GB005630

Eddebbar, Y. A., Subramanian, A. C., Whitt, D. B., Long, M. C., Verdy, A., Mazloff, M. R., & Merrifield, M. A. (2021). Seasonal Modulation of Dissolved Oxygen in the Equatorial Pacific by Tropical Instability Vortices. *Journal of Geophysical Research: Oceans*, *126*(11), e2021JC017567. https://doi.org/10.1029/2021JC017567

Emerson, S., & Hayward, T. (1995). Chemical tracers of biological processes in shallow waters of North Pacific: Preformed nitrate distributions. *Journal of Marine Research*, *53*(3). https://elischolar.library.yale.edu/journal_of_marine_research/2149

Frenzel, H., Sharp, J. D., Fassbender, A. J., & Buzby, N. (2022). *OneArgo-Mat: A MATLAB toolbox for accessing and visualizing Argo data* (Version v1.0.3) [Computer software]. Zenodo. https://doi.org/10.5281/zenodo.7055484

Garcia, H. E., & Gordon, L. I. (1992). Oxygen solubility in seawater: Better fitting equations. *Limnology and Oceanography*, *37*(6), 1307–1312. https://doi.org/10.4319/LO.1992.37.6.1307

Gierach, M. M., Lee, T., Turk, D., & McPhaden, M. J. (2012). Biological response to the 1997–98 and 2009–10 El Niño events in the equatorial Pacific Ocean. *Geophysical Research Letters*, *39*(10). https://doi.org/10.1029/2012GL051103

Guidi, L., Stemmann, L., Legendre, L., Picheral, M., Prieur, L., & Gorsky, G. (2007). Vertical distribution of aggregates (>110 µm) and mesoscale activity in the northeastern Atlantic: Effects on the deep vertical export of surface carbon. *Limnology and Oceanography*, *52*(1), 7–18. https://doi.org/10.4319/lo.2007.52.1.0007

Holmes, R. M., & Thomas, L. N. (2016). *Modulation of Tropical Instability Wave Intensity by Equatorial Kelvin Waves*. https://doi.org/10.1175/JPO-D-16-0064.1

Influence of El Niño on the equatorial Pacific contribution to atmospheric CO2 accumulation | Nature. (n.d.). Retrieved November 7, 2024, from https://www.nature.com/articles/19273

Izumo, T. (2005). The equatorial undercurrent, meridional overturning circulation, and their roles in mass and heat exchanges during El Niño events in the tropical Pacific ocean. *Ocean Dynamics*, *55*(2), 110–123. https://doi.org/10.1007/s10236-005-0115-1

Jiang, S., Zhu, C., Hu, Z.-Z., Jiang, N., & Zheng, F. (2023). Triple-dip La Niña in 2020–23: Understanding the role of the annual cycle in tropical Pacific SST. *Environmental Research Letters*, *18*(8), 084002. https://doi.org/10.1088/1748-9326/ace274

Johnson, E. S., & Proehl, J. A. (2004). *Tropical Instability Wave Variability in the Pacific and Its Relation to Large-Scale Currents*. https://journals.ametsoc.org/view/journals/phoc/34/10/1520-0485_2004_034_2121_tiwvit_2.0.co_2.xml

Johnson, K. S., Riser, S. C., & Karl, D. M. (2010). Nitrate supply from deep to near-surface waters of the North Pacific subtropical gyre. *Nature*, *465*(7301), 1062–1065. https://doi.org/10.1038/nature09170

Karnauskas, K. B., Jakoboski, J., Johnston, T. M. S., Owens, W. B., Rudnick, D. L., & Todd, R. E. (2020). The Pacific Equatorial Undercurrent in Three Generations of Global Climate Models and Glider Observations. *Journal of Geophysical Research: Oceans*, *125*(11), e2020JC016609. https://doi.org/10.1029/2020JC016609

Kessler, W. S., & Cravatte, S. (2021). *Final Report of TPOS 2020*.

Key, R. M., Lauvset, S. K., Olsen, A., Van Heuven, S. M. A. C., Velo, A., Lin, X., Schirnick, C., Kozyr, A., Tanhua, T., Hoppema, M., Jutterström, S., Steinfeldt, R., Jeansson, E., Ishii, M., Pérez, F. F., Suzuki, T., & Watelet, S. (2023). *A new global interior ocean mapped climatology: The 1° × 1° GLODAP version 2 from 1972-01-01 to 2013-12-31 (NCEI Accession 0286118)* [Dataset]. NOAA National Centers for Environmental Information. https://doi.org/10.3334/CDIAC/OTG.NDP093_GLODAPV2

Kiladis, G. N., Wheeler, M. C., Haertel, P. T., Straub, K. H., & Roundy, P. E. (2009). Convectively coupled equatorial waves. *Reviews of Geophysics*, *47*(2). https://doi.org/10.1029/2008RG000266

Lauvset, S. K., Key, R. M., Olsen, A., van Heuven, S., Velo, A., Lin, X., Schirnick, C., Kozyr, A., Tanhua, T., Hoppema, M., Jutterström, S., Steinfeldt, R., Jeansson, E., Ishii, M., Perez, F. F., Suzuki, T., & Watelet, S. (2016). A new global interior ocean mapped climatology: The 1° × 1° GLODAP version 2. *Earth System Science Data*, *8*(2), 325–340. https://doi.org/10.5194/essd-8-325-2016

Leung, S., Thompson, L., McPhaden, M. J., & Mislan, K. A. S. (2019). ENSO drives near-surface oxygen and vertical habitat variability in the tropical Pacific. *Environmental Research Letters*, *14*(6), 064020. https://doi.org/10.1088/1748-9326/ab1c13

Lewis, E., Wallace, D., & Allison, L. J. (1998). *Program developed for CO{sub 2} system calculations* (ORNL/CDIAC-105). Brookhaven National Lab., Dept. of Applied Science, Upton, NY (United States); Oak Ridge National Lab., Carbon Dioxide Information Analysis Center, TN (United States). https://doi.org/10.2172/639712

Li, X., Hu, Z.-Z., McPhaden, M. J., Zhu, C., & Liu, Y. (2023). Triple-Dip La Niñas in 1998–2001 and 2020–2023: Impact of Mean State Changes. *Journal of Geophysical Research: Atmospheres*, *128*(17), e2023JD038843. https://doi.org/10.1029/2023JD038843

Liao, E., Resplandy, L., Liu, J., & Bowman, K. W. (2020). Amplification of the Ocean Carbon Sink During El Niños: Role of Poleward Ekman Transport and Influence on Atmospheric CO2. *Global Biogeochemical Cycles*, *34*(9), e2020GB006574. https://doi.org/10.1029/2020GB006574

Lim, H.-G., Dunne, J. P., Stock, C. A., Ginoux, P., John, J. G., & Krasting, J. (2022). Oceanic and Atmospheric Drivers of Post-El-Niño Chlorophyll Rebound in the Equatorial Pacific. *Geophysical Research Letters*, *49*(5), e2021GL096113. https://doi.org/10.1029/2021GL096113

Liu, C., Köhl, A., Liu, Z., Wang, F., & Stammer, D. (2016). Deep-reaching thermocline mixing in the equatorial pacific cold tongue. *Nature Communications*, *7*(1), 11576. https://doi.org/10.1038/ncomms11576

Martin, J. H., Coale, K. H., Johnson, K. S., Fitzwater, S. E., Gordon, R. M., Tanner, S. J., Hunter, C. N., Elrod, V. A., Nowicki, J. L., Coley, T. L., Barber, R. T., Lindley, S., Watson, A. J., Van Scoy, K., Law, C. S., Liddicoat, M. I., Ling, R., Stanton, T., Stockel, J., … Tindale, N. W. (1994). Testing the iron hypothesis in ecosystems of the equatorial Pacific Ocean. *Nature*, *371*(6493), 123–129. https://doi.org/10.1038/371123a0

Mathis, J. T., Feely, R. A., & Sutton, A. (2014). *White Paper #6 – Tropical Pacific Biogeochemistry: Status, Implementation and Gaps*.

Matthews, A. J., Singhruck, P., & Heywood, K. J. (2007). Deep Ocean Impact of a Madden-Julian Oscillation Observed by Argo Floats. *Science*, *318*(5857), 1765–1769. https://doi.org/10.1126/science.1147312

Maurer, T. L., Plant, J. N., & Johnson, K. S. (2021). Delayed-Mode Quality Control of Oxygen, Nitrate, and pH Data on SOCCOM Biogeochemical Profiling Floats. *Frontiers in Marine Science*, *8*. https://www.frontiersin.org/articles/10.3389/fmars.2021.683207

McDougall, & Barker. (2011). *GSW Toolbox*. https://www.teos-10.org/pubs/Getting_Started.pdf

McPhaden, M. J. (2002). *Mixed Layer Temperature Balance on Intraseasonal Timescales in the Equatorial Pacific Ocean*. https://journals.ametsoc.org/view/journals/clim/15/18/1520-0442_2002_015_2632_mltboi_2.0.co_2.xml

McPhaden, M. J., Busalacchi, A. J., Cheney, R., Donguy, J.-R., Gage, K. S., Halpern, D., Ji, M., Julian, P., Meyers, G., Mitchum, G. T., Niiler, P. P., Picaut, J., Reynolds, R. W., Smith, N., & Takeuchi, K. (1998). The Tropical Ocean-Global Atmosphere observing system: A decade of progress. *Journal of Geophysical Research: Oceans*, *103*(C7), 14169–14240. https://doi.org/10.1029/97JC02906

Munk, W. H. (1981). Internal Waves and Small-Scale Processes. *Evolution of Physical Oceanography*.

Nonaka, M., & Sasaki, H. (2007). *Formation Mechanism for Isopycnal Temperature–Salinity Anomalies Propagating from the Eastern South Pacific to the Equatorial Region*. https://doi.org/10.1175/JCLI4065.1

O'Connor, B. M., Fine, R. A., & Olson, D. B. (2005). A global comparison of subtropical underwater formation rates. *Deep Sea Research Part I: Oceanographic Research Papers*, *52*(9), 1569–1590. https://doi.org/10.1016/j.dsr.2005.01.011

Orr, J. C., Epitalon, J.-M., Dickson, A. G., & Gattuso, J.-P. (2018). Routine uncertainty propagation for the marine carbon dioxide system. *Marine Chemistry*, *207*, 84–107. https://doi.org/10.1016/j.marchem.2018.10.006

Pittman, N. A., Strutton, P. G., Johnson, R., Matear, R. J., & Sutton, A. J. (2022). Relationships Between Air-Sea CO2 Flux and New Production in the Equatorial Pacific. *Global Biogeochemical Cycles*, *36*(4), e2021GB007121. https://doi.org/10.1029/2021GB007121

Qu, T., Gao, S., & Fine, R. A. (2013). *Subduction of South Pacific Tropical Water and Its Equatorward Pathways as Shown by a Simulated Passive Tracer*. https://doi.org/10.1175/JPO-D-12-0180.1

Rafter, P. A. (2024). On the Variability of Equatorial Pacific Nitrate and Iron Utilization. *Oceanography*, *37*(2), 72–84.

Rafter, P. A., Sigman, D. M., & Mackey, K. R. M. (2017). Recycled iron fuels new production in the eastern equatorial Pacific Ocean. *Nature Communications*, *8*(1), 1100. https://doi.org/10.1038/s41467-017-01219-7

Roemmich, D., & Gilson, J. (2009). The 2004–2008 mean and annual cycle of temperature, salinity, and steric height in the global ocean from the Argo Program. *Progress in Oceanography*, *82*(2), 81–100. https://doi.org/10.1016/j.pocean.2009.03.004

Roemmich, D., Johnson, G. C., Riser, S., Davis, R., & Gilson, J. (2009). *The Argo Program: Observing the Global Ocean with Profiling Floats | Oceanography*. https://tos.org/oceanography/article/the-argo-program-observing-the-global-ocean-with-profiling-floats

Rydbeck, A. V., Jensen, T. G., & Flatau, M. (2019). Characterization of Intraseasonal Kelvin Waves in the Equatorial Pacific Ocean. *Journal of Geophysical Research: Oceans*, *124*(3), 2028–2053. https://doi.org/10.1029/2018JC014838

Sasaki, Y. N., & Iwai, Y. (2022). Two Pathways of Subsurface Spiciness Anomalies in the Subtropical South Pacific. *Frontiers in Climate*, *4*. https://doi.org/10.3389/fclim.2022.897498

Sauzède, R., Claustre, H., Uitz, J., Jamet, C., Dall'Olmo, G., D'Ortenzio, F., Gentili, B., Poteau, A., & Schmechtig, C. (2016). A neural network-based method for merging ocean color and Argo data to extend surface bio-optical properties to depth: Retrieval of the particulate backscattering coefficient. *Journal of Geophysical Research: Oceans*, *121*(4), 2552–2571. https://doi.org/10.1002/2015JC011408

Schallenberg, C., Harley, J. W., Jansen, P., Davies, D. M., & Trull, T. W. (2019). Multi-Year Observations of Fluorescence and Backscatter at the Southern Ocean Time Series (SOTS) Shed Light on Two Distinct Seasonal Bio-Optical Regimes. *Frontiers in Marine Science*, *6*. https://doi.org/10.3389/fmars.2019.00595

Schmechtig, C., Wong, A., Maurer, T. l, Bittig, H., Thierry, V., Maurer, T. l, Bittig, H., & Thierry, V. (2023). *Argo quality control manual for biogeochemical data*. https://doi.org/10.13155/40879

Sharp, J. D., Pierrot, D., Humphreys, M. P., Epitalon, J.-M., Orr, J. C., Lewis, E. R., & Wallace, D. W. R. (2023). *CO2SYSv3 for MATLAB* (Version v3.2.1) [Computer software]. Zenodo. https://doi.org/10.5281/zenodo.7552554

Slemons, L. O., Murray, J. W., Resing, J., Paul, B., & Dutrieux, P. (2010). Western Pacific coastal sources of iron, manganese, and aluminum to the Equatorial Undercurrent. *Global Biogeochemical Cycles*, *24*(3). https://doi.org/10.1029/2009GB003693

Smith, N., Kessler, W. S., Cravatte, S., Sprintall, J., Wijffels, S., Cronin, M. F., Sutton, A., Serra, Y. L., Dewitte, B., Strutton, P. G., Hill, K., Sen Gupta, A., Lin, X., Takahashi, K., Chen, D., & Brunner, S. (2019). Tropical Pacific Observing System. *Frontiers in Marine Science*, *6*. https://doi.org/10.3389/fmars.2019.00031

Smyth, A. J., & Letscher, R. T. (2023). Spatial and temporal occurrence of preformed nitrate anomalies in the subtropical North Pacific and North Atlantic oceans. *Marine Chemistry*, *252*, 104248. https://doi.org/10.1016/j.marchem.2023.104248

Strutton, P. G., & Chavez, F. P. (2000). Primary productivity in the equatorial Pacific during the 1997–1998 El Niño. *Journal of Geophysical Research: Oceans*, *105*(C11), 26089–26101. https://doi.org/10.1029/1999JC000056

Strutton, P. G., Evans, W., & Chavez, F. P. (2008). Equatorial Pacific chemical and biological variability, 1997–2003. *Global Biogeochemical Cycles*, *22*(2). https://doi.org/10.1029/2007GB003045

Sutton, A. J., Feely, R. A., Sabine, C. L., McPhaden, M. J., Takahashi, T., Chavez, F. P., Friederich, G. E., & Mathis, J. T. (2014). Natural variability and anthropogenic change in equatorial Pacific surface ocean pCO2 and pH. *Global Biogeochemical Cycles*, *28*(2), 131–145. https://doi.org/10.1002/2013GB004679

Takeda, S. (1998). Influence of iron availability on nutrient consumption ratio of diatoms in oceanic waters. *Nature*, *393*(6687), 774–777. https://doi.org/10.1038/31674

Trenberth, K. E. (1997). *The Definition of El Niño*. https://journals.ametsoc.org/view/journals/bams/78/12/1520-0477_1997_078_2771_tdoeno_2_0_co_2.xml

Turk, D., Lewis, M. R., Harrison, G. W., Kawano, T., & Asanuma, I. (2001). Geographical distribution of new production in the western/central equatorial Pacific during El Niño and non-El Niño conditions. *Journal of Geophysical Research: Oceans*, *106*(C3), 4501–4515. https://doi.org/10.1029/1999JC000058

Turk, D., Meinen, C. S., Antoine, D., McPhaden, M. J., & Lewis, M. R. (2011). Implications of changing El Niño patterns for biological dynamics in the equatorial Pacific Ocean. *Geophysical Research Letters*, *38*(23). https://doi.org/10.1029/2011GL049674

Wang, X. J., Behrenfeld, M., Le Borgne, R., Murtugudde, R., & Boss, E. (2009). Regulation of phytoplankton carbon to chlorophyll ratio by light, nutrients and temperature in the Equatorial Pacific Ocean: A basin-scale model. *Biogeosciences*, *6*(3), 391–404. https://doi.org/10.5194/bg-6-391-2009

Wang, X., Murtugudde, R., Hackert, E., & Marañón, E. (2013). Phytoplankton carbon and chlorophyll distributions in the equatorial Pacific and Atlantic: A basin-scale comparative study. *Journal of Marine Systems*, *109–110*, 138–148. https://doi.org/10.1016/j.jmarsys.2012.03.004

Westberry, T. K., Schultz, P., Behrenfeld, M. J., Dunne, J. P., Hiscock, M. R., Maritorena, S., Sarmiento, J. L., & Siegel, D. A. (2016). Annual cycles of phytoplankton biomass in the subarctic Atlantic and Pacific Ocean. *Global Biogeochemical Cycles*, *30*(2), 175–190. https://doi.org/10.1002/2015GB005276

Wijffels, S. E., Toole, J. M., Bryden, H. L., Fine, R. A., Jenkins, W. J., & Bullister, J. L. (1996). The water masses and circulation at 10°N in the Pacific. *Deep Sea Research Part I: Oceanographic Research Papers*, *43*(4), 501–544. https://doi.org/10.1016/0967-0637(96)00006-4

Willett, C. S., Leben, R. R., & Lavín, M. F. (2006). Eddies and Tropical Instability Waves in the eastern tropical Pacific: A review. *Progress in Oceanography*, *69*(2), 218–238. https://doi.org/10.1016/j.pocean.2006.03.010

Wimart-Rousseau, C., Steinhoff, T., Klein, B., Bittig, H., & Körtzinger, A. (2024). Technical note: Assessment of float pH data quality control methods – a case study in the subpolar northwest Atlantic Ocean. *Biogeosciences*, *21*(5), 1191–1211. https://doi.org/10.5194/bg-21-1191-2024

Winckler, G., Anderson, R. F., Jaccard, S. L., & Marcantonio, F. (2016). Ocean dynamics, not dust, have controlled equatorial Pacific productivity over the past 500,000 years. *Proceedings of the National Academy of Sciences*, *113*(22), 6119–6124. https://doi.org/10.1073/pnas.1600616113

Wolter, K., & Timlin, M. S. (2011). El Niño/Southern Oscillation behaviour since 1871 as diagnosed in an extended multivariate ENSO index (MEI.ext). *International Journal of Climatology*, *31*(7), 1074–1087. https://doi.org/10.1002/joc.2336

Wyrtki, K. (1981). *An Estimate of Equatorial Upwelling in the Pacific*. https://journals.ametsoc.org/view/journals/phoc/11/9/1520-0485_1981_011_1205_aeoeui_2_0_co_2.xml

Yang, H., & Wang, F. (2009). *Revisiting the Thermocline Depth in the Equatorial Pacific*. https://doi.org/10.1175/2009JCLI2836.1

Yu, L. (2015). Sea-surface salinity fronts and associated salinity-minimum zones in the tropical ocean. *Journal of Geophysical Research: Oceans*, *120*(6), 4205–4225. https://doi.org/10.1002/2015JC010790

Zeller, M., McGregor, S., van Sebille, E., Capotondi, A., & Spence, P. (2021). Subtropical-tropical pathways of spiciness anomalies and their impact on equatorial Pacific temperature. *Climate Dynamics*, *56*(3), 1131–1144. https://doi.org/10.1007/s00382-020-05524-8